Doctoral Dissertation (Censored)
博士論文（要約）

Studies on Tropical Cyclone Influences on Climate and Environment
（熱帯低気圧が気候および環境場に与える影響に関する研究）

Sho Arakane
荒金 匠

Abstract

The impact of large-scale fields on tropical cyclones (TCs) has been studied extensively. On the other hand, it is expected that TCs, which are vigorous systems, can influence large-scale fields both in situ and remotely, but such studies are not many. Although some studies have reported on the modulation of large-scale fields by the remote effects of TCs over ocean basins, few studies have reported on the modulation of large-scale fields over land. Moreover, few studies have reported the in-situ TC footprint in large-scale fields, but their analysis is limited to the wind field. This study aims to evaluate the impact of tropical cyclones (TCs) on the environment and climate by carrying out a case study analysis to investigate the remote impact of a TC over the Bay of Bengal on East Asia, and by analyzing a dataset in which TC vortices are removed to investigate the in-situ TC footprints.

In Chapter 2, the triggering effect of a TC over the Bay of Bengal (BoB) on a torrential frontal rainfall system over East Asia is investigated through numerical experiments in which the BoB TC data are either included or excluded. These numerical experiments reveal that the TC strengthens (1) the low-level southwesterly winds, which effectively transports tropical warm moist air toward Taiwan and (2) cool dry northerly winds to the north of Taiwan. The strengthened southeasterly and northerly winds intensify the strong frontal system near Taiwan. The results show that, along with the downstream impact of TC over the western North Pacific, a BoB TC also has the potential to modulate the downstream environmental field over East Asia.

In Chapter 3 and Chapter 4, to understand TC footprints in large-scale circulations, specifically considering subtropical high and monsoon trough over the western North Pacific (WNP), a TC-removed dataset is constructed and the TC footprints are investigated by comparing the results of analyses conducted with the original and TC-removed datasets. Although several previous studies have shown how to decompose the wind field into TC and non-TC components, in this study, a method to objectively remove the TC component not only in the wind field but also in the mass and temperature fields is established by using the potential vorticity inversion from the viewpoint of dynamic balance. The results reveal the considerable TC footprints in the climatological mean state and variability over the WNP in 1958–2019, which are characterized by a strengthened monsoon trough and weakened subtropical anticyclonic circulation in the lower troposphere, enhanced anticyclonic circulation in the upper troposphere, and warming throughout the troposphere. TCs constitute distinct footprints in the long-term mean states of the WNP summer monsoon, and their contributions increase intraseasonal and interannual variances by 50%–70%. The propagation of intraseasonal variance is analyzed, revealing that the analysis with TCs exhibits a

stronger northward propagation over the WNP. The interdecadal variations and long-term trends in intraseasonal variance are primarily due to the annual fluctuations in TC activity. The size of TC footprints is positively correlated with the magnitude of TC activity. Moreover, analysis of seasonal-mean low-level vorticity field suggests that TC genesis and seasonal low-level vorticity distributions are closely related, and the vorticity distribution cannot be explained only by the TC-free seasonal circulation only.

This study reveals the remote impact by TC and in-situ TC footprints in large-scale fields with different approach because the remote impact cannot be analyzed by using the TC-removed data constructed in this study. The remote impact is investigated with numerical model experiments and a modification of the large-scale field over land is clearly demonstrated. This is the first to report that a BoB TC modulates the downstream environmental field in East Asia, similar to the downstream impact of TCs over the WNP. On the other hand, the in-situ TC footprints in the large-scale fields are investigated with the TC-removed dataset and it is shown that the in-situ TC footprints are too large to ignore. The findings suggest that climate variabilities and changes cannot be adequately understood based on low-frequency, large-scale circulations alone. Rather, TCs should be regarded as a crucial component in the climate system.

Acknowledgments

Most of the works presented in the dissertation were done under the project by Prof. Huang-Hsiung Hsu of the Anthropogenic Climate Change Research Center, Research Center for Environmental Changes, Academia Sinica, Taiwan. The author deeply acknowledges him for his valuable comments and heartfelt encouragement during the works. The author is grateful to Prof. Masaki Satoh and Prof. Tomoki Miyakawa for their encouragement and very valuable advice during the works. The dissertation would not be completed without their contributions.

The author is indebted to Prof. Masahiro Watanabe, Prof. Yukari Takayabu, Prof. Hisashi Nakamura, Prof. Akira Oka, and Prof. Hiroaki Miura for their critical comments and constructive discussion. The author is also grateful to Prof. Masahide Kimoto, Prof. Yu Kosaka, Prof. Kaoru Sato, Prof. Tomoki Tozuka, Prof. Ichiro Yasuda, Dr. Takao Kawasaki, Dr. Masuo Nakano, Dr. Tomoe Nasuno, Dr. Tomoki Ohno, Dr. Yohei Yamada, and Dr. Akira Yamazaki; their instructive comments were very useful to improve the study.

Thanks are extended to the members and ex-members of Prof. Hsu's research group, especially Dr. Wan-Ling Tseng, Wen-Ming Chang, Hsin-Chien Liang, and Jack Yu, for their bits of help and valuable comments during the work.

Table of contents

Abstract i
Acknowledgments iii
Table of contents iv
Chapter 1. General Introduction 1
1.1. Downstream impact and predecessor rain event 1
1.2. Tropical cyclone footprints in climate 4
1.3. Potential vorticity, PV inversion, and TC-removed data 5
1.4. Aims and objectives 9
Chapter 2. Remote Effect of a Tropical Cyclone over the Bay of Bengal on a Heavy Rainfall Event in Subtropical East Asia 11
2.1. Introduction 11
2.2. Data and methods 13
2.3. Results 17
2.3.1. Observation 17
2.3.2. Numerical simulations 20
2.4. Conclusion 27
Chapter 3. Tropical Cyclone Footprint in Large-Scale Circulation over the Western North Pacific: A Case Study 30
3.1. Introduction 30
3.2. Data and methods 33
3.2.1. Data 33
3.2.2. Basic framework of PV decomposition 34
3.2.3. Determination of TC domain for PV decomposition 39
3.2.4. Estimations of vertical velocity and irrotational wind 42
3.3. Comparison of the effectiveness of PVI and the existing TC removal schemes 42
3.4. Results 49
3.4.1. TC contributions to intraseasonal variability and seasonal-mean fields in the typhoon season in 2004 49
3.4.2. Respective effects of TC-related positive and negative PV anomalies 55
3.5. Conclusion 59

Chapter 4. Tropical Cyclone Footprints in Long-Term Mean State and Multiscale Climate Variability over the Western North Pacific 62

4.1. Introduction 62

4.2. Data and methods 62

4.3. Results 65

4.3.1. TC footprints in climatological seasonal mean circulations 65
4.3.2. TC footprints in the interannual variability 71
4.3.3. TC footprints in the intraseasonal variability 80
4.3.4. Relationship between interannual variations in TC genesis and low-level vorticity fields 90

4.4. Discussion 90

4.5. Conclusion 92

Chapter 5. General conclusion 95

5.1. General discussion 95

5.2. Implications for future works 100

5.3. Concluding remarks 102

References 104

Chapter 1. General Introduction

Tropical cyclones (TCs) are long-lived extreme vortices formed over tropical oceans. Several dozens of TCs are generated each year, causing extreme weather events that cover extensive areas. Characterized by intensive heating and strong disturbances, TCs are likely to trigger distinct perturbations both in situ and remotely, leaving footprints in the large-scale flow. In this study, both the in-situ footprint and remote TC effect on climate will be investigated by a different approach. The in-situ footprint is investigated by comparing original reanalysis and TC-removed dataset which is constructed by removing TCs existed in the original reanalysis. While, because the remote effect cannot be investigated by the same analysis, it is studied by numerical simulations in which a TC is included and excluded in the initial conditions instead of the TC-removed dataset analysis. This section introduces the in-situ TC footprint and remote effect on larger-scale fields, the potential vorticity (PV) inversion technique used in the TC removal procedure, and physical meaning of the TC-removed data.

1.1. Downstream impact and predecessor rain event

Over the western North Pacific (WNP), a recurving TC interacts with a mid-latitude baroclinic flow and undergoes a significant structure change, becoming an extratropical cyclone (Jones et al. 2003). This structure change is called extratropical transition (ET; Sekioka 1956). A cyclone after ET may re-intensify and cause extreme weather such as heavy rainfall (Evans et al. 2017). The interaction of TC with mid-latitude flow induces structural changes in the TC and modulates the flow (Riemer et al. 2008; Grams et al. 2013a,b; Archambault et al. 2013, 2015; Grams and Archambault 2016; Quinting and Jones 2016; Keller et al. 2019). A new cyclone and/or extreme weather may occur some distance from the TC as a result of this mid-latitude flow modification (called downstream impact; Grams et al. 2013a,b; Archambault et al. 2013, 2015). Therefore, a transitioning TC can cause extreme weather events both in the location where it emerges and downstream.

The downstream impact is induced by modulation of upper-level mid-latitude flow [Fig. 1.1 (from Archambault et al. 2013)]. In the case of TC Oscar in 1995, as the TC entered the mid-latitude baroclinic zone, the upper-level ridge amplified, and the jet streak strengthened. With the modifications, the downstream upper-level trough also strengthened, and a new surface cyclone was generated in its location. The strengthened upper-level trough induced strengthening of upper-level ridge further downstream, resulting in extreme weather over North

America.

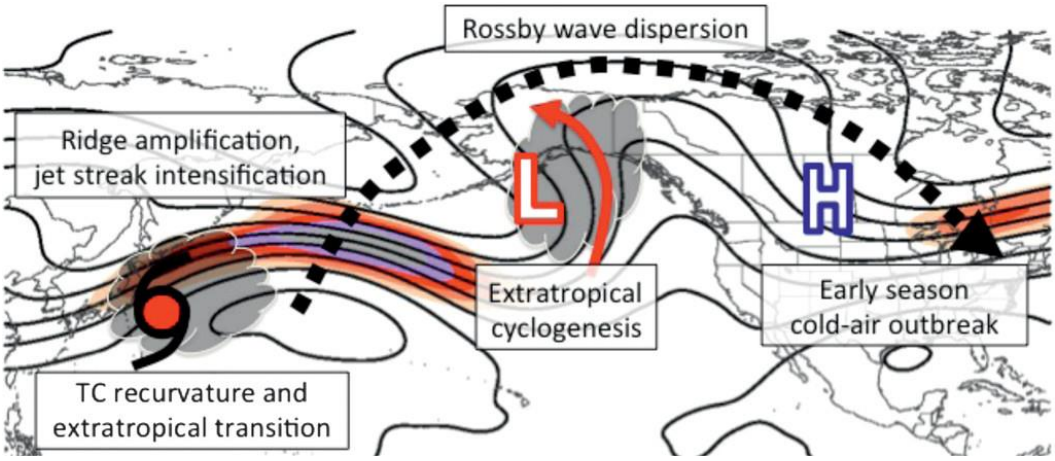

Fig. 1.1. Schematic diagram of key processes of a cold-air outbreak over the central United States by TC Oscar in September 1995. Contours represent the upper-level streamfunction and colors denote the maximum region of wind speed. The "L" and "H" denote the centers of surface cyclone and anticyclone, respectively. [Figure 1 from Archambault et al. (2013). © American Meteorological Society. Used with permission.]

Transitioning TCs do not always modulate the upper-level mid-latitude flow significantly or develop a downstream cyclone. The conditions favorable for this type of downstream impact were investigated by Archambault et al. (2013, 2015). In a climatological study of ETs during 1979–2009, Archambault et al. (2013) revealed that mid-latitude flow could be significantly modulated when a TC entered ahead of an upper-level trough after recurving. Furthermore, the modulation of the mid-latitude flow was found to be highly sensitive to the magnitude of the divergent wind component of the PV advection in the upper troposphere associated with the TC (described in detail later in this section), while it was relatively insensitive to the size or intensity of the recurving TC or the intensity of the TC after ET (Archambault et al. 2013, 2015).

This amplification of the ridge–trough couplet can be explained by the PV advection induced by a TC during ET. The low-level cyclonic PV advection induced by the nondivergent wind component associated with a transitioning TC promotes ridge and upstream trough amplification, while the upper-level anticyclonic PV advection contributes to ridge and downstream trough amplification (Riemer et al. 2008; Riemer and Jones 2010; Grams et al. 2013a,b; Grams and Blumer 2015; Grams and Archambault 2016). Upper-level PV advection by the divergent wind component associated with the transitioning TC also contributes to ridge amplification, and the largest contribution compared with nondivergent PV advection occurs at the lower and upper levels (Riemer and Jones 2010). The PV advection induced by the divergent wind component significantly reduces the eastward

movement of the ridge–trough couplet and maintains the positions of transitioning TC and the ridge–trough couplet for a long period, resulting in "phase locking," which strengthens the ridge persistently (Riemer et al. 2008; Grams et al. 2013b). This phase locking is more likely to occur in the case of a weak jet streak deflected in the meridional direction (Riemer et al. 2008; Riboldi et al. 2018). In contrast, it is less likely to occur in the case of a strong jet streak. Furthermore, the upper-level negative PV advection associated with divergent outflows of a transitioning TC enhances the PV gradient in the upper troposphere (i.e., tropopause gradient), resulting in the formation/enhancement of a jet streak (Archambault et al. 2015). Considering these aspects, it is crucial to develop accurate representations of the nondivergent component of PV advection in the upper level and the phase between the transitioning TC and the ridge–trough couplet, for accurately forecasting the downstream impact in numerical simulations (Keller et al. 2019).

Heavy rainfall may not occur downstream but occurs approximately 1000 km poleward of a TC. This is called a predecessor rain event (PRE), defined as a mesoscale, coherent heavy rainfall event with precipitation greater than 100 mm $(\text{day})^{-1}$ that occurs poleward of the TC (Cote 2007). The key mechanisms of PREs are (1) poleward transport of tropical-origin water vapor by outer (synoptic-scale) circulation of the TC, (2) synoptic-scale frontogenetical (i.e., ascent) forcing in the equatorial side of the jet streak entrance that exists poleward ahead of the TC, and (3) lifting of the TC-induced moisture-rich air parcel via synoptic-scale ascent forcing (Cote 2007). A statistical analysis of 28 PRE cases over the United States during 1995–2008 revealed that the range of the separation distance between the TC and PRE region was from 410 to 1700 km (Galarneau et al. 2010). Galarneau et al. (2010) analyzed a PRE associated with TC Erin (2007), which produced record-breaking rainfall. The analysis revealed that an ascent forcing around a jet streak entrance was necessary to generate a long-lived mesoscale convective system. In contrast, Schumacher et al. (2011) investigated the importance of the poleward transport of moisture-rich air parcels by TC Erin (2007) for the associated PRE using a set of numerical experiments. The results showed that, compared with the features of the PRE reproduced in the control experiment, the sensitivity experiment, in which the TC-related water vapor was removed produced a heavy rainfall area that appeared to be the PRE, but the maximum and total precipitation in the PRE were reduced to approximately 50% and 25%, respectively. Schumacher et al. (2011) concluded that the intermittent moisture supply by TC Erin was an important factor affecting the record-breaking precipitation of the associated PRE. The results by Galarneau et al. (2010) and Schumacher et al. (2011) suggest that poleward moisture supply by TCs and the synoptic-scale ascent forcing ahead of TCs are both important for PRE excitation.

1.2. Tropical cyclone footprints in climate

Large-scale, low-frequency circulation has long been acknowledged to exert a substantial modulating effect on the genesis and development of smaller-scale, high-frequency localized disturbances, such as extreme weather events. In contrast to the well-studied downscaling effect, the potential upscaling process from these disturbances has not received sufficient scholarly attention and thus remains unclear. Although the interplay of downscale and upscale processes is difficult to disentangle, several studies have been conducted. Using observed TC track data and a coupled ocean-atmosphere hurricane model, Emanuel (2001) estimated the poleward heat transport triggered by global TC activity and found that the TC activity could enhance the oceanic thermohaline circulation and play an important role in terms of climate regulation. Hu and Meehl (2009) employed a coupled global model to investigate the impact of an idealized North Atlantic TC on the Atlantic meridional overturning circulation (AMOC) and northward meridional heat transport. It was revealed that strong TC wind increased evaporation and the surface salinity increased, and thus, the AMOC was accelerated, while freshwater induced by strong TC rainfall decreased evaporation and the surface salinity decreased, and thus, the AMOC was decelerated. The net effect of the North Atlantic TC on the AMOC and heat transport was determined by the magnitude of these processes. Using the reanalysis dataset and observed TC track data, Hart (2011) examined the impact of TC activity in the Northern Hemisphere (NH) on the subsequent NH winter season and found a negative correlation between NH TC activity and the stationary meridional heat transport in the NH winter season. Moreover, Chang et al. (2016) revealed that the existence of TC cold wakes slowed the warming sea surface temperature (SST) trend over the WNP over the past few decades.

Hsu et al. (2008a,b) used a dynamic statistical approach to estimate TC footprints in climate variability over the WNP. The studies indicated that TCs significantly contributed to multiscale climate features ranging from intraseasonal variance to long-term mean climatology, although specific dynamic and thermodynamic processes were not identified. In their studies, they argued that TC-related perturbations were too extreme to be removed from original data by simple temporal averaging or low-pass filtering. Thus, climate variability (e.g., variance) estimations would contain substantial TC footprints. However, climate variability research often considered only large-scale dynamics, neglecting the effects of these footprints. This implies that a crucial TC footprint was missed, leading to an incomplete understanding of climate variability.

Hsu et al. (2008a,b) demonstrated the possibility of investigating the TC footprint on the large-scale flow. Using a unique dataset in which TC vortices were removed, they were the first to reveal the significant contributions of TCs to climate variability over the WNP. A comparison between the original and TC-removed datasets revealed that TCs contributed to more than 50% of the intraseasonal and interannual variances. Feng et al. (2020) used the same procedure to isolate the TC-free monsoon trough in a 6-hourly reanalysis dataset, developing a daily index representative of spatiotemporal monsoon trough variations. This index was used to determine the onset and retreat dates of the monsoon trough and their interannual fluctuations. They revealed that over 60% of TC genesis events were related to an active monsoon trough functioning as a background flow free of TC signals.

Hsu et al. (2008b) adopted a more dynamic approach for evaluating the contribution of TCs to WNP circulation in 2004 by applying a global circulation model (GCM). A series of hindcast experiments were conducted with two sets of simulations: one with realistic initial conditions including TC vortices and another in which TCs were not considered in the initial conditions. The seasonal mean and intraseasonal variance in both sets were integrated and compared. The second set exhibited a significant change in seasonal mean circulation and a reduction in intraseasonal variance with a ratio (40%–50%) similar to that derived directly from the empirical procedure in which TCs were removed from the reanalysis. The findings indicated the necessity of considering the contribution of TCs in GCM evaluation and the importance of their consideration in the realistic simulations of climate mean state and variability.

As shown in Hsu et al. (2008a,b) and Feng et al. (2020), the TC removal approach was effective in assessing the footprints of TCs in large-scale, low-frequency circulations. However, the TC removal scheme used by Hsu et al. (2008a,b), a spatial filtering scheme in a TC domain, was applied only to the low-level wind field, limiting the scope of the analysis to presenting a holistic picture of TC footprints. Moreover, the dynamic balance was not considered; therefore, more complex types of analyses, such as a budget analysis, could not be performed. Developing a new TC removal method is one approach for obtaining a holistic view of how TCs impact large-scale, low-frequency circulations. Herein, the potential vorticity inversion approach is adopted to isolate TC vortices from the global analysis.

1.3. Potential vorticity, PV inversion, and TC-removed data

Potential vorticity is largely considered to be a critical atmospheric variable. It is defined as a dot product

of absolute vorticity and stratification,

$$q = \frac{1}{\rho}(f + \nabla_3 \times \boldsymbol{u}_3) \cdot \nabla_3 \theta,$$

where f is the Coriolis parameter, ∇_3 is 3-dimensional differential operator, $\boldsymbol{u}_3$ is a 3-dimensional wind vector, θ is the potential temperature, and ρ is the density. PV is conserved when the heating source and friction are absent. This implies that the PV parcel on the material surface (i.e., isentropic surface) can be regarded as a tracer under the conservative condition. Thus, many studies used the PV to analyze weather systems in the middle troposphere, upper troposphere, and stratosphere (e.g., Brennan et al. 2008; Wernli and Sprenger 2007; Jones et al. 2003; Wirth et al. 2018; Archambault et al. 2013, 2015; Seiler 2019).

Another important feature of PV is the invertibility principle: if some relationships among wind field, mass field, and stratification are assumed, these fields are recovered by the PV distribution with appropriate boundary conditions. This approach is widely called the PV inversion (hereafter PVI). Thorpe (1985) was the first to demonstrate the invertibility of PV: assuming the axisymmetric structure and gradient wind balance, a balanced vortex structure (e.g., a tropical cyclone) can be diagnosed using PVI. Hoskins et al. (1985) also employed the same procedure and demonstrated idealized vortex structures induced by upper- and low-level PV anomalies. Moreover, many studies employed quasigeostrophic PV and its invertibility principle to analyze realistic data (Robinson 1988; Holopainen and Kaurola 1991; Hakim et al. 1996). Because the geostrophic wind is defined as a function of the geopotential, no assumption is needed to retrieve the mass field in the quasigeostrophic PVI framework. However, the analysis is restricted to the middle and high-latitude regions due to the quasigeostrophic assumption.

To analyze cyclones in the low-latitude region, Davis and Emanuel (1991) developed a PVI framework in which the balance wind equation is assumed. Wang and Zhang (2003) also developed a similar PVI framework. Here, the PVI framework by Davis and Emanuel (1991) and Wang and Zhang (2003) is introduced. Assuming that the irrotational and vertical winds are negligible in the divergence equation, the balance wind equation can be derived as follows:

$$\begin{aligned}\nabla^2\Phi &= \nabla \cdot (f\nabla\Psi) + 2\left[\frac{\partial^2\Psi}{\partial x^2}\frac{\partial^2\Psi}{\partial y^2} - \left(\frac{\partial^2\Psi}{\partial x \partial y}\right)^2\right] \\ &= f\nabla^2\Psi + \frac{df}{dy}\frac{\partial\Psi}{\partial y} + 2\left[\frac{\partial^2\Psi}{\partial x^2}\frac{\partial^2\Psi}{\partial y^2} - \left(\frac{\partial^2\Psi}{\partial x \partial y}\right)^2\right] \\ &\equiv f\nabla^2\Psi + N_b(\Psi), \end{aligned} \tag{1.1}$$

where Φ is geopotential, Ψ is streamfunction, and ∇ is the 2-dimensional differential operator. The balance wind equation shows the relationship between the geopotential and streamfunction. The approximate definition of PV in π $[= C_p(p/p_0)^{\kappa}]$ coordinate is written as

$$q = -\frac{g\kappa\pi}{p}\left(\eta\frac{\partial\theta}{\partial\pi} - \frac{\partial v}{\partial\pi}\frac{\partial\theta}{\partial x} + \frac{\partial u}{\partial\pi}\frac{\partial\theta}{\partial y}\right), \tag{1.2}$$

where $\kappa = R_d/C_p$ is the ratio of gas constant for dry air (R_d) and specific heat at constant pressure (C_p), p is pressure, p_0 is reference pressure (=1000 hPa), g is gravitational acceleration, u is eastward wind speed, v is northward wind speed, and η is the vertical component of absolute vorticity. Note that the terms including vertical velocity are neglected in the PV form. Because of focusing on TCs located at low latitudes where water vapor is rich, the moisture effect should be considered in the form of PV as demonstrated by Wang and Zhang (2003). Thus, the potential temperature (θ) in the PV form is replaced by the virtual potential temperature (θ_v):

$$q = -\frac{g\kappa\pi}{p}\left(\eta\frac{\partial\theta_v}{\partial\pi} - \frac{\partial v}{\partial\pi}\frac{\partial\theta_v}{\partial x} + \frac{\partial u}{\partial\pi}\frac{\partial\theta_v}{\partial y}\right), \tag{1.3}$$

where $\theta_v = (1 + 0.608s)\theta$, and s is the specific humidity. Assuming hydrostatic balance ($\theta_v = -\partial\Phi/\partial\pi$) and that the nondivergent wind is much greater than the irrotational wind, Eq. (1.3) can be rewritten as follows:

$$\begin{aligned}\frac{pq}{g\kappa\pi} &= (f + \nabla^2\Psi)\frac{\partial^2\Phi}{\partial\pi^2} - \frac{\partial^2\Psi}{\partial x\partial\pi}\frac{\partial^2\Phi}{\partial x\partial\pi} - \frac{\partial^2\Psi}{\partial y\partial\pi}\frac{\partial^2\Phi}{\partial y\partial\pi} \\ &\equiv (f + \nabla^2\Psi)\frac{\partial^2\Phi}{\partial\pi^2} - N_p(\Psi,\Phi).\end{aligned} \tag{1.4}$$

Equations (1.1) and (1.4) have two unknowns, which can be calculated by the method provided by Davis and Emanuel (1991) and Wang and Zhang (2003) using the q distribution, θ_v on the upper and bottom boundaries, and Φ and Ψ on the lateral boundaries. To solve the unknowns (Ψ and Φ) easily, two elliptic partial differential equations are derived. By subtracting Eq. (1.1) from Eq. (1.4) and multiplying a dimension-matching parameter ϵ_1, the following is obtained:

$$\left[\nabla^2 + \epsilon_1(f + \nabla^2\Psi)\frac{\partial^2}{\partial\pi^2}\right]\Phi = \frac{\epsilon_1 pq}{g\kappa\pi} + \epsilon_1 N_p(\Psi,\Phi) + N_b(\Psi) + f\nabla^2\Psi. \tag{1.5}$$

Adding Eq. (1.1) to Eq. (1.4) and multiplying a dimension-matching parameter ϵ_2 yields

$$\nabla^2\Psi = \left[\frac{\epsilon_2 pq}{g\kappa\pi} + \epsilon_2 N_p(\Psi,\Phi) - N_b(\Psi) + \nabla^2\Phi - \epsilon_2 f\frac{\partial^2\Phi}{\partial\pi^2}\right]\Big/\left(f + \epsilon_2\frac{\partial^2\Phi}{\partial\pi^2}\right). \tag{1.6}$$

Note that the parameters ϵ_1 and ϵ_2 must be set a positive (negative) value in Northern (Southern) Hemispheric region to hold the ellipticity in Eq. (1.5) and not to diverge to infinity on the right-hand side of Eq. (1.6), respectively. Equations (1.5) and (1.6) are solved by the successive over-relaxation method individually and repeatedly, and the solution is obtained when the variations of both unknowns are sufficiently small compared to the values in the previous step.

To recover the balanced mass and circulation fields associated with PV anomalies, the piecewise PV inversion (PPVI) method is employed following the method reported by Davis and Emanuel (1991). First, $\bar{\Phi}$ and $\bar{\Psi}$ satisfying Eqs. (1.1) and (1.4) for a given $\bar{q}$ must be defined:

$$\nabla^2\bar{\Phi} = \nabla\cdot(f\nabla\bar{\Psi}) + N_b(\bar{\Psi}), \tag{1.7}$$

$$\frac{p\bar{q}}{g\kappa\pi} = (f+\nabla^2\bar{\Psi})\frac{\partial^2\bar{\Phi}}{\partial\pi^2} - N_p(\bar{\Psi},\bar{\Phi}), \tag{1.8}$$

where $\bar{q}$ is an arbitrary averaged PV. By substituting $\Phi = \bar{\Phi} + \Phi', \Psi = \bar{\Psi} + \Psi'$, and $q = \bar{q} + q'$ into Eqs. (1.1) and (1.4) and using Eqs. (1.7) and (1.8), the PPVI system can be derived as

$$\nabla^2\Phi' = \nabla\cdot(f\nabla\Psi') + 2\left[\frac{\partial^2\Psi^*}{\partial x^2}\frac{\partial^2\Psi'}{\partial y^2} + \frac{\partial^2\Psi'}{\partial x^2}\frac{\partial^2\Psi^*}{\partial y^2} - 2\frac{\partial^2\Psi^*}{\partial x\partial y}\frac{\partial^2\Psi'}{\partial x\partial y}\right], \tag{1.9}$$

$$\begin{aligned}\frac{pq'}{g\kappa\pi} = {} & (f+\nabla^2\Psi^*)\frac{\partial^2\Phi'}{\partial\pi^2} + \frac{\partial^2\Phi^*}{\partial\pi^2}\nabla^2\Psi' \\ & - \left(\frac{\partial^2\Psi^*}{\partial x\partial\pi}\frac{\partial^2\Phi'}{\partial x\partial\pi} + \frac{\partial^2\Phi^*}{\partial x\partial\pi}\frac{\partial^2\Psi'}{\partial x\partial\pi} + \frac{\partial^2\Psi^*}{\partial y\partial\pi}\frac{\partial^2\Phi'}{\partial y\partial\pi} + \frac{\partial^2\Phi^*}{\partial y\partial\pi}\frac{\partial^2\Psi'}{\partial y\partial\pi}\right)\end{aligned} \tag{1.10}$$

where $[\ ]^* = \overline{[\ ]} + 1/2\,[\ ]' = 1/2\,([\ ] + \overline{[\ ]})$. First, two elliptic partial differential equations are derived from Eqs. (1.9) and (1.10) in the same manner as the total PVI solution procedure; then, given the PV anomaly (q'), geopotential deviation (Φ') and streamfunction deviation (Ψ') are solved in the PPVI system. The distributions of Φ' and Ψ' depend on the definition of $q'(= q - \overline{q})$, which in turn depends on how the averaged PV is defined. That is, the derived Φ' and Ψ' depend on the definition of $\overline{q}$. Therefore, care must be exercised when handling the arbitrary averaging of PV, which is discussed in greater detail in Section 3.2.

Although a more detailed procedure for constructing the TC removal data will be described in Sections 3.2 and 4.2, it is worthwhile to describe the physical meaning of TC removal data here. By the PPVI, dynamically balanced vortex structures are extracted from the 6-hourly reanalysis data, while the Rossby response induced by a

TC vortex and a response forced by TC's diabatic heating are not extracted. Therefore, by analyzing the TC-removed data, TC contribution (i.e., the in-situ TC footprint) to climate can be investigated directly, but the responses forced by TCs (i.e., remote TC effect such as downstream impact) cannot be investigated. This is the reason why a different approach (e.g., comparison of numerical simulation results) is needed to study the remote TC effect, but the PPVI can be used to build an initial field for the sensitivity experiment to extract TCs.

If no TCs existed in weather systems, a large-scale field would be expected to be modulated. Thus, the time series of the TC removed fields does not represent the time series obtained under the assumption of a weather system without TCs. The analysis of the TC-removal data allows us to estimate the TC footprints in large-scale fields, but it does not allow us to investigate the causality of the TC effects on climate directly. Numerical experiments would be necessary to explore the cause-and-effect relationship between TC and climate.

1.4. Aims and objectives

To obtain a comprehensive understanding of the TC contributions to the large-scale field, this study investigate the remote TC effect (i.e., downstream impact) on large-scale field and the in-situ TC footprints in climate using different approaches due to the applicability limitation of TC-removed data. The former is investigated by comparing simulation results of control and sensitivity experiments in which a TC in the initial condition is removed by the PPVI in Chapter 2. The latter is investigated by comparing analyses using the original and TC-removed data in Chapter 3 and Chapter 4.

The downstream impacts associated with TCs over the WNP, North Atlantic, and the south Indian Ocean have been reported (Grams et al. 2013a,b; Archambault et al. 2013, 2015; Grams and Archambault 2016; Quinting and Jones 2016; Keller et al. 2019) but reports of the downstream impact over other basins are lacking. Chapter 2 reports that a TC over the BoB strongly contributed to a heavy rainfall event in East Asia by a similar mechanism to the downstream impacts associated with TCs. This is the first report of remote impact by a TC over the BoB, which indirectly induced an extreme weather event in East Asia. In Chapter 3, the clustered TC footprints in the large-scale fields using the PVI technique are investigated. The PVI technique is applied to reanalysis data during June–October 2004 and the TC-removed fields are compared with the one by the traditional TC removal techniques. The TC footprints in intraseasonal variance and seasonal-mean circulation over the tropical WNP in the 2004 TC season discussed in Hsu et al. (2008b) are reexamined. By using almost the same PVI technique employed

in Chapter 3, Chapter 4 develops an understanding of the TC footprints in larger scale circulations, i.e., in the long-term climate means, interannual and interdecadal variabilities, and long-term trends, between 1958 and 2019. Finally, Chapter 5 concludes this study and presents implications for future work.

The contents of Chapter 2 and Chapter 3 have already been published in npj Climate and Atmospheric Science (Arakane et al. 2019) and Climate Dynamics (Arakane and Hsu 2020), respectively. The content in Chapter 4, excluding analyses of stability, genesis potential index, Pacific–Japan pattern, and propagations of quasi-biweekly and intraseasonal oscillations and Subsection 4.3.4, has also been accepted for publication (Arakane and Hsu 2021, © American Meteorological Society. Used with permission).

Chapter 2. Remote Effect of a Tropical Cyclone over the Bay of Bengal on a Heavy Rainfall Event in Subtropical East Asia

2.1. Introduction

Taiwan, an island off the east coast of Asia, receives a large amount of precipitation (climatological annual rainfall 2000–3000 mm). Steep topography, the East Asian monsoonal flow, fronts, and TCs are the causes of rainfall in Taiwan. Taiwan experiences five rainy seasons: winter, spring, Mei-Yu, typhoon, and fall (Chen and Chen 2003). The Mei-Yu season (May–June) in Taiwan is equivalent to the pre-flooding period in China. Mesoscale convective systems (MCSs) embedded in the Mei-Yu front are the major source of rainfall in the Mei-Yu season (Chen et al. 2006; Wang et al. 2016). The Mei-Yu front generally possesses a large gradient of equivalent potential temperature, which is associated with a convergence of cool dry air from the north and warm moist air from the southwest (Chen and Chang 1980; Chen and Chen 2003). In northern Taiwan, extreme rainfall events of as much as 600 mm of daily rain often occur when an MCS is supported by a strong low-level jet forming over the northern South China Sea (SCS, Chen and Yu 1988; Chen 1992, 2005). Recently, Tu et al. (2019) named the low-level jet over the SCS that transports warm moist air toward Taiwan effectively as the marine boundary layer jet (MBLJ).

On 2 June 2017, torrential rainfall occurred in northern Taiwan and continued throughout the next day. The Central Weather Bureau (CWB) in Taiwan reported that during the event, 2-hour and 12-hour rainfall amounts in northern Taiwan exceeding 120 mm and 600 mm, respectively. Flooding and landslides were induced by this heavy rainfall. Two people were killed, and three people were reported missing during this incident. The CWB reported that a Mei-Yu front associated with southwesterly winds induced the heavy rainfall event. The observed heavy rainfall (exceeding 600 mm in 12 hours) in this event was record-breaking for the events associated with a Mei-Yu front during the recent 26 years (Gong et al. 2015).

Before the heavy rainfall, TC Mora formed over the Bay of Bengal (BoB) on 28 May and dissipated on 31 May 2017. The Himawari-8 satellite images demonstrated the deep convection of TC Mora and the upper-level thin cloud accompanying the outflow to the north of TC Mora on 30 May 2017 (Figs. 2.1a,b). TC Mora dissipated at 0000 UTC 31 May 2017, but the thin cloud remained in the region to the northeast of the BoB. In the next few days, the thin cloud moved east over the East China Sea and a frontal system was observed to the northwest of

Taiwan. The frontal system shifted southeastward toward Taiwan on 2 June 2017 (Figs. 2.1c–f), and heavy rainfall occurred on the island (detail of southeastward movement of the frontal system will be discussed later). In addition, the southwesterly prevailed from the BoB to the northern SCS was enhanced following TC Mora. Because of the association of upper tropospheric perturbation and low-level southwesterly with TC Mora, the development of the front is hypothesized to be associated with TC Mora. A systematic study is required to investigate whether and how TC Mora contributed to the heavy rainfall.

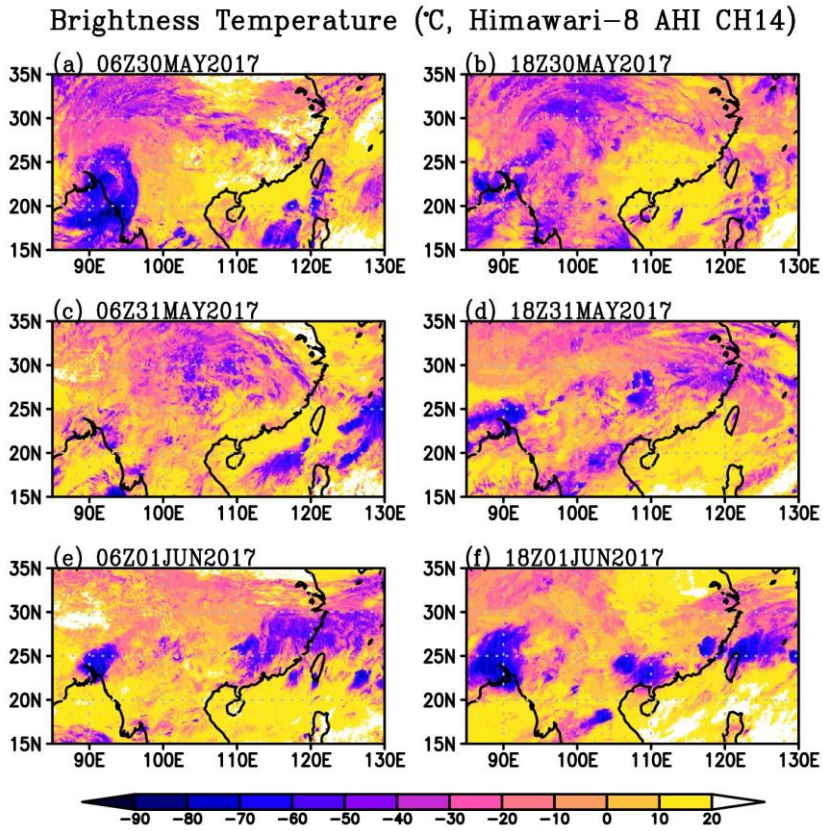

Fig. 2.1. The calculated brightness temperature (ºC) of Himawari-8 AHI channel 13 at (a) 0600 UTC 30 May, (b) 1800 UTC 30 May, (c) 0600 UTC 31 May, (d) 1800 UTC 31 May, (e) 0600 UTC 1 June, and (f) 1800 UTC 1 June 2017.

Did TC Mora help trigger or enhance the heavy rainfall? To answer the question, the effect of TC Mora on the heavy rainfall is assessed by conducting two sets of hindcast experiments, one with TC Mora included in the initial condition and one with TC Mora artificially removed from the initial condition.

This work is organized as follows: Section 2.2 describes data, a numerical model, and analyses employed in this work. In Subsection 2.3.1, an observed feature of the heavy rainfall event is described. An effect of TC Mora on heavy rainfall is discussed in Subsection 2.3.2 through comparative analyses of the control and the sensitivity

experiments by a numerical model. In Section 2.4, this work is summarized.

2.2. Data and methods

The brightness temperature retrieved from the Himawari-8 satellite data (Bessho et al. 2016) and the Global Satellite Mapping of Precipitation standard product (GSMaP; Kubota et al. 2020) are used. Furthermore, the Japanese 55-year reanalysis (JRA-55, Kobayashi et al. 2015; Harada et al. 2016) provided by the Japan Meteorological Agency is used. The JRA-55 used here is a 6-hourly 1.25° latitude–longitude gridded data set. These data are used to show a synopsis of the frontal rainfall and to validate the result of the control experiment.

The Geophysical Fluid Dynamics Laboratory (GFDL) finite-volume dynamical core (Lin and Rood 1997; Lin 1997, 2004) with the Global Forecast System (GFS) produced by NCEP is used (fvGFS, a global numerical weather prediction model, Hazelton et al. 2018). As the radiation scheme, the Rapid Radiative Transfer Model for general circulation models (Iacono et al. 2008) is used. The cumulus parameterization is the simplified Arakawa–Schubert scheme (Arakawa and Schubert 1974; Han and Pan 2011). The microphysics scheme is the six-class single-moment scheme developed by the GFDL (Lin et al. 1983; Chen and Lin 2013). The simulation is conducted with approximately 13-km horizontal resolution globally and 64 vertical levels with a model top at approximately 0.3 hPa. Using the NCEP-GFS analysis data, the experiment is initialized at 0000 UTC 29 May 2017 and integrated for 7 days. Although the horizontal resolution of the NCEP-GFS analysis data is coarser than that of the fvGFS simulation, the "initial shock" of convection in the simulation is suppressed within a day. The experiment captures the mature phase and dissipation of TC Mora over the BoB and the strong frontal rainfall system over northern Taiwan. This experiment is referred to as the control experiment.

A sensitivity experiment is conducted to investigate the influence of TC Mora on frontal rainfall over northern Taiwan. As in Hirota et al. (2016), using the potential vorticity inversion technique developed by Davis and Emanuel (1991), TC Mora is removed from the initial data used in the control experiment. After the removal of TC Mora, all dynamic variables (i.e., horizontal wind, vertical wind, temperature, geopotential height, and humidity) are modified to achieve dynamic balance in the initial data (Fig. 2.2). To quantify the model uncertainty, the sensitivity experiments with 11 ensemble members initialized with 99.9%–100.1% (with 0.02% increment) of the TC Mora vortex removed are conducted. Eleven simulations in the control experiment initialized with 99.9%–100.1% of the TC Mora are also conducted. The results of all ensemble members are quantitatively similar in both

experiments (Figs. 2.3 and 2.4), thus analyses will be conducted by ensemble data of the control and sensitivity experiments.

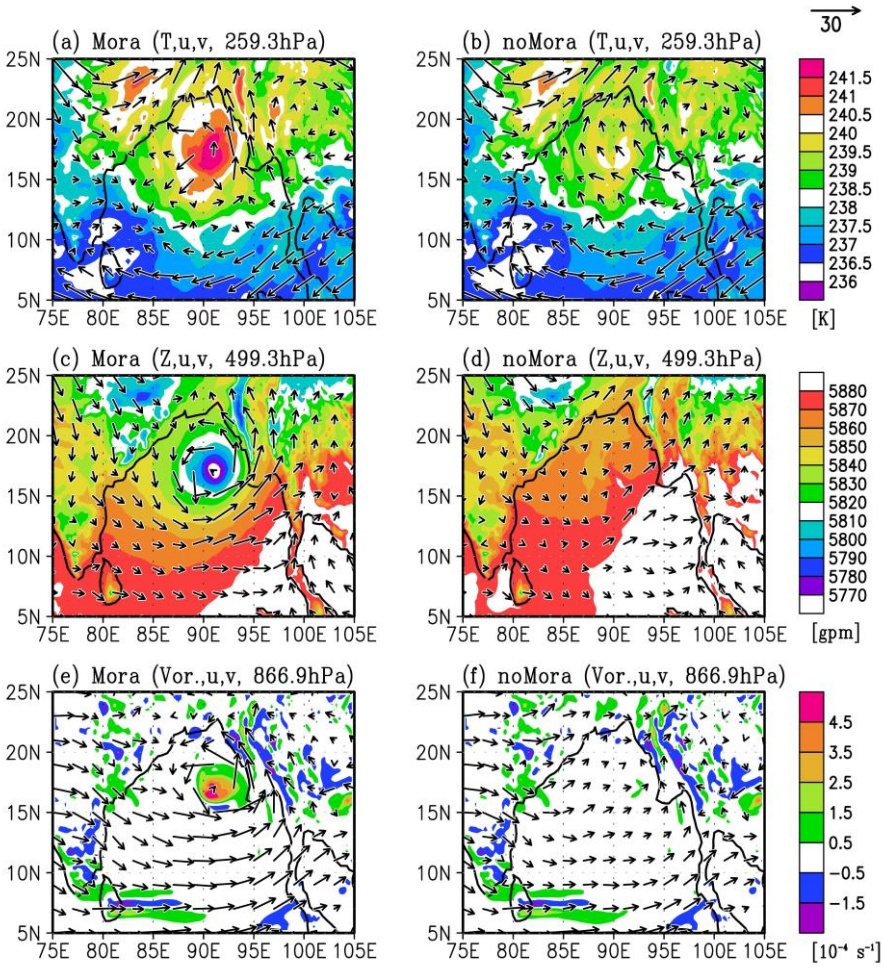

Fig. 2.2. Initial condition for the control (left-hand side) and sensitivity experiments (right-hand side) at 0000 UTC 29 May 2017. (a,b) Temperature (color, K) and horizontal wind (vector, m s^{-1}) at 259.3 hPa. (c,d) Geopotential height (color, gpm) and horizontal wind (vector, m s^{-1}) at 499.3 hPa. (e,f) Relative vorticity (color, s^{-1}) and horizontal wind (vector, m s^{-1}) at 866.9 hPa.

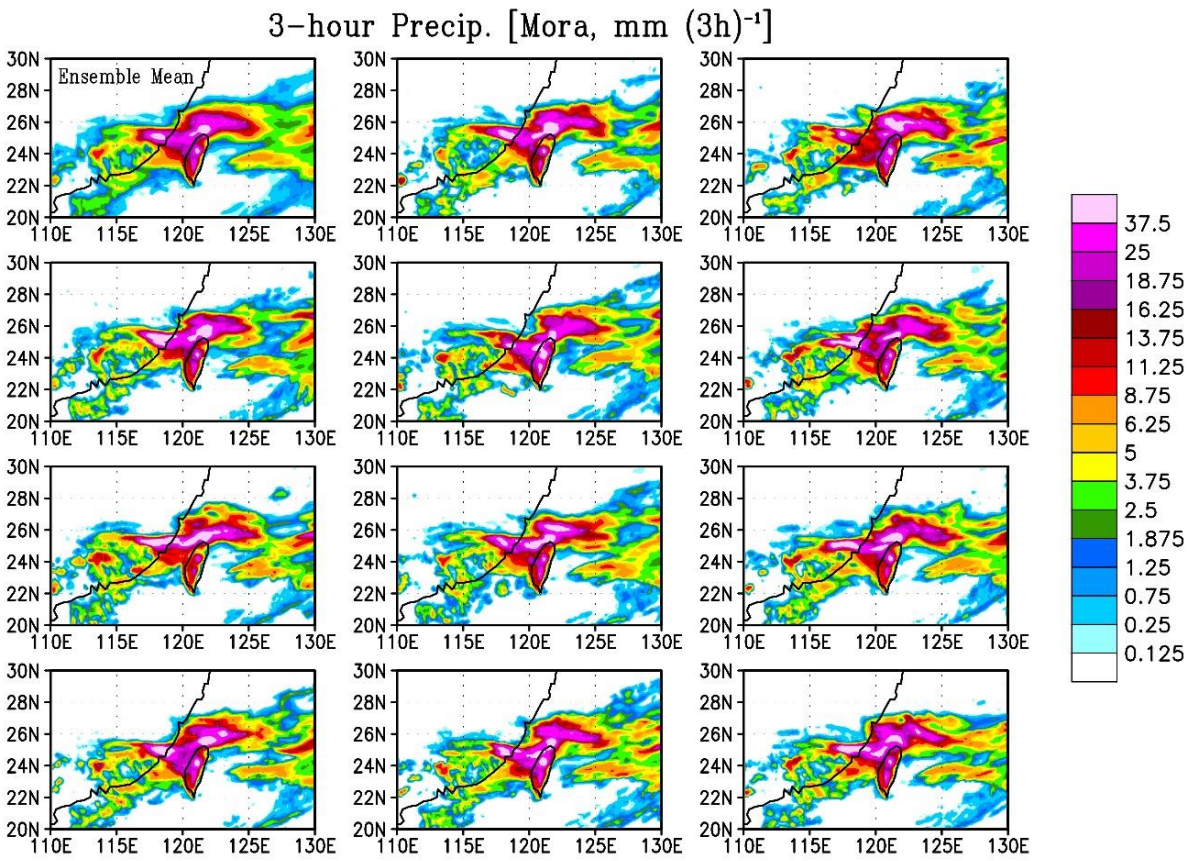

Fig. 2.3. Three-hourly accumulated rainfall [mm $(3h)^{-1}$] of the control ensemble simulations. The start time of the 3-hourly rainfall accumulation is 0000 UTC 2 June 2017. The top-left corner panel denotes ensemble mean precipitation and the others denote individual simulated precipitation.

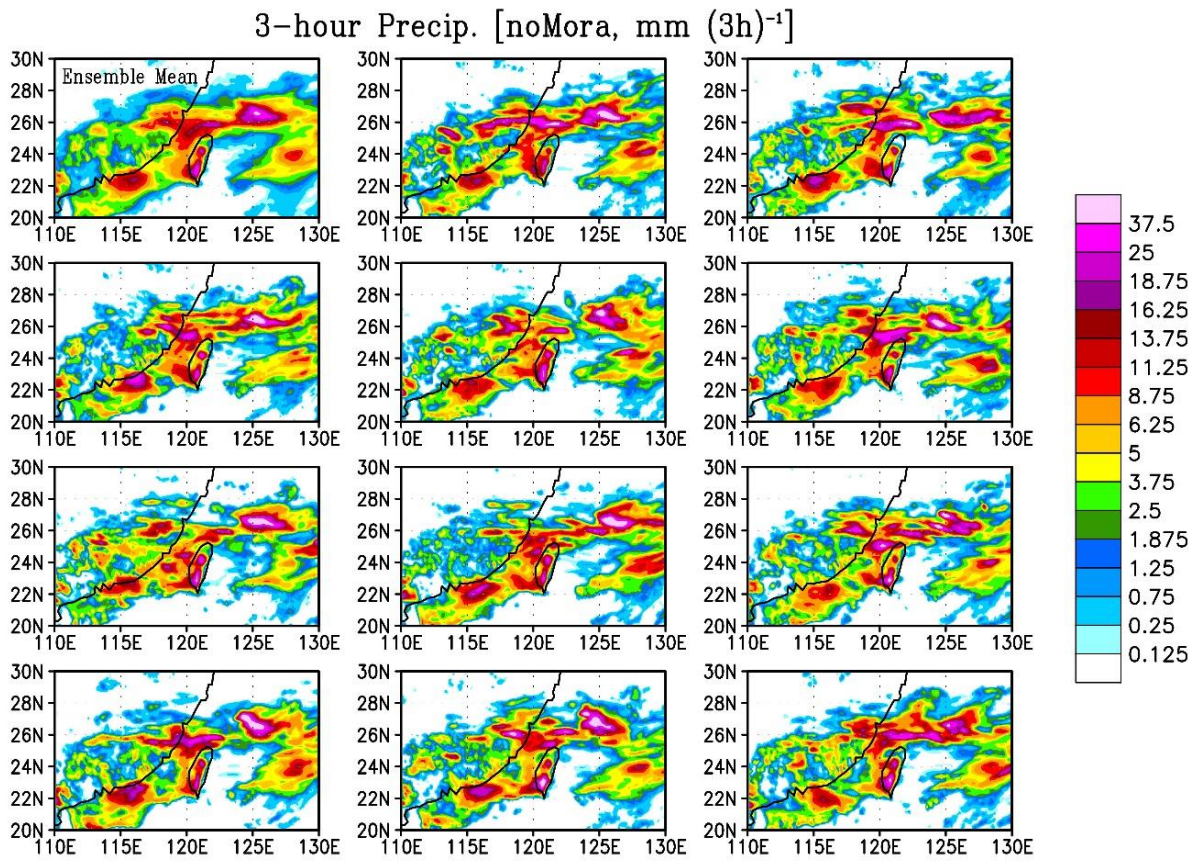

Fig. 2.4. As in Fig. 2.3, but for the sensitivity ensemble simulations.

The frontogenetical function budget analysis (Ogura and Portis 1982) is conducted to study the development of the frontal system near Taiwan. The budget equation for frontogenetical function is expressed as follows:

$$F_{\mathrm{G}} = F_{\mathrm{div}} + F_{\mathrm{def}} + F_{\mathrm{tilt}} + F_{\mathrm{diab}},$$

where F_{G} is the frontogenetical function, F_{div} is the divergence term, F_{def} is the deformation term, F_{tilt} is the tilting term, and F_{diab} is the diabatic term. The terms are expressed in pressure coordinates as follows:

$$\begin{aligned}
F_{\mathrm{G}} &= \frac{d}{dt}|\nabla_{\mathrm{h}}\theta_e|, \\
F_{\mathrm{div}} &= -\frac{1}{2}|\nabla_{\mathrm{h}}\theta_e|\delta, \\
F_{\mathrm{def}} &= -\frac{1}{|\nabla_{\mathrm{h}}\theta_e|}\left[\frac{1}{2}\left\{\left(\frac{\partial\theta_e}{\partial x}\right)^2 - \left(\frac{\partial\theta_e}{\partial y}\right)^2\right\}D_1 + \frac{\partial\theta_e}{\partial x}\frac{\partial\theta_e}{\partial y}D_2\right], \\
F_{\mathrm{tilt}} &= -\frac{1}{|\nabla_{\mathrm{h}}\theta_e|}\frac{\partial\theta_e}{\partial p}\nabla_h\theta_e \cdot \nabla_h\omega, \\
F_{\mathrm{diab}} &= \frac{1}{|\nabla_{\mathrm{h}}\theta_e|}\nabla_h\theta_e \cdot \nabla_h\left(\frac{d\theta_e}{dt}\right),
\end{aligned}$$

where θ_e is the equivalent potential temperature, ∇_h is the horizontal differential operator, $d/dt = \partial/\partial t + u\partial/\partial x + v\partial/\partial y + \omega\partial/\partial p$ is the total derivative, u is the zonal wind, v is the meridional wind, and ω is the pressure velocity; $\delta \equiv \partial u/\partial x + \partial v/\partial y$ is the divergence, $D_1 \equiv \partial u/\partial x - \partial v/\partial y$ is the stretching deformation, and $D_2 \equiv \partial v/\partial x + \partial u/\partial y$ is the shearing deformation. The preceding budget calculation is applied to demonstrate that TC Mora enhanced the divergence and deformation terms and thus considerably contributes to the formation of the front near northern Taiwan.

2.3. Results

2.3.1. Observation

Figure 2.5 shows the satellite-based rainfall with low-level horizontal wind and a wind shift line (WSL). Following Yeh et al. (2002), the WSL is defined as a boundary where the horizontal wind direction is abruptly changed. Because it is difficult to detect the leading edge of the "frontal zone" using thermal variables in this case, the WSL is used to show the approximate location of air masses' boundary (i.e., the leading edge of a baroclinic zone) near Taiwan. The WSL is in eastern China at 0000 UTC 1 June 2017 (Fig. 2.5b) and moving southeastward. Accompanied by the movement of the WSL, the well-organized frontal rainfall system shifts to the southeast with time. As shown in Fig. 2.5, the heavy rainfall over northern Taiwan starts between 1200 UTC 1 June and 0000 UTC 2 June 2017.

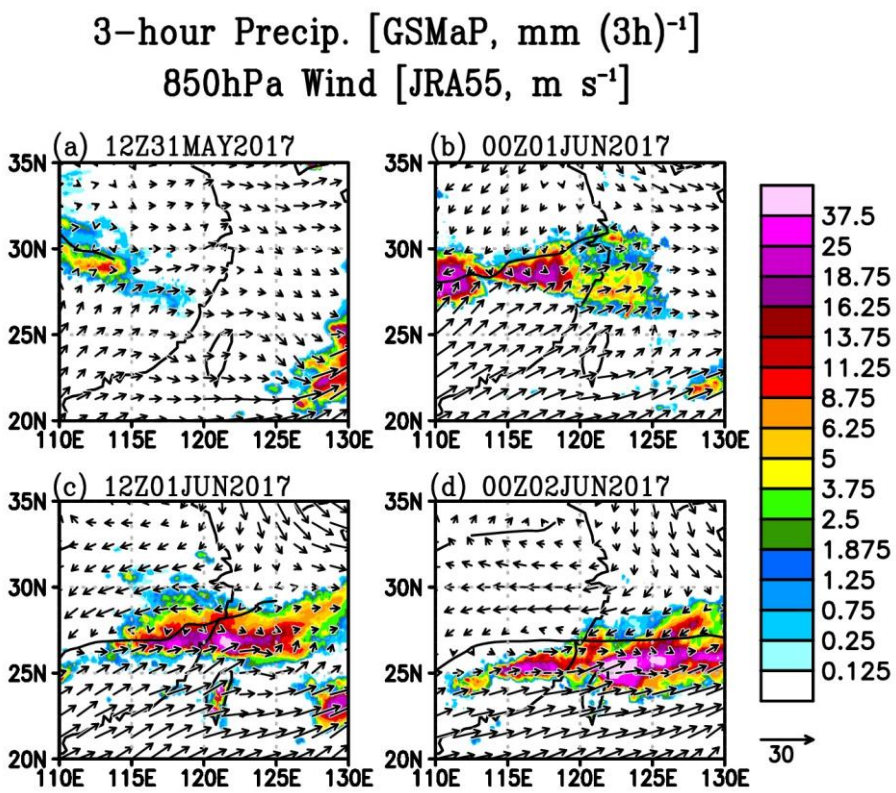

Fig. 2.5. Three-hourly accumulated rainfall [mm $(3h)^{-1}$] obtained from the GSMaP. The start time for the 3-hourly rainfall accumulation is (a) 1200 UTC 31 May, (b) 0000 UTC 1 June, (c) 1200 UTC 1 June, and (d) 0000 UTC 2 June 2017. Vectors represent 850-hPa horizontal wind and the solid lines show the wind shift lines obtained from the JRA-55 at the start time for precipitation accumulation.

Next, the synopsis of the heavy rainfall system after the onset of heavy rainfall over northern Taiwan (at 1800 UTC 1 June 2017) is analyzed. The upper-level northerly wind component and subsidence are observed to the north of Taiwan (approximately 40°N, 125°E) along the western periphery of an upper-level trough (Fig. 2.6a). Furthermore, the subsiding northerly wind is observed to the north of the WSL in the cross-section along 121°E (Figs. 2.7c,d). Thus, the low-level northerly wind situated to the north of Taiwan shown in Fig. 2.5 is vertically linked with the upper-level system. Conversely, the low-level southwesterly wind toward Taiwan transports moisture-laden air to Taiwan. As a result, the low-level southwesterly and northerly winds create a large moisture flux convergence near Taiwan (Fig. 2.6b). The vertical cross-section from 25°N, 117.5°E to 20°N, 120°E shown in Fig. 2.6c reveals that the strong low-level southwesterly wind (i.e., a MBLJ) is confined below 850 hPa as in many case studies of the Mei-Yu fronts. Compared with a climatology of MBLJ using the National Centers for Environmental Prediction (NCEP) Climate Forecast System Reanalysis (CFSR) data from 2008 to 2012 during May–June with 6-hourly 0.5° latitude-longitude grids conducted by Tu et al. (2019), in this case, the maximum

speed of MBLJ is 50% larger than its 5-year climatology (19 m s^{-1} versus 12.5 m s^{-1}). Note that the horizontal resolution of JRA-55 used here is coarser than the CFSR data (1.25° versus 0.5°). A higher resolution data might yield an even stronger MBLJ.

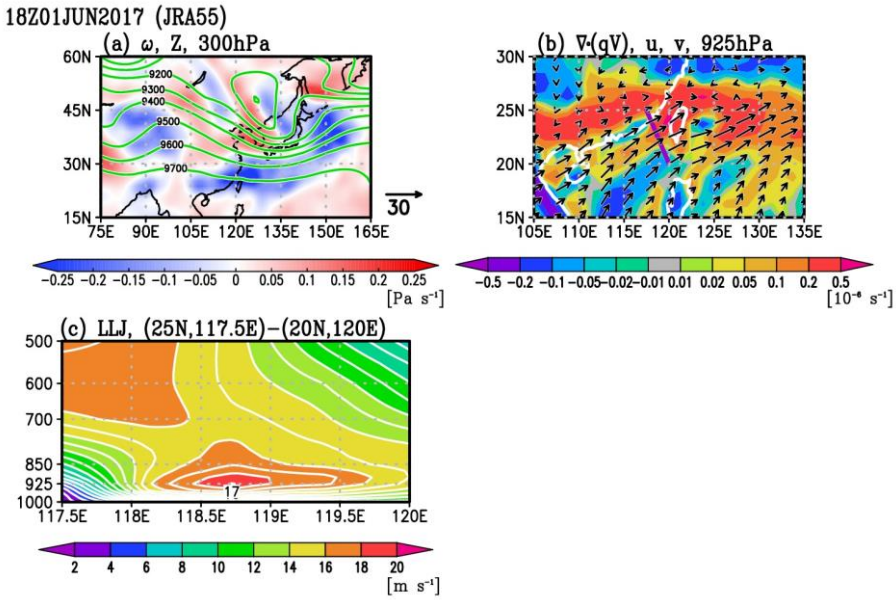

Fig. 2.6. Synopsis of the heavy rainfall obtained from the JRA-55 at 1800 UTC 1 June 2017. (a) Daily averaged vertical pressure velocity (color, Pa s^{-1}) and geopotential height (contour, gpm) at 300 hPa. (b) Daily averaged moisture (specific humidity) flux convergence (color, s^{-1}) and horizontal wind (vector, m s^{-1}) at 925 hPa. (c) Vertical cross section of daily-averaged horizontal wind component perpendicular to the section (color and contour, contour interval is 1 m s^{-1}). Location of the cross section is indicated as the purple-colored solid line in (b).

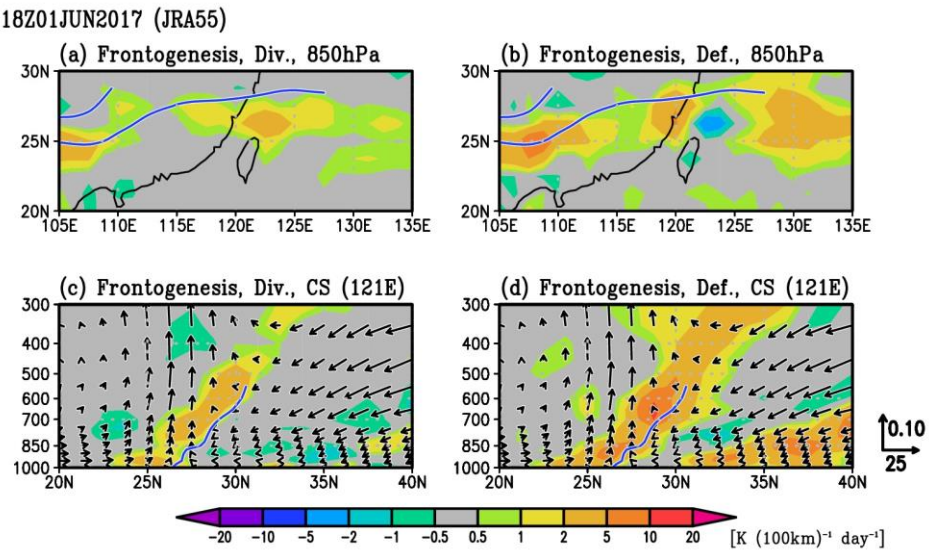

Fig. 2.7. Daily averaged frontogenetical function term [color, K (100 km)$^{-1}$ day^{-1}] with the wind shift line (blue line) obtained from the JRA-55 at 1800 UTC 1 June 2017. (a) Divergent and (b) deformation terms at 850 hPa, and vertical cross section of (c) divergence and (d) deformation terms and daily averaged transverse circulation (vector, m s^{-1}) along 121°E (the plotted data are zonally averaged between 119°E and 123°E).

Finally, the frontal development induced by the horizontal confluent flow is investigated. Along with the WSL, both the divergence and deformation terms of the frontogenetical function (F_{div} and F_{def}, respectively), which are the dominant terms in the budget equation, are positive at the low level (Figs. 2.7a,b). This means that low-level convergence and deformation induced by the northerly wind to the north of Taiwan and the MBLJ to the southwest of Taiwan positively contribute to the frontal development. The north–south vertical cross-sections of F_{div} and F_{dev} also show the positive contributions of divergence and deformation terms to the frontal development in the south of the WSL that tilts northward with height (Figs. 2.7c,d). A noteworthy feature is the distinguished upward motion over the positive F_{div} and F_{def} near the surface where large precipitation occurs near the front.

2.3.2. Numerical simulations

The contribution of TC Mora to the frontal rainfall system is revealed by contrasting the control experiment and sensitivity experiment in which TC Mora is removed using the fvGFS. The simulated 3-h accumulated precipitation is shown in Fig. 2.8. In the control experiment, although the 13-km spatial resolution used for the experiments is not sufficiently high to resolve the steep topography in Taiwan, the characteristics of the

heavy rainfall system over northern Taiwan is realistically reproduced: well-organized rainfall system with an amount comparable to the observed (Figs. 2.8a,b). Furthermore, as revealed in the JRA-55, the rainfall system shifts to the southeast along with the southeastward movement of the simulated WSL (black-colored solid lines). By contrast, the rainfall system simulated in the sensitivity experiment is less organized with a smaller amount of rainfall (Figs. 2.8c,d). Also, the WSL in the sensitivity experiment always stays to the north of the one simulated in the control experiment (red-colored solid lines). This suggests that the boundary of air masses to the north of Taiwan shifts further southward because of the further equatorward penetration of northerly wind under the influence of TC Mora.

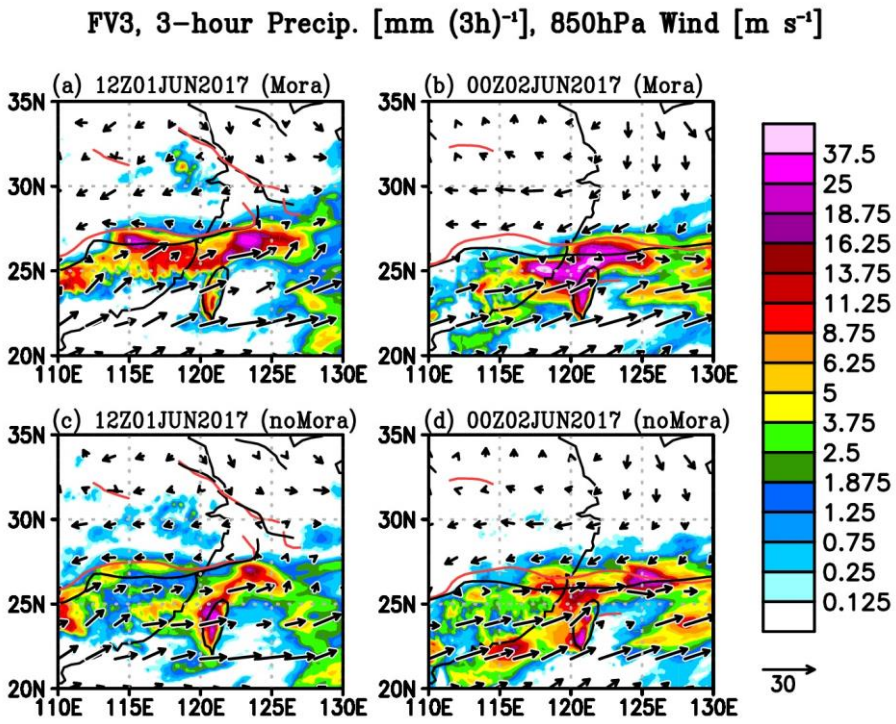

Fig. 2.8. (a,b) As in Figs. 2.5c,d, respectively, but for ensemble of the control experiment. (c,d) As in Figs. 2.5c,d, respectively, but for ensemble of the sensitivity experiment. The black- and red-colored solid lines show the wind shift lines in ensembles of the control and sensitivity experiments, respectively.

The existence of TC Mora modulates other dynamic fields over East Asia as well. Figures 2.9a,b show the simulated upper-level fields. As revealed in the JRA-55, the subsiding northerly wind component along the western periphery of the upper-level trough to the north of Taiwan is well simulated in the control experiment (Fig. 2.9a). In the sensitivity experiment, the location and strength of the upper-level trough and vertical motion differ from the results in the control experiment (Fig. 2.9b). This can be seen clearly in the differences between the two

experiments. As shown in Fig. 2.9c, a wave-like pattern is seen centered around the Korean Peninsula in the difference between the control and sensitivity experiments. As a result, the enhancement of northerly wind and subsidence over the Yellow Sea (approximately 35°N, 123°E) are simulated in the control experiment. This means that the existence of TC Mora enhances the subsiding northerly wind to the north of Taiwan by modulating the upper-level circulation. Note that the subsiding northerly wind prevails through the entire troposphere as seen in Figs. 2.7c,d. Therefore, the existence of the upper-level trough plays an important role in inducing the northerly wind. To confirm how TC Mora modulates the upper-level circulation, the temporal evolution of differences in the upper-level streamfunction and wave activity flux (WAF, Takaya and Nakamura 2001) between the control and sensitivity experiments are investigated. The streamfunction differences indicate the development of a wave-like structure emanating northeastward from the tip of the BoB, as indicated by the WAF similar to the Rossby wave dispersion triggered by a heat source (Fig. 2.10). This contrast between the two experiments suggests that TC Mora modulates the upper-level structure over East Asia through the processes of northeastward wave energy propagation and the modulated upper-level field enhances the northerly wind and subsidence to the north of Taiwan and the associated frontogenesis.

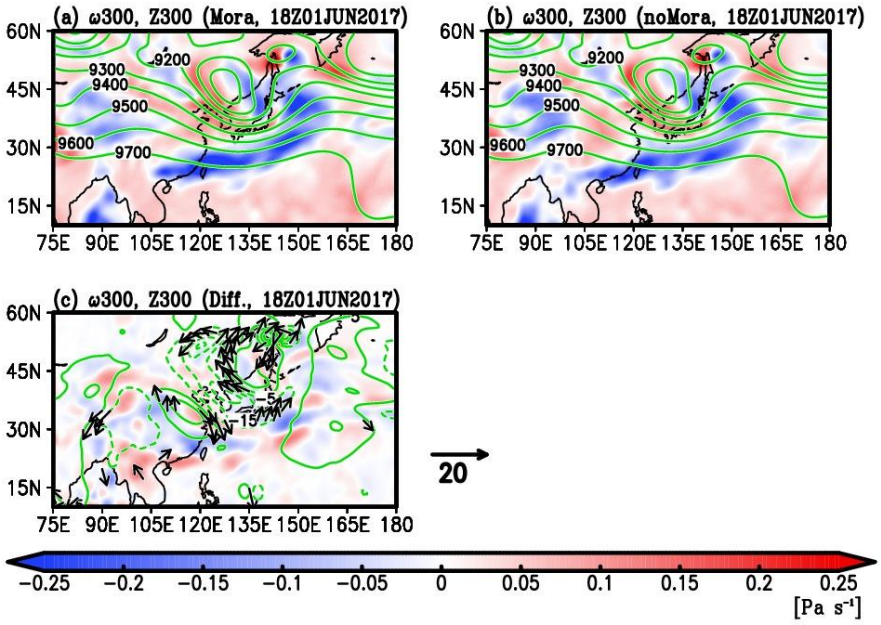

Fig. 2.9. Daily averaged vertical pressure velocity (color, Pa s^{-1}) and geopotential height (contour, gpm) at 300 hPa at 1800 UTC 1 June 2017. (a) Ensemble of the control experiment, (b) ensemble of the sensitivity experiment, and (c) difference between ensembles of the control and sensitivity experiments (contour interval is 10 gpm) with daily-averaged 300-hPa horizontal wind difference (vector: the wind vector is omitted where its magnitude is smaller than Pa s^{-1}).

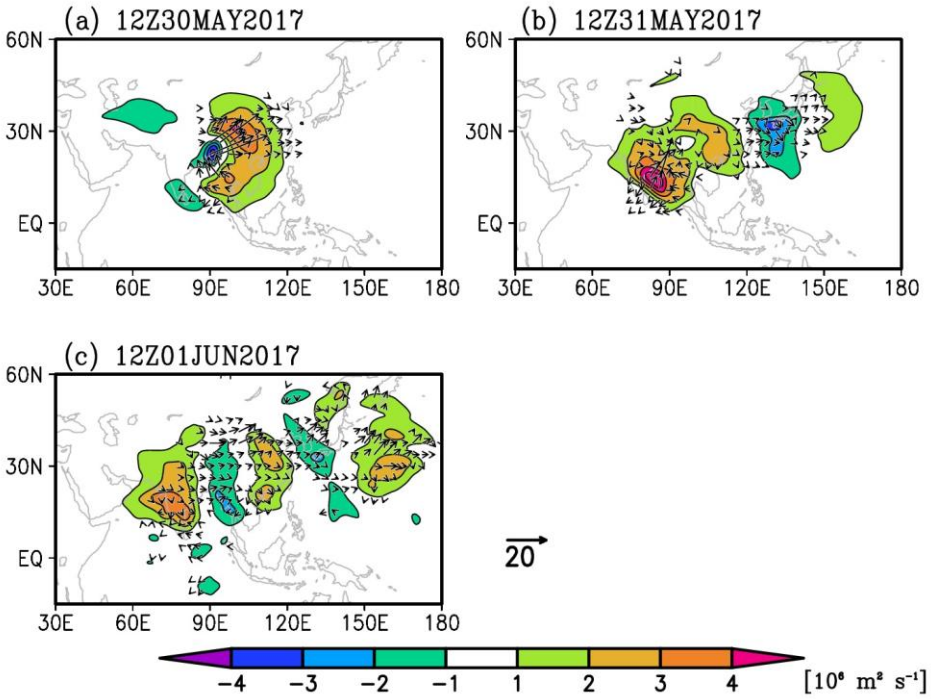

Fig. 2.10. Differences in streamfunction (color, $m^2\ s^{-1}$) and the wave activity fluxes (vector: the vector is omitted where its magnitude is smaller than 1 $m^2\ s^{-2}$) between ensembles of the control and sensitivity experiments at 300 hPa. (a) 1200 UTC 30 May, (b) 1200 UTC 31 May, and (c) 1200 UTC 1 June 2017.

In addition to enhancing the upper-level fields, TC Mora modulates the low-level fields around Taiwan to favor the development of the frontal system. The observed low-level southwesterly wind toward Taiwan, large moisture flux convergence, and the MBLJ are reproduced in both experiments (Figs. 2.11a,b and 2.12). However, Fig. 2.12 shows that the MBLJ in the control experiment is notably stronger and wider than in the sensitivity experiment (e.g., the MBLJs maximum speed in both experiments are approximately 18.7 and 17.0 m s^{-1}, respectively), especially in the area closer to Taiwan (i.e., 119°E–120°E). The moisture flux convergence around Taiwan is therefore much stronger in the control experiment (Fig. 2.11c). It follows that the existence of TC Mora enhances the MBLJ, which transports a large amount of low-level moisture toward Taiwan, and thus a considerably favorable condition for heavy rainfall is created in northern Taiwan.

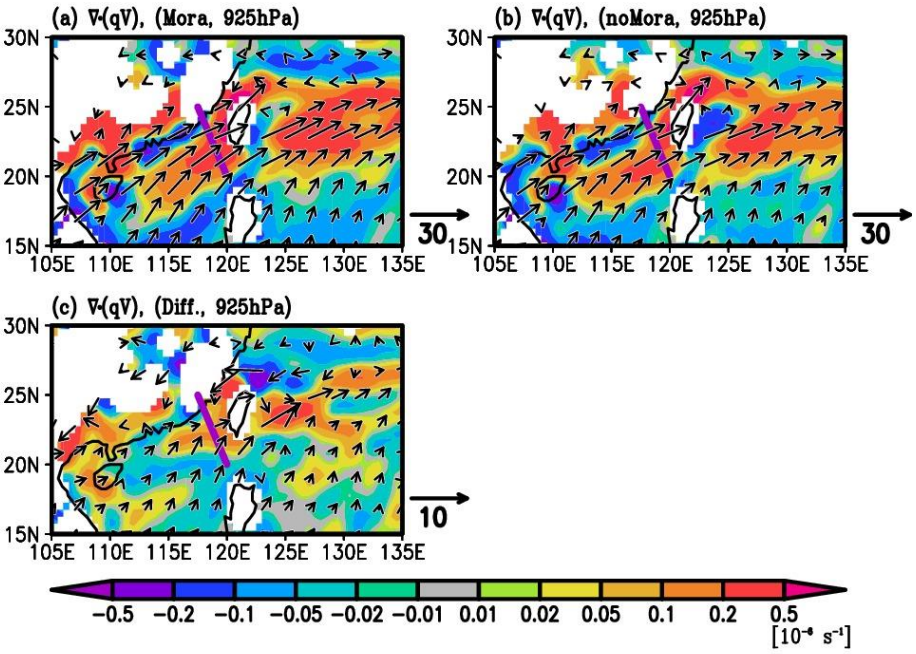

Fig. 2.11. Daily averaged moisture (specific humidity) flux convergence (color, s^{-1}) and horizontal wind (vector, m s^{-1}) at 925 hPa at 1800 UTC 1 June 2017. (a) Ensemble of the control experiment, (b) ensemble of the sensitivity experiment, and (c) difference between ensembles of the control and sensitivity experiments.

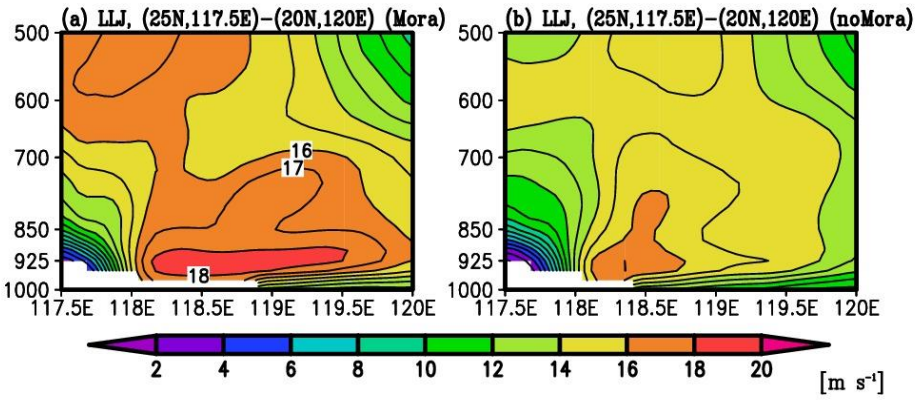

Fig. 2.12. Vertical cross section of daily-averaged horizontal wind component perpendicular to the section (color and contour, contour interval is 1 m s^{-1}) at 1800 UTC 1 June 2017. (a) Ensemble of the control experiment and (b) ensemble of the sensitivity experiment. Location of the cross section is indicated as the purple-colored solid line in Figs. 2.11a,b.

Although TC Mora changes the location of the front through modulating dynamic fields over East Asia, how TC Mora contributes to the frontal intensity needs to be evaluated. The low-level positive contributions by F_{div} and F_{def} to the frontal development near Taiwan are well reproduced in the control experiment as in the JRA-55 analysis (Figs. 2.13a,d). Compared with the sensitivity experiment, a larger positive contribution near

northern Taiwan (approximately 25°N, 121°E) is simulated in the control experiment (Figs. 2.13b,e). This is reflected in the differences between the experiments shown in Figs. 2.13c,f. Moreover, the north–south vertical cross-sections of F_{div} and F_{def} also show results more consistent with the JRA-55 analysis (Fig. 2.14). In the control experiment, Fig. 2.14 shows that larger positive contribution to the frontal development along the WSL, stronger northerly wind originated in the upper level to the north of WSL, stronger southerly wind originated in the tropic to the south of WSL, and stronger upward motion over the WSL than in the sensitivity experiment. Notably, Figs. 2.14c,f show that the MBLJ and the subsiding northerly wind toward Taiwan are enhanced in the control experiment. Furthermore, although the positions of air masses' boundaries at 850–600 hPa level in both experiments are almost identical at 1800 UTC 1 June 2017, the positions notably become different 6 hours later (Figs. 2.14d,h). Both WSLs have tilted structures from low level to middle level, however, the stronger northerly wind in the control experiment nudges the WSL further south. This implies that the enhancement of the dry northerly and moist southerly winds induced by TC Mora do have a large impact on the frontal system. As a result, the enhanced confluence induced by TC Mora not only shifts the location of the baroclinic zone but also creates stronger baroclinicity and moisture convergence near Taiwan.

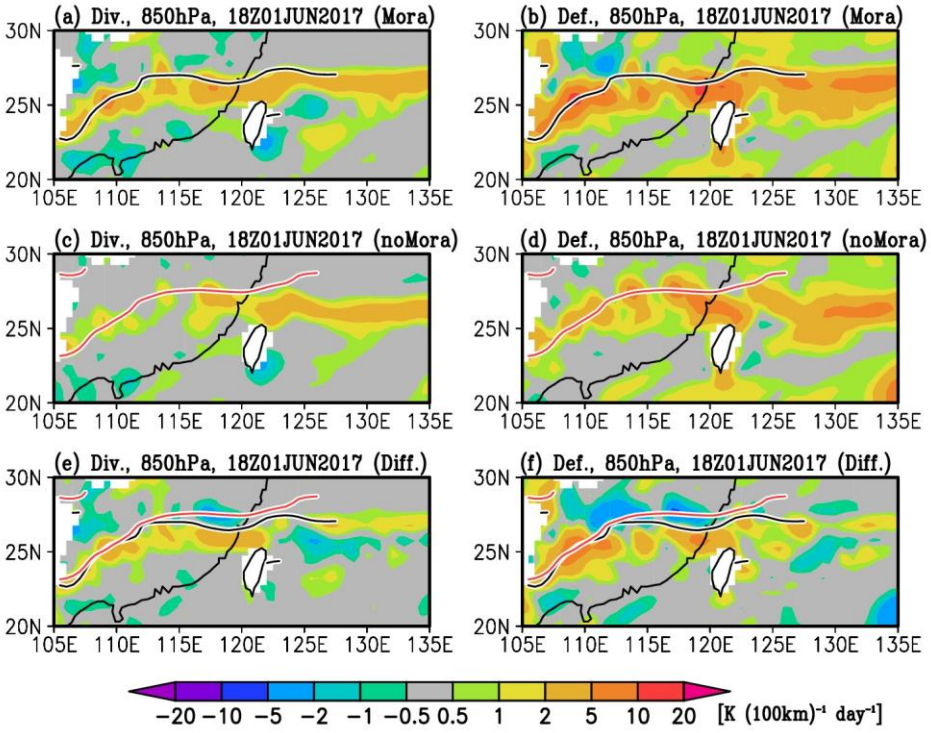

Fig. 2.13. Daily averaged 850-hPa (left) divergent and (right) deformation terms [color, K (100 km)$^{-1}$ day^{-1}] in the frontogenetical function with the wind shift line at 1800 UTC 1 June 2017. (a,d) Ensemble of the control experiment, (b,e) ensemble of the sensitivity experiment, and (c,f) difference between ensembles of the control and sensitivity experiments. The black-colored and red-colored solid lines denote the wind shift lines in ensembles of the control and sensitivity experiments, respectively.

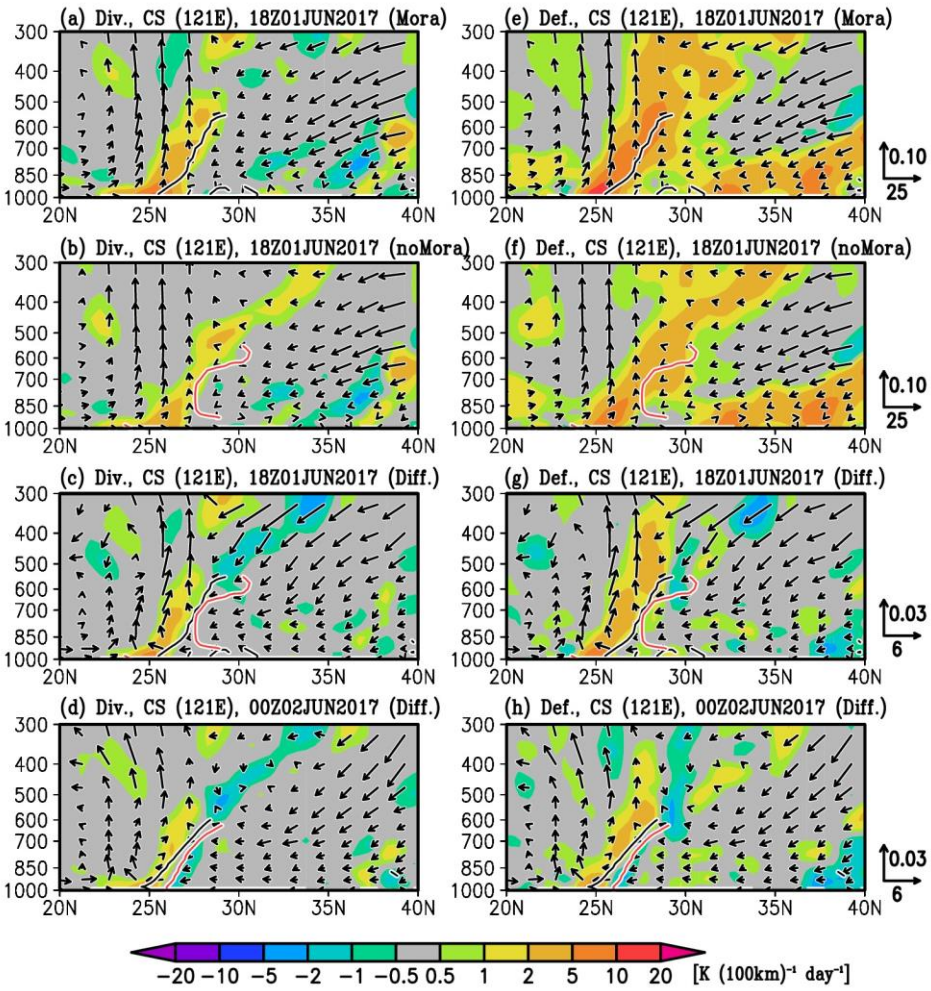

Fig. 2.14. Vertical cross section (along 121°E) of daily-averaged (left) divergent and (right) deformation terms [color, K (100 km)$^{-1}$ day^{-1}] in the frontogenetical function with the wind shift line at 1800 UTC 1 June 2017. (a,e) Ensemble of the control experiment, (b,f) ensemble of the sensitivity experiment, and (c,g) difference between ensembles of the control and sensitivity experiments. (d,h) As in (c,g), respectively, but at 0000 UTC 2 June 2017. The black-colored and red-colored solid lines denote the wind shift lines in ensembles of the control and sensitivity experiments, respectively.

2.4. Conclusion

It was demonstrated how TC Mora over the BoB led to the torrential rainfall event over northern Taiwan on 2 June 2017. This event resulted from the modification of upper-level large-scale and low-level synoptic-scale circulation (namely, the Mei-Yu front). The fvGFS that realistically simulated the torrential rainfall event starting 4 days in advance was used to conduct two hindcast experiments: a control experiment with TC Mora embedded in the initial condition and a sensitivity experiment initialized with TC Mora removed. By analyzing the contrasting

results, the physical processes induced by TC Mora that led to the torrential rainfall event were identified. As shown in the schematic diagram (Fig. 2.15), the mechanisms are described as follows:

(1) TC Mora remotely and extensively affected circulation over East Asia.

(2) The effect on circulation enhanced the southwesterly winds over the SCS to the southwest of Taiwan and the northerly winds to the north of Taiwan.

(3) The strengthened and widened marine boundary layer jet over the SCS transported moisture-laden air toward Taiwan and enhanced low-level moisture convergence near Taiwan.

(4) The strong northerly winds moved cooler air mass farther southward in the north of Taiwan and promoted the enhancement of low-level convergence.

(5) The stronger confluent zone induced by the strengthening of the warm moist southerly and cool dry northerly winds resulted in a strong baroclinic zone (front), which shifted further southward toward northern Taiwan through the deformation and divergence processes.

(6) The enhanced low-level moisture convergence and frontal system generated heavy rainfall over northern Taiwan.

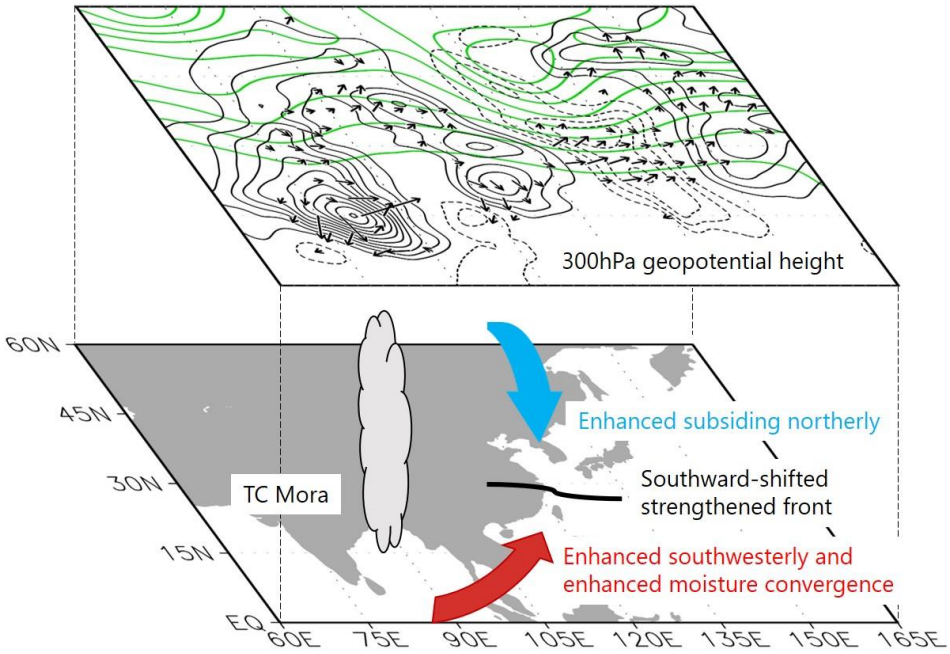

Fig. 2.15. Schematic diagram of the heavy rainfall in Taiwan on 2 June 2017. Green contour shows 300-hPa geopotential height. Black contour and vector show the deviations of geopotential height and horizontal wind induced by TC Mora at 300 hPa, respectively.

One may suspect that the event reported here is like a PRE. In a PRE, low-level moisture-rich tropical air is transported by a TC's outer (synoptic-scale) circulation to a frontal zone located in the north and triggers heavy rainfall in the frontal zone (Galarneau et al. 2010). At the first look, the 2 June 2017 event seemingly exhibited some similarities. However, different characteristics were observed in this event. One is that statistical distances between the TC and frontal zone in PREs are 410–1700 km (Galarneau et al. 2010), whereas the distance between TC Mora over the BoB and the frontal zone to the north of Taiwan over the WNP was approximately 3500 km. Thus, the direct contribution of TC outflow to the heavy rain event was extremely low. The other is that, remarkably, numerical experiments revealed that TC Mora modified the evolution of the large-scale circulation, for example, by enhancing the overall low-level cyclonic circulation and emanating a wave-like structure that modified the upper-level circulation over East Asia. The former increased the moisture transport from the SCS, and the latter induced strong cyclonic circulation in the north along with the southward penetration of cool dry air. These modifications suggest that TC Mora remotely enhanced the vertical coupling and the tropical–extratropical interaction in East Asia and led to the extreme rainfall event in northern Taiwan.

Chapter 3. Tropical Cyclone Footprint in Large-Scale Circulation over the Western North Pacific: A Case Study

3.1. Introduction

Many studies have revealed the large-scale environmental effects on a TC during its life cycle: genesis (Gray 1998; Ritchie and Holland 1999), development (DeMaria 1996; Ritchie and Frank 2007; Hendricks et al. 2010), and movement (Franklin et al. 1996; Sobel and Camargo 2005; Galarneau and Davis 2013). By contrast, few studies have considered the effects exerted by TCs on the large-scale environment. By comparing original reanalysis data with TC-removed data, Hsu et al. (2008a,b) demonstrated that TCs contributed more than 50% to intraseasonal variance (ISV) of 850-hPa vorticity along TC tracks over the tropical WNP during boreal summers when TC and intraseasonal oscillation (ISO) activities were strong. Ko et al. (2012) also used the same method and demonstrated that TCs enhanced the amplitudes of vorticity and kinetic energy of the TC/submonthly wave pattern over the WNP by more than 50%. The TC removal technique proposed by Kurihara et al. (1995) [hereafter Kurihara filtering (KF)], which was applied in the procedure of the TC bogus initialization, was employed in their studies. The procedure of KF is described briefly as follows. An 850-hPa wind field was divided into basic and disturbance fields, and its TC center and domain were then determined using the tangential wind profile of the disturbance field. For all atmospheric variables, the disturbance field within the TC domain was removed.

The KF has been widely used in TC numerical experiments (Cheung and Chan 1999; Wu et al. 2002; Kwon et al. 2002; Rogers et al. 2003). Ross and Kurihara (1995) used the KF to create an initial field of sensitivity experiment in which a TC was removed. Moreover, in a dynamical initialization scheme for TC simulations, Cha and Wang (2013) and Wang et al. (2013) employed the KF to separate the TC vortex component and the environmental component. To compute the large-scale vertical wind shear, Wang et al. (2015) used the filtered basic wind field obtained by the KF.

The employment of this type of TC removal technique is a powerful way to investigate TC contributions to the large-scale environments. However, results obtained by the KF have some problems. First, although a TC sometimes tilts vertically, the center and domain are fixed at all layers because they are determined by the 850-hPa wind field only. Second, the dynamic balance is not considered in both the TC-removed component and the remaining circulation. The consideration of the dynamic balance in the TC removal fields is important when other

dynamic fields, e.g., vertical velocity, temperature, and geopotential fields, are analyzed to obtain a complete structure associated with TC. These inherent problems in the KF are partially dealt with in the new TC removal technique proposed by Winterbottom and Chassignet (2011); the TC center and domain were determined individually at each level. The domain radiuses for the geopotential height and temperature fields were 1.25 times the domain radius for the wind field, considering the larger influence of TC on these fields compared to the winds. However, the dynamic balance between variables was not considered in the removal process, either. In numerical simulations, this dynamic imbalance in the TC-removed fields is often overcome through dynamical initialization.

Galarneau and Davis (2013) proposed a new decomposition technique; they decomposed wind fields into TC and non-TC wind components to investigate TCs' steering flows [hereafter Galarneau and Davis filtering (GDF)]. The TC components of streamfunction (Ψ) and velocity potential (χ) were defined as:

$$\nabla^2\Psi = \begin{cases} \zeta, & (r \le r_0) \\ 0, & (r > r_0) \end{cases} \quad \text{and} \quad \nabla^2\chi = \begin{cases} \delta, & (r \le r_0) \\ 0, & (r > r_0)' \end{cases}$$

where ζ is the relative vorticity, δ is the divergence, ∇ is the two-dimensional gradient operator, and r and r_0 are the distance from the TC center and the radius of the TC domain, respectively. Using these Helmholtz equations, the TC-associated rotational and divergent wind components were then calculated by the obtained TC-related streamfunction and velocity potential, respectively. Unlike the KF that determines and retains the non-TC background circulation, the GDF removes all the rotational and divergent wind fields inside the pre-determined TC domain and does not decompose other variables such as geopotential and temperature. A similar vortex removal method is used for the vortex removal scheme in the Weather Research and Forecasting (WRF) model. In the scheme, using the nondivergent wind, the balance wind equation is solved to obtain geopotential, and then the temperature is computed in the vortex-removed field.

Here, the existing TC removal methods, the KF and GDF, are compared and summarized. In the KF, the TC domain is determined by using 850-hPa radial disturbance tangential wind profile from the TC center. In this procedure, 24 radial directions from the TC center are tested; the obtained removal domain is generally not circular. The TC center and domain remain fixed vertically at all levels. The wind, geopotential, and temperature associated with the target TC are then individually removed within the domain without considering the dynamic balance among the variables. In contrast, the GDF's TC-removal domains are circular: all vorticity and divergence are removed within the circular domain whose extent depends on the TC considered. Then, the rotational and the

divergent wind fields after the TC removal are recovered by solving the Helmholtz equation. The tunable parameters to detect the removal domains used in these methods are listed in Table 3.1. To obtain the TC removal domain, several tunable parameters [e.g., (a, b), $r_f(\theta)$, and $r_0(\theta)$] are used in the KF. By contrast, only one tunable parameter (r_0) is used in the GDF.

Table 3.1. Tunable parameters for determining the TC removal domain used in Kurihara et al. (1995) and Galarneau and Davis (2013).

Filtering method	Tunable parameter	Value used in the original study (reference in the original study)
KF	Search direction (θ) for wind profile test	24 radial directions (every 15° angle) (Section 2c)
	Parameters to determine the range of a starting point for wind profile test (a, b)	$a = 0.5, \mathrm{b} = 0.75$ (Appendix A)
	Condition to determine an appropriate starting radius for each direction [$r_f(\theta)$]	$v_{\tan} < 6$ m s^{-1} and $-\partial v_{\tan}/\partial r < 4 \times 10^{-6}$ s^{-1} (the second r for which this is true), or $v_{\tan} <$ 3 m s^{-1} [r: the distance from the TC center, $v_{\tan}(r, \theta)$: the tangential component of the disturbance wind centered on the TC center] (Section 2c)
	Maximum $r_f(\theta)$	1200 km (Section 2c)
	Definition of TC domain radius [$r_0(\theta)$]	$r_0(\theta) = 1.25\, r_f(\theta)$ (Section 2c)
GDF	TC domain radius (r_0)	depend on each TC (Section 2b and Figs. 10 and 11)

Because of the dynamic imbalance issue in the existing TC-removal schemes, in this section, a TC removal technique using the PV inversion (Davis and Emanuel 1991; Wang and Zhang 2003) is proposed. The proposed removal technique is applied to reanalysis data during June–October 2004. The derived fields are

dynamically balanced in the PVI framework. The TC-removed fields derived by the traditional and the proposed TC removal techniques are compared, and the TC contribution to intraseasonal variance and seasonal-mean circulation over the tropical WNP discussed in Hsu et al. (2008b) are reexamined with dynamically balanced TC-removed data.

Contents in this section are listed as follows: Section 3.2 describes the data and the procedure of the algorithm and Section 3.3 compares the TC-removed field with the existing and the proposed methods. The TC contributions to the intraseasonal variance of vorticity and the seasonal-mean geopotential height and temperature fields are discussed in Subsection 3.4.1. The potential effects of the negative PV anomalies associated with TCs for the TC removal are discussed in Subsection 3.4.2. Finally, this work is summarized in Section 3.5.

3.2. Data and methods

3.2.1. Data

The atmospheric variables used in this work were geopotential, horizontal and vertical winds, temperature, and specific humidity. The data were taken from the JRA-55, which is a 6-h 1.25° latitude/longitude gridded data set. This work analyzes 5 months of data during June–October 2004. An advantage of JRA-55 is that the data set assimilates tropical cyclone wind retrievals (TCRs) derived from best track data. Because of the TCRs, the intensity and center location of TCs are better represented in JRA-55 compared with other reanalysis data (Murakami 2014).

The PV inversion technique used in the following works was developed by Davis and Emanuel (1991). The domain used for PVI extends from 0° to 60°N and from 90°E to 150°W with a horizontal resolution of 1.25° latitude/longitude. The solution occasionally includes an unstable layer because of numerical error induced by an inhomogeneous vertical grid interval in the π coordinate. To prevent the appearance of the unstable layer in the solution, the data on the inhomogeneous vertical grid is reconstructed into a homogeneous one through cubic spline interpolation. The reconstructed data has 26 layers, the level at $k = 1\ (26)$ of the reconstructed data satisfies $\pi = C_p\ (0.5C_p)$, and the constant vertical grid interval is $\Delta\pi = 0.02C_p$.

The θ_v fields at the levels of $\pi = 0.99C_p$ and $0.51C_p$ (approximately 965 and 95 hPa) are used for the upper and bottom boundary conditions that satisfy $\theta_v = -\partial\Phi/\partial\pi = -f_0\partial\Psi/\partial\pi$, where f_0 is the Coriolis

parameter at 30°N. The Dirichlet boundary condition (fixed Φ and Ψ) is used for the lateral boundary condition. The Neumann boundary condition was attempted for solving the system; however, a stable solution is not always obtainable. Wu and Emanuel (1995) argued that the reason is probably the dynamic imbalance between mass and wind fields near the equator. To overcome this problem, they considered 10°N or 12.5°N as the southern boundary of the inversion domain. This study requires the inverted geopotential and streamfunction at low latitudes. Therefore, the Dirichlet boundary condition is selected to stabilize the solution.

The PVI is executed for 612 (every 6 hours for 5 months) cases in total. The solution diverges in some cases and tends to converge when a smaller under-relaxation parameter for Ψ (see Davis and Emanuel 1991) is applied; however, the use of the smaller parameter requires more computation time. To overcome this solution problem, the parameter becomes smaller automatically in the code when the solution diverges, and then the calculation is executed again. No smoothing for any variable is required in the PVI code because of the adoption of parameter correction and the application of the parameter ε introduced by Wang and Zhang (2003), which prevents the nonellipticity problem for the 3-D Poisson equation [see (1.5) and Wang and Zhang 2003].

To decompose the PV anomalies (PVAs) associated with TCs, the best track data provided by the Regional Specialized Meteorological Center, Tokyo (RSMC-Tokyo) are used. TCs in the categories of the tropical storm, severe tropical storm (STS), and typhoon (TY) during June–October 2004 in the RSMC-Tokyo best track data are defined as analysis objects in this work. The use of the RSMC-Tokyo best track data for the decomposition is discussed later.

3.2.2. Basic framework of PV decomposition

The PVAs generated by TCs are mainly characterized by the following two features: (1) the positive PVA concentrated on the TC center in the troposphere, and (2) the negative PVA widely spread over the TC in the upper troposphere and the lower stratosphere (Fig. 3.1). As discussed in Haynes and McIntyre (1987), the PV associated with a TC should follow the volume integral constraint of PV: the integral of PV in a certain volume bounded by two isentropic surfaces is constant. That is, a positive PV produced by diabatic heating must be compensated by an equal and negative PV in the volume. This constraint should be considered in principle when the TC-associated PVAs are isolated from the large-scale environmental PV. Whether such a constraint can be

obtained in real data is explored later in this section.

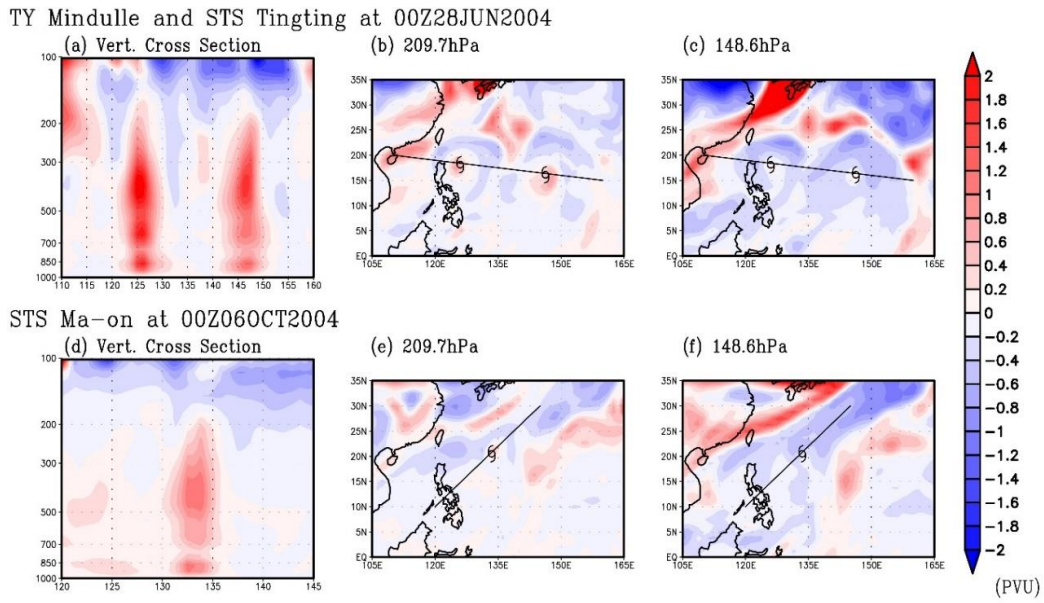

Fig. 3.1. (Top) Distributions of PV disturbance (in PVU). (a) Vertical cross-section along the line indicated in the following plan views; (b) plan view at 209.7 hPa; and (c) plan view at 148.6 hPa for the case of Typhoon Mindulle (at 18.1°N, 126.0°E, MSLP: 950 hPa) and Severe Tropical Storm Tingting (at 16.1°N, 146.3°E, MSLP: 980 hPa) at 0000 UTC 28 June 2004. (Bottom) As in the top panel but for the case of Severe Tropical Storm Ma-on (at 20.5°N, 133.5°E, MSLP: 985 hPa) at 0000 UTC 6 October 2004.

The characteristics of TC-associated positive PVAs are observed in the cases of TY Mindulle and STS Tingting (Fig. 3.1a) and STS Ma-on (Fig. 3.1d): these positive PVAs are spatially isolated and exist in the troposphere. In contrast, the distributions of the negative PVAs associated with the TCs are complicated. In the case of TY Mindulle and STS Tingting, a negative PVA encircles each positive PVA (Figs. 3.1a–c). These encircling negative PVAs are presumably associated with their respective TC. However, in the case of STS Ma-on, the distribution of negative PVA in the upper troposphere is highly asymmetric and spreads out in an area much larger than the TC itself; the negative PVA is associated with an elongated band (i.e., trough) to the north of STS Ma-on (Figs. 3.1d–f). Such asymmetric and ill-defined TC-related negative PVAs are observed in many TC cases. By contrast, a clear negative PVA encircling the center of TC such as in Figs. 3.1a–c is rarely observed. The horizontal distributions of the asymmetric negative PVAs observed in many TC cases are presumably associated with the large-scale wind fields in the upper troposphere. Greater asymmetry of the negative PVA in the upper troposphere tends to be observed when TCs move into the midlatitudes. Moreover, as shown in Figs. 3.1a,d, the negative PVAs over the TCs extend continuously from the upper troposphere to the lower stratosphere. The upper

boundaries of the negative PVAs associated with the TCs cannot be well defined.

In contrast to the partitioning of the positive PVA associated with the TC, it is more difficult to partition the asymmetric negative PVA into its TC and non-TC components. A clean way for separating TC and non-TC negative PVAs is yet to be identified. For this reason, an isolated positive PVA in the troposphere within the TC domain as proposed above and negative PVAs within the 800-km radius from the TC center, reported in the best-track data, from the surface to the top are identified.

Isolating the TC circulation would involve a definition of a mean (environmental) field, which depends on the purpose of the study. For example, Davis and Emanuel (1991) defined the mean as a 5-day time-averaged field in the extratropical cyclone study. Although Wu and Emanuel (1995) also employed time-averaging in their study of the TC movement, the averaging period was three months. The mean geopotential and streamfunction fields in these studies are solved in the system of （1.7） and （1.8). Conversely, spatially averaged fields were used for the mean fields in other studies. Focusing on a highly axisymmetric structure of TC, an axisymmetric averaged streamfunction circling the TC center is adopted as a mean streamfunction field, and mean geopotential and PV fields are solved by （1.7） and （1.8), respectively (Shapiro 1996; Wu et al. 2003, 2004). Wang and Zhang (2003) used the axisymmetric averaging for geopotential fields to avoid the appearance of negative static stability near the top of the planetary boundary layer; mean streamfunction and PV fields were then obtained from the gradient wind balance relation and （1.8), respectively. Although the time-averaged fields can be easily calculated, the shortcoming of time-averaging for TC study is that the obtained mean-field is severely influenced by the presence of TCs. By contrast, the advantage of using axisymmetric averaging is that the TC's axisymmetric structure can be completely removed when the TC center is clearly defined. However, TC sometimes tilts vertically, and thus, it becomes complicated to define the TC center. In this situation, the employment of axisymmetric averaging may cause errors in the mean and perturbation fields.

In this study, a new decomposition method in which both time and spatial averaging are applied is adopted to obtain the mean PV field, which is not related to the presence of TC. First, PV at a certain time is decomposed such that

$$q(t) = \overline{q(t)}^{t} + q'(t), \tag{3.1}$$

where $\overline{[\ ]}^t$ represents a 31-day time-averaging field,[1] called the basic field, and $q'(t)$ is the perturbation PV, which is the deviation from the basic PV field. Then, $q'(t)$ is separated into a TC and a non-TC component (the separating method is described in Subsection 3.2.3):

$$q'(t) = q_{\mathrm{TC}}(t) + q_{\mathrm{noTC}}(t).$$

Finally, the environmental PV field is obtained by combining the non-TC part with the basic PV field:

$$q_{\mathrm{E}}(t) = \overline{q(t)}^t + q_{\mathrm{noTC}}(t).$$

Equation (3.1) can be written as

$$q(t) = q_{\mathrm{TC}}(t) + q_{\mathrm{E}}(t).$$

This is the same as in Kurihara et al. (1995), except for the calculation of the basic field; in their study, the basic field was defined by a spatial filtering method. As stated above, $\overline{q(t)}^t$ includes the TC footprint. To cleanly remove the imprints of TC in the basic PV field, the basic PV field is further recalculated using the obtained $q_{\mathrm{E}}(t)$, and the TC and non-TC components are separated again from the new perturbation field, $q(t) - \overline{q_{\mathrm{E}}(t)}^t$:

$$q(t) = \overline{q_{\mathrm{E}}(t)}^t + q_{\mathrm{TC}}(t)|_{\mathrm{new}} + q_{\mathrm{noTC}}(t)|_{\mathrm{new}} \equiv q_{\mathrm{E}}(t)|_{\mathrm{new}} + q_{\mathrm{TC}}(t)|_{\mathrm{new}}.$$

The TC imprints in the new environmental PV field, $q_{\mathrm{E}}(t)|_{\mathrm{new}}$ are reduced than those in the previous environmental PV field $q_{\mathrm{E}}(t)$. However, the obtained new environmental PV field still has weaker TC imprints; therefore, this procedure is repeated. That is,

$$\begin{aligned}
q(t) &= \overline{q(t)}^t + q^1_{\mathrm{TC}}(t) + q^1_{\mathrm{noTC}}(t) \equiv q^1_{\mathrm{E}}(t) + q^1_{\mathrm{TC}}(t), \\
&= \overline{q^1_{\mathrm{E}}(t)}^t + q^2_{\mathrm{TC}}(t) + q^2_{\mathrm{noTC}}(t) \equiv q^2_{\mathrm{E}}(t) + q^2_{\mathrm{TC}}(t), \\
&= \overline{q^2_{\mathrm{E}}(t)}^t + q^3_{\mathrm{TC}}(t) + q^3_{\mathrm{noTC}}(t) \equiv q^3_{\mathrm{E}}(t) + q^3_{\mathrm{TC}}(t), \\
&\vdots \\
q(t) &= \overline{q^{n-1}_{\mathrm{E}}(t)}^t + q^n_{\mathrm{TC}}(t) + q^n_{\mathrm{noTC}}(t) \equiv q^n_{\mathrm{E}}(t) + q^n_{\mathrm{TC}}(t), \qquad (3.2)
\end{aligned}$$

where the superscript *n* denotes the number of iterations. The TC footprint in the environmental field disappears gradually with the iterations.

This decomposition procedure is summarized in Fig. 3.2 and the obtained basic (time-averaged) fields

[1] The application of different time mean periods has negligible impacts on the results.

after each iteration at 0000 UTC 16 August 2004 are shown in Fig. 3.3. After the first iteration, there exist two PV maxima, which are associated with the TCs, near 25°N, 125°E and 27°N, 133°E (Fig. 3.3a). The amplitudes of these maxima decrease after the second iteration (Fig. 3.3b). These PV extrema are virtually removed after the 4th and 5th iterations, and the distributions of $\overline{q_{\mathrm{E}}^{3}(t)}^{t}$ and $\overline{q_{\mathrm{E}}^{4}(t)}^{t}$ are almost identical (Figs. 3.3c,d). Thus, the TC imprints are effectively removed in $\overline{q_{\mathrm{E}}^{4}(t)}^{t}$ (the iteration is repeated five times for this study), and the usage of this time mean-field with little trace of the TC imprints is valid for this study. Another important feature of the basic field is that the PV value in a TC-free region is unchanged by the iterative method because of the definition of the environmental component of PV. Besides, note that the basic field varies with the time step because it is a 31-day running mean.

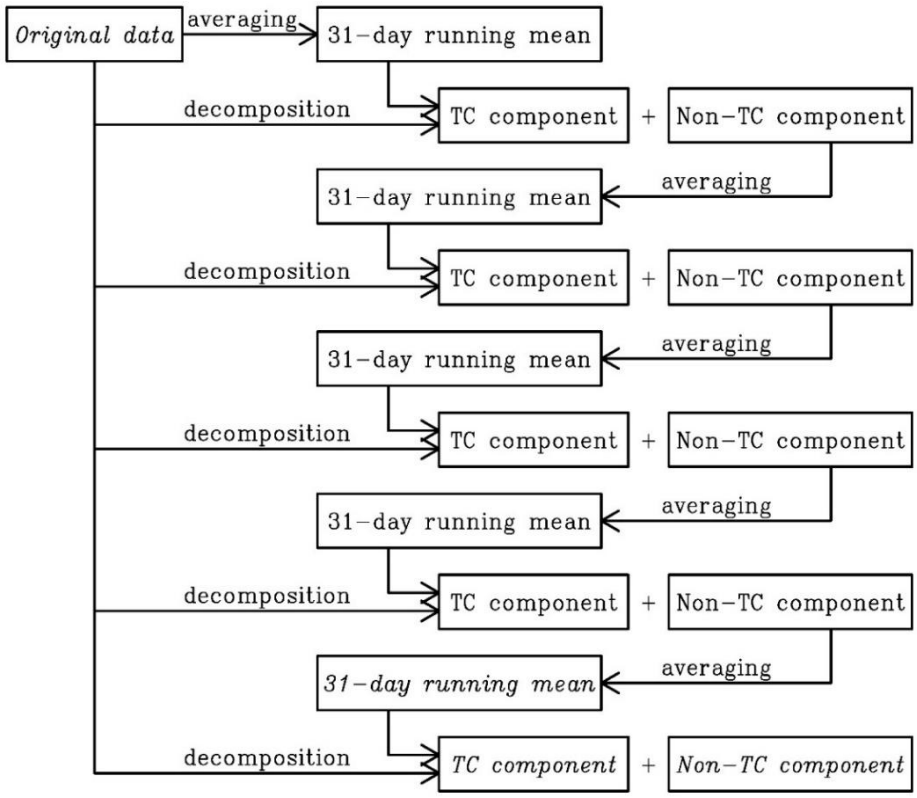

Fig. 3.2. Flowchart illustrating the procedure of creating the mean and TC component of PV fields (see the text). The fields in italic are used for the analysis.

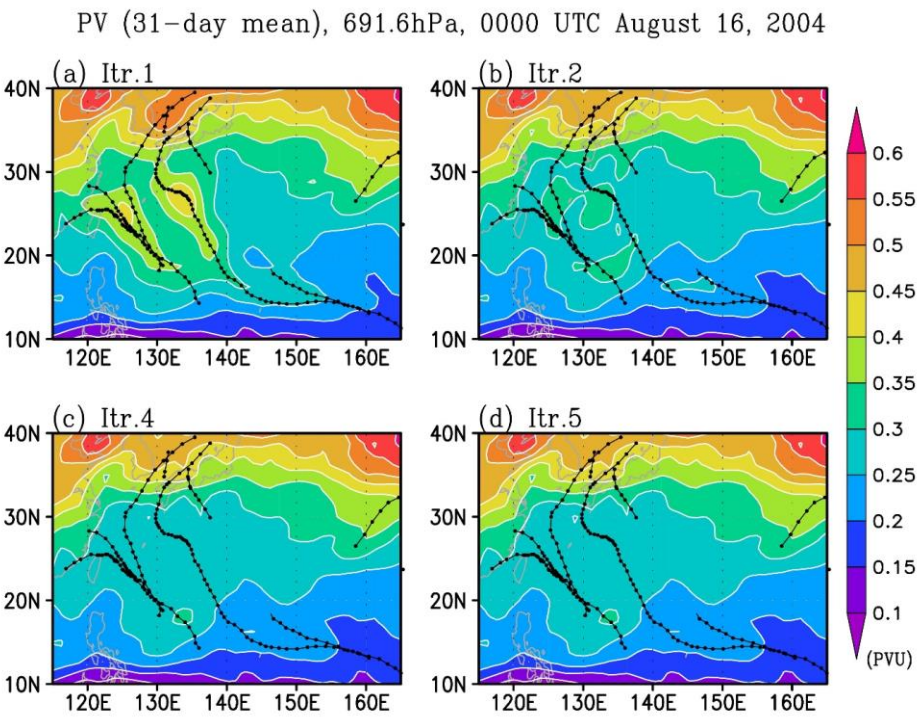

Fig. 3.3. Basic (31-day running mean) PV fields at 0000 UTC 16 August 2004 at 691.6 hPa after 1, 2, 4, and 5 iterations: (a) $\overline{q(t)}^t$; (b) $\overline{q_{\mathrm{E}}^1(t)}^t$; (c) $\overline{q_{\mathrm{E}}^3(t)}^t$; and (d) $\overline{q_{\mathrm{E}}^4(t)}^t$ (see the text). Dots indicate the locations of TCs that exist during the time-averaging period.

3.2.3. Determination of TC domain for PV decomposition

The basic procedure for the determination of TC domain for positive PVA in this work follows that proposed by Kurihara et al. (1995) and Kwon and Cheong (2010). The procedure is as follows: the TC center at each level and TC height are detected first, and then the domain boundary of the TC in 360 directions from the TC center is determined, as described in the next paragraph. After the TC domain detection, tropospheric positive PVA is extracted for separating the TC and non-TC components (see Subsection 3.2.2).

In Kurihara et al. (1995) and Kwon and Cheong (2010), the bilinearly interpolated disturbance field at 850 hPa was used to determine the TC center and domain. However, using one layer for defining the TC center (and domain) may lead to errors when the TC structure tilts in the vertical. Therefore, the TC center and domain individually at each layer are defined. Here, the TC center is defined as the location of maximum vorticity averaged within a 250-km disk. The precision of the TC center is (1.25/16)°; thus, the TC center is typically not located on a grid point. The TC position recorded in the RSMC-Tokyo best track data is used for an initial guess first, and then

the TC center at the level k = 2 is determined. PVAs associated with TCs at k = 1 do not need to be determined because the PPVI system does not require PVAs at the lowest level. It is the potential temperature anomaly that the PPVI system needs at the lowest level. The anomaly within 1200 km from the TC position recorded in the RSMC-Tokyo best track data is defined as the TC-associated potential temperature anomaly. After the determination of TC center at k = 2, a location of TC center at k = 3 is determined using the information of the center location at k = 2; this procedure is repeated continuously upward. However, this procedure may pick up another meteorological system that has strong vorticity in the vicinity of the TC. To avoid this potential problem, the vertically connected TC center, so-called the vortex axis, is examined; the TC center detection repeated upward is terminated when the vertical gradient of the vortex axis exceeds the threshold of $300/\Delta\pi$ [km J^{-1} kg K]. This threshold is empirically chosen and corresponds approximately to a two-grid distance per one layer at 1.25° horizontal resolution.

After determining the TC center, by examining the PV disturbance[2] profile along 360 radial directions, the extent of the TC domain is determined at all layers. Going outward from a point 200 km away from the obtained TC center, each profile is tested at radial intervals of 10 km. It means that the profile from 0 to 200 km is not tested. The reason will be discussed later in this paragraph. The domain boundary at each angle is defined as the point where q_{test} <0.05 PVU (PV unit: 10^{-6} m^2 kg^{-1} s^{-1} K) is first satisfied, where q_{test} is the PV disturbance along the radial direction. In general, distribution of PV disturbance associated with TC at a specified level does not necessarily have a closed curve of the value with 0 PVU that encloses the TC center (see red contours in Fig. 3.4 described later); therefore, the condition $q_{\mathrm{test}} <$ 0.05 PVU is sought. Then, the distance of the domain boundary from the TC center is modified to consider the range of $0 \leq q_{\mathrm{test}} \leq$ 0.05 PVU; assuming that the distance of the range of $0 \leq q_{\mathrm{test}} \leq$ 0.05 PVU is 100 km, 100 km is added to the domain boundary distance. Moreover, the innermost point where the gradient of q_{test} exceeds 0 PVU m^{-1} is also regarded as the boundary of the TC domain because q_{test} typically decreases outward. The reason why the starting point for seeking the radial profile is not the TC center but 200 km away from the TC center is that the previously defined TC center is not always located at the position of the maximum q_{test}, and thus, the gradient of q_{test} becomes positive within a range of 0 to 200 km in some cases. The distance is bounded by 1200 km, thus the range of the distance is restricted to 200 to 1200 km. In most cases, the domain boundary exhibits a smoothed curve, but a spike-like curve occasionally

[2] The PV disturbance is equivalent to $q(t) - \overline{q(t)}^t, q(t) - \overline{q_{\mathrm{E}}^1(t)}^t, q(t) - \overline{q_{\mathrm{E}}^2(t)}^t, \cdots, q(t) - \overline{q_{\mathrm{E}}^{n-1}(t)}^t$ in (5.9). Note that the PV disturbance varies with the iteration step.

appears. The spike-like curve is replaced with the smoothed curve, which is calculated using the adjacent boundary points. The examples of the obtained TC domains are illustrated in Fig. 3.4. Although the TC domain for a strong storm is almost circular (Fig. 3.4c), the TC domains for weaker storms can be stretched in a certain direction (Figs. 3.4a,b). Visually, the TC domains can be reasonably detected by this method according to the 0 PVU line shown in Fig. 3.4.

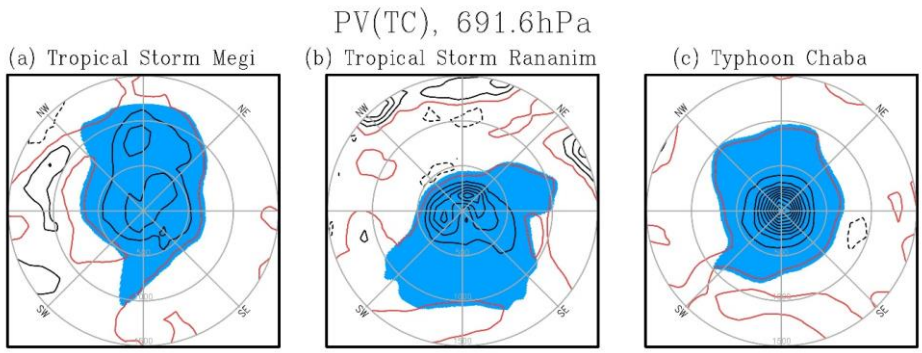

Fig. 3.4. Distributions of the PV disturbance at 691.6 hPa: (a) Tropical Storm Megi at 1200 UTC 16 (MSLP: 992 hPa); (b) Tropical Storm Rananim at 1800 UTC 12 (MSLP: 975 hPa); and (c) Typhoon Chaba at 0000 UTC 24 (MSLP: 910 hPa) August 2004. The contour interval is 0.2 PVU (red contours indicate 0 PVU). The blue-colored area represents the TC domain for positive PVA, and the three gray-colored circles indicate distances of 500, 1000, and 1500 km from the TC center.

In some cases, TC couples with other meteorological systems originated in the stratosphere. To prevent picking up the coupled PVAs, the PVA associated with TC in the troposphere is restricted (i.e., the PVA in the stratosphere is not defined as the anomaly associated with TC). In this work, the dynamical tropopause is defined as the surface of 2 PVU; the height of the dynamical tropopause is searched downward from the top of the gridded PV data.

As stated above, both positive and negative PVAs were considered as the PVA associated with TC. An 800-km disk from the TC center reported in the best-track data from the surface to the top was assumed as the negative PVA domain in this work. This definition is less sophisticated compared with one of the positive PVA. This is because of the highly asymmetric distribution of the negative PVA associated with TCs in most cases. The respective effect of positive and negative PVAs associated with TCs on the surrounding large-scale circulations will be discussed later.

3.2.4. Estimations of vertical velocity and irrotational wind

The TC-associated anomalies of nondivergent wind, geopotential, and temperature are obtained from the PPVI, and by subtracting these from the respective total fields the TC-removed components are obtained. The TC-removed components of vertical velocity and irrotational wind are calculated based on the quasi-balanced omega equation and continuity equation as in Wang and Zhang (2003) (hereafter the balanced omega equation system). In this procedure, diabatic heating and specific humidity, which are given explicitly during the calculation, are modified in the same manner as the KF. The Lagrangian derivative of potential temperature is used for the diabatic heating calculation, which is computed from the JRA-55 using centered 6-h air parcel trajectories, that is, 3-h forward and backward trajectories. Five-minute intervals of linear temporal interpolation are considered for the trajectory calculation. Similarly, the TC-included components of the vertical velocity and the irrotational wind are obtained from the balanced omega equation system, but in this instance, the diabatic heating and specific humidity obtained from the JRA-55 is directly used without any modifications. Finally, after subtracting the TC-removed components from the TC-included components, the TC-associated vertical velocity and irrotational wind are obtained.

3.3. Comparison of the effectiveness of PVI and the existing TC removal schemes

The fields in which TCs were removed by the KF at 0000 UTC 23 August 2004 are shown in Fig. 3.5. There exist two typhoons: TYs Chaba centered at 15.2°N, 143.6°E and Aere centered at 22.9°N, 126.2°E. The TCs are removed within a polygonal domain at the lower layer (Fig. 3.5i), but weak cyclonic circulations still exist in the TC-removed field at the location where the TCs originally existed (Figs. 3.5g,h). Similarly, in the middle layer, the weak cyclonic circulations in the TC-removed field remain (Figs. 3.5d,e). The isolated TY Aere is not encircled by the zero-line of geopotential height deviation (Fig. 3.5f), indicating that the size of the TC domain at this layer is not sufficient to remove the TC component. TY Aere is elongated southwestwardly (Fig. 3.5d); therefore, a wider domain is required for the removal. The TC domain determined by the KF is too small because the center and domain are determined at only 850 hPa. Besides, the temperature fields at the upper layer are shown in Figs. 3.5a–c. The warm cores induced by two typhoons seem to be fairly removed in the field. However, similar to the mass and wind fields at the lower and middle layers, the high temperature remains beyond the TC domain in the TC-removed field (Figs. 3.5a,b).

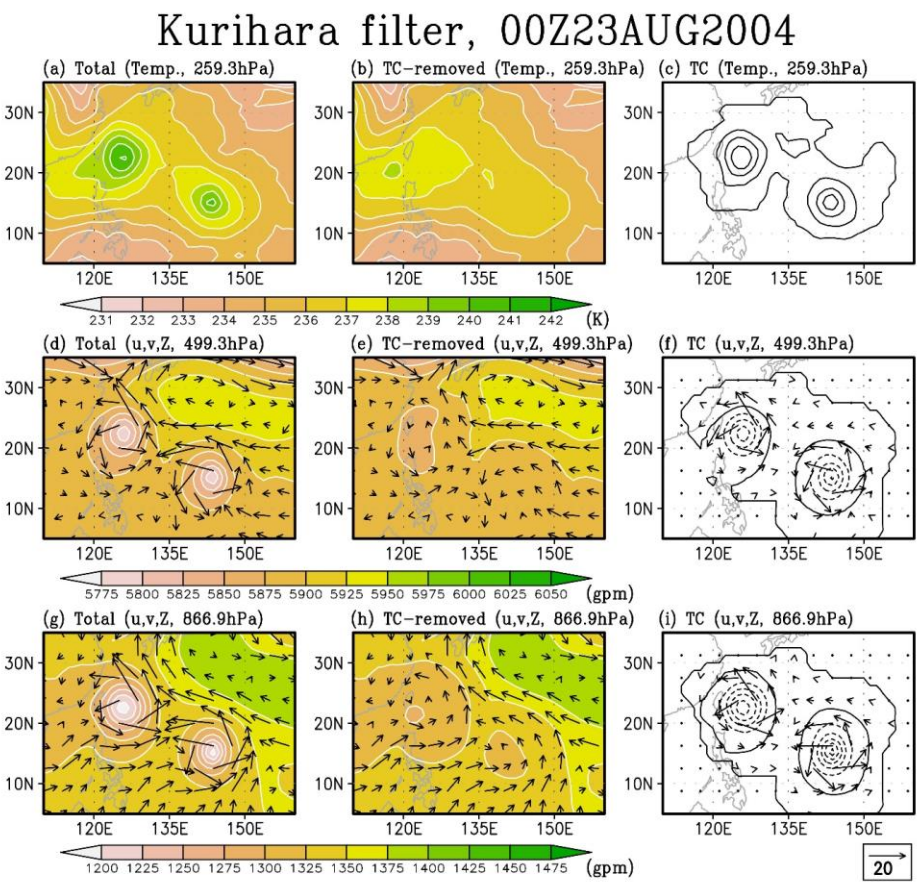

Fig. 3.5. (Top) Temperature distribution at 259.3 hPa at 0000 UTC 23 August 2004: (a) JRA-55 reanalysis; (b) field in which TC-component is removed; and (c) TC-component. The TC-component is determined based on the KF method. (Middle) As in the top panel but for geopotential height (color and contour) and horizontal wind (vector) fields at 499.3 hPa. (Bottom) As in the middle panel but at 866.9 hPa. The contour interval in the top panel (middle and bottom panels) is 1 K (25 gpm). A vector scale in units of $\mathrm{m\,s^{-1}}$ is shown in the lower right-hand corner.

The TC-removed fields calculated by the PVI are shown in Fig. 3.6. Compared with the results by the KF, the TC components of wind and mass fields spread over a wider area and have larger amplitudes (Figs. 3.5f,i and 3.6f,i). The TC-removed fields are different from that by the KF, and no residual cyclonic circulations at the TC-existed location are found in the TC-removed field (Figs. 3.5e,h and 3.6e,h). Whereas the geopotential and wind fields outside the TC domain remain largely unchanged in the results by the KF, the outside field exhibits marked changes after the TC removal by the PVI. While the TC-removed fields obtained by the PVI are dynamically balanced in the PVI framework, it is unclear whether the TC-removed fields obtained by the KF are dynamically balanced. Similarly, the warm cores associated with the two typhoons obtained from the PVI are larger than those obtained from the KF (Figs. 3.5c and 3.6c); therefore, the high temperature beyond the TC-existed

domain shown in the result by the KF no longer remains in the PVI result (Figs. 3.5b and 3.6b). Note that the maximum temperature at 12°N, 148°E in the TC-removed field (Fig. 3.6b) is associated with another meteorological system, a PV maximum to the southeast of TY Chaba.

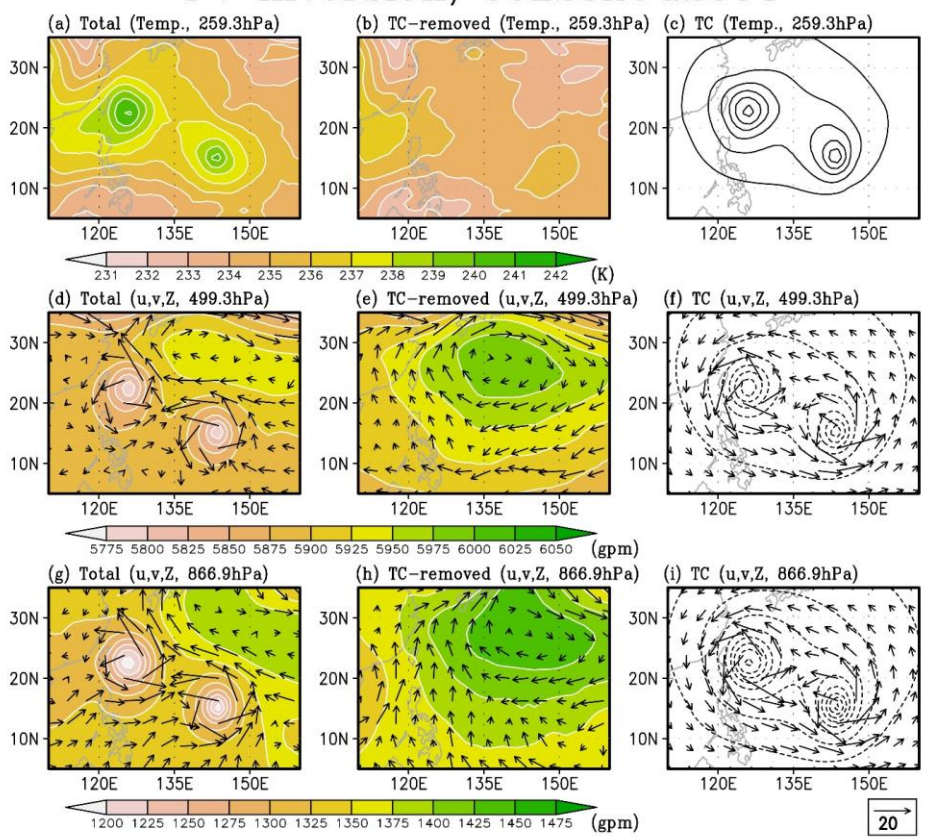

Fig. 3.6. As in Fig. 3.5, but for the results obtained by the PVI.

Figure 3.7 shows the relative vorticity of the original and TC-removed fields at a low level. Because of the detection of the larger TC-component wind field by the PVI, the relative vorticity of the TC component becomes (approximately 50%) larger than that obtained by the KF (Figs. 3.7e,g). Residual amplitudes of relative vorticity remain at the TC-existed location in the KF result (Fig. 3.7b). This is because, as shown in Fig. 4 of Kurihara et al. (1995), a weaker cyclonic circulation tends to remain around the TC location when the KF is applied. By contrast, such weak anomalies are not found in the TC-removed field by the PVI (Fig. 3.7d). Moreover, in the TC-component vorticity by the KF, thick bands of negative vorticity surrounding the positive vorticities centered on the TC centers appear, but such kind of vorticity structure is not seen in the PVI result (Figs. 3.7e,g). This tendency of the KF TC detection method in producing thick negative vorticity bands in the surroundings of a TC does not seem realistic. Besides, similar to the TC-removed wind field surrounding the TCs obtained by the KF

(Figs. 3.5g,h), the TC-removed vorticity field surrounding TCs remains largely unchanged (Figs. 3.7a,b). While the environmental wind field surrounding TCs changes more significantly after the TC removal by the PVI, the surrounding vorticity field is nearly unchanged as in the KF approach, indicating that the choice of TC removal technique (the KF or PVI) has a minimum influence on the vorticity in the exterior of the TC region. However, the result obtained from the GDF shows a larger TC footprint on the relative vorticity field compared with that by the PVI (Figs. 3.7c,f). This is caused by the TC removal procedure in the GDF: the vorticity within the defined TC domain is completely removed regardless of the signs (Fig. 3.7c), thus creating a discontinuity at the boundaries.

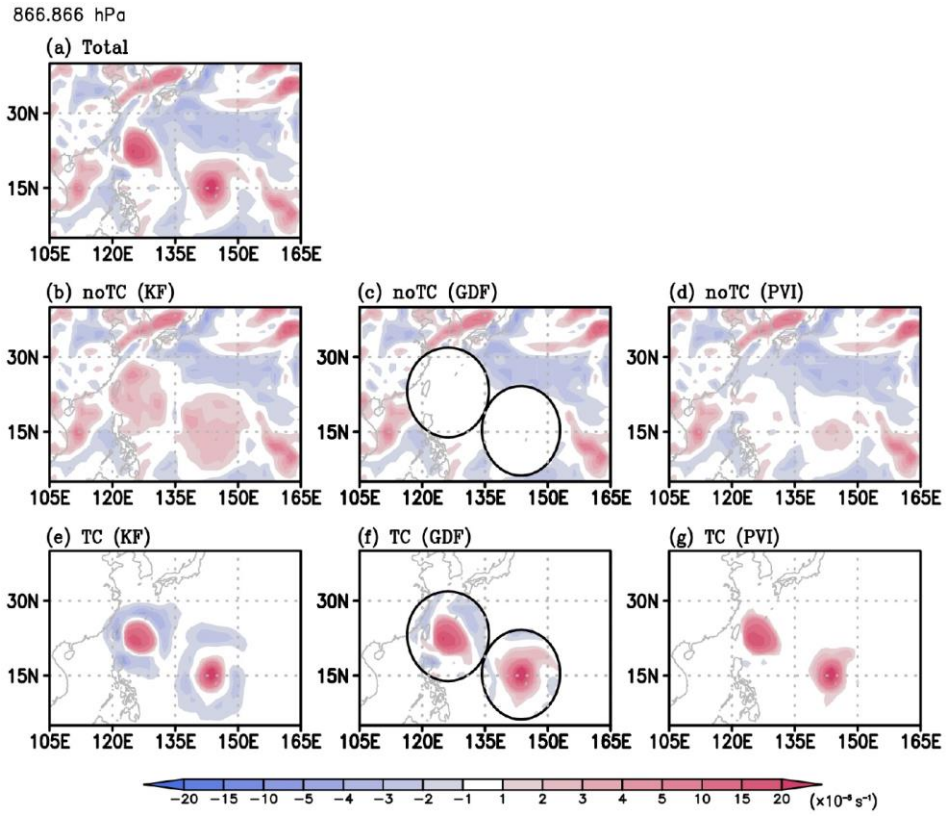

Fig. 3.7. Relative vorticity (color and contour) at 866.9 hPa at 0000 UTC 23 August 2004: (a) JRA-55 reanalysis; (b–d) field in which TC-component is removed; and (e–g) TC-component. The fields are decomposed by (b,e) KF, (c,f) GDF, and (d,g) PVI. The circles shown in (c,f) indicate the boundaries of TC removal regions.

To confirm the dynamic consistency of the KF's TC-removed fields, further PVI calculations to their PVAs are performed; the results are shown in Figs. 3.8, 3.9, and 3.10. In this calculation, the TC-associated PVA is defined as the difference between the total and TC-removed PV fields obtained by the KF (hereafter KF-PVI). The derived TC component is smaller and weaker than the TC component derived from the PVI alone (Figs. 3.6c,f,i and 3.8c,f,i), but the TC components obtained by the KF-PVI alone and those obtained by the KF are similar (Figs.

3.5c,f,i and 3.8c,f,i). Moreover, as also clearly seen in a vertical cross-section, even though the TC components of mass and wind fields obtained by the KF and KF-PVI are distributed locally (Figs. 3.9d,f,g,i), the components obtained by PVI are distributed over a wider range (Figs. 3.9e,h). The TC-removed fields and TC component derived from the KF-PVI approach are consistent with the results derived from the KF approach alone, however, the distributions are different from those obtained by the PVI.

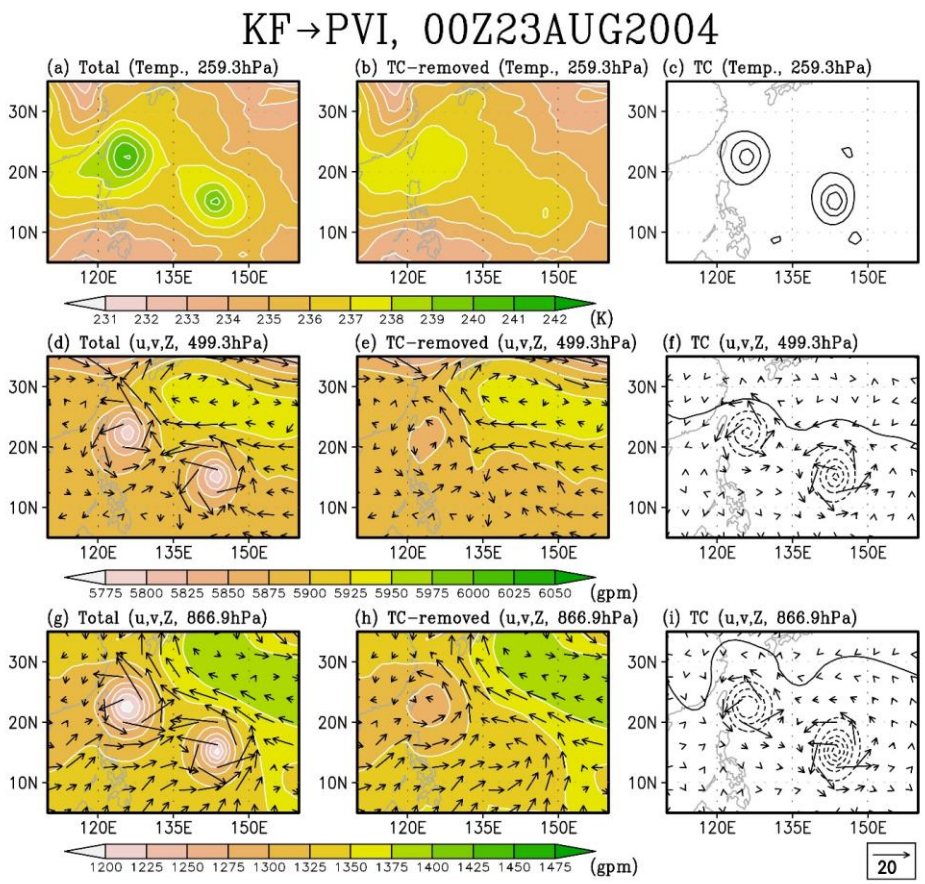

Fig. 3.8. (Left-hand and center columns) As in the center and the right-hand columns of Fig. 3.5 but the input PVA is calculated using the TC-removed fields obtained by the KF, respectively. (Right-hand column) The difference in the TC component (center column) and the TC component obtained by the KF (the right-hand column of Fig. 3.5). Contour intervals in panel (c) and (f,i) are 0.25 K and 25 gpm, respectively. A vector scale in units of $\mathrm{m\,s^{-1}}$ is shown in the lower right-hand corner.

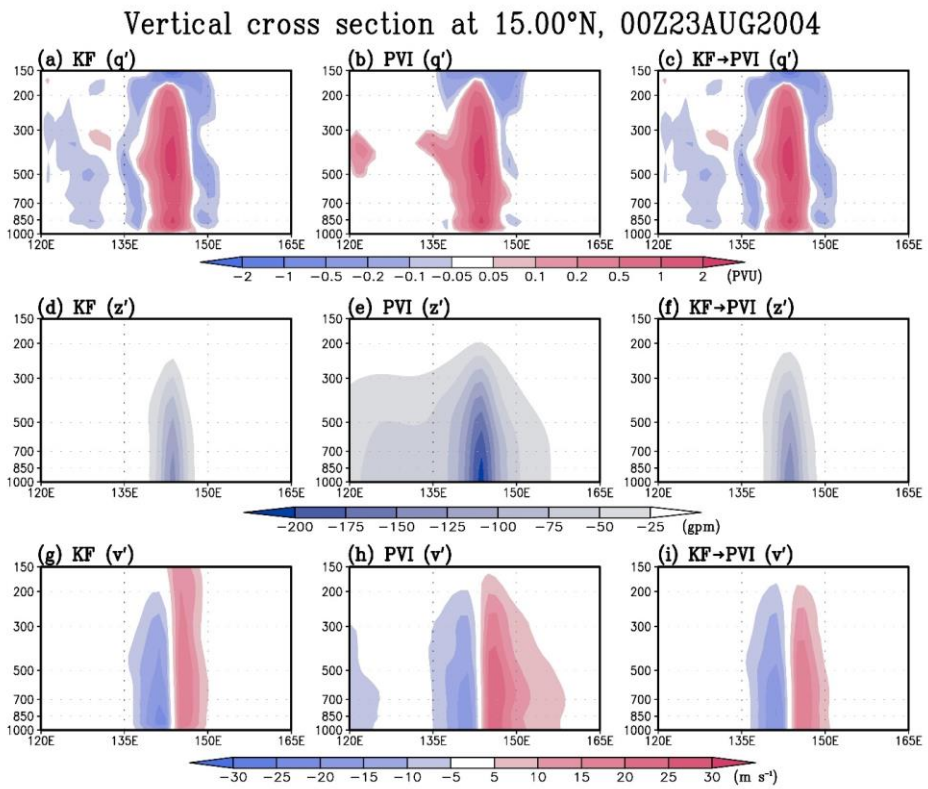

Fig. 3.9. The vertical cross-section at 15°N at 0000 UTC 23 August 2004 of TC-associated (top) PVA, (middle) geopotential height deviation, and (bottom) meridional wind deviation. The left-hand (center) column is derived from the result obtained by the KF (PVI) [corresponding to Figs. 3.5c,f,i (Figs. 3.6c,f,i)]. The right-hand column is the result by the PVI but the input PVAs are calculated using the KF's TC-removed fields (corresponding to Figs. 3.8b,e,h).

In principle, the PVI would generate wider-spread geopotential and temperature fields. However, the KF-PVI generates more localized fields than the PVI does (Fig. 3.9). This seeming inconsistency is attributed to the cancellation of fields inverted from positive and negative PVAs. To investigate the cancellation, the respective effects of positive and negative PVA in the KF-PVI are shown in Fig. 3.10. As the same as the vorticity structure shown in Fig. 3.7e, the TC-associated PVA in the KF has a thick negative PVA surrounding the positive PVA centered on the TC (Fig. 3.10a). The thick negative PVA is mainly generated by the thick negative vorticity, which is artificially generated by the KF scheme instead of realistic TC characteristics. The positive PVA induces widely spread TC components of mass and wind fields, which is like the PVI result (Figs. 3.10e,h). Similarly, the negative PVA induces widely spread anticyclonic circulation (Figs. 3.10f,i). The anticyclonic circulation cancels out the widely spread cyclonic circulation induced by the positive PVA. As a result, the TC components of mass and wind fields are distributed locally.

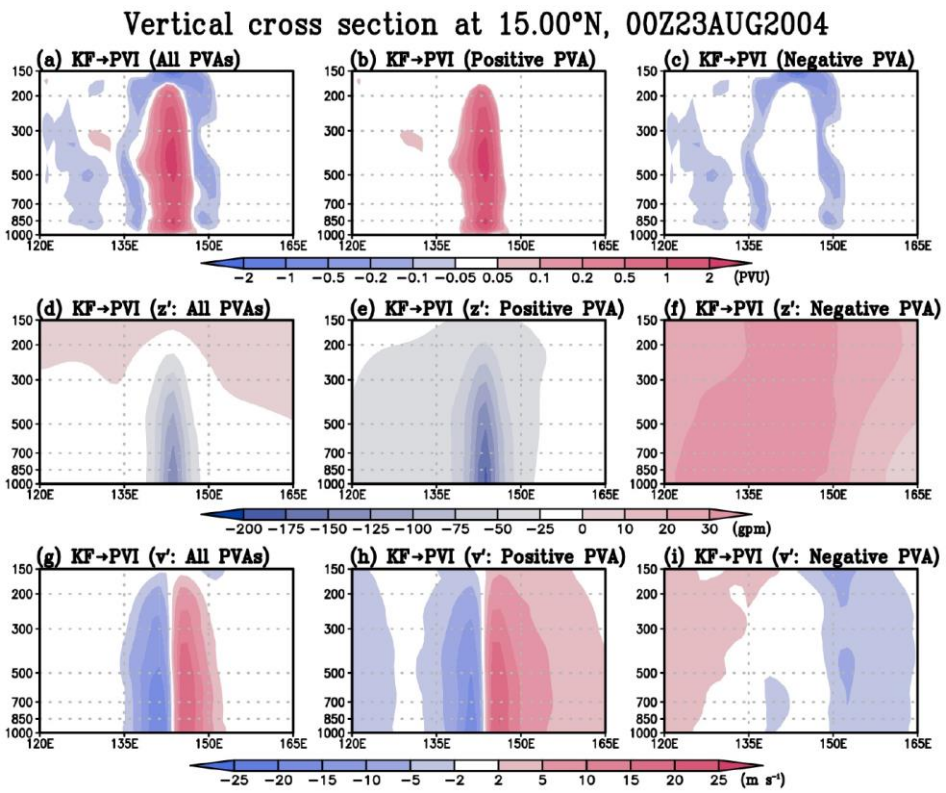

Fig. 3.10. (Left-hand column) As in Figs. 3.9c,f,i, respectively, with different color ranges. (Center column) As in the left-hand column, but the results are induced by positive PVA. (Right-hand column) As in the left-hand column, but the results are induced by negative PVA.

The PVI approach can be used to derive the mass and temperature associated with the TC-removed vorticity obtained from the GDF. Figure 3.11 shows the result of PVI calculation, in which the PVAs are calculated using the TC-removed fields obtained by the GDF [here, to compute PV in the TC-removed field, the temperature in the TC-removed field is obtained by the spatial filtering used in Kurihara et al. (1995)]. The derived TC components are slightly smaller but qualitatively similar to the result derived by the PVI (Figs. 3.9e,h and 3.11b,c). This indicates that the GDF fairly calculates TC-associated PVA and confirms again that the mass and temperature fields associated with TC vorticity exhibit a wider spread structure than the vortex itself. However, a direct application of this removal technique needs to be cautioned because the TC component of relative vorticity decomposed by the GDF includes background relative vorticity (Fig. 3.7c).

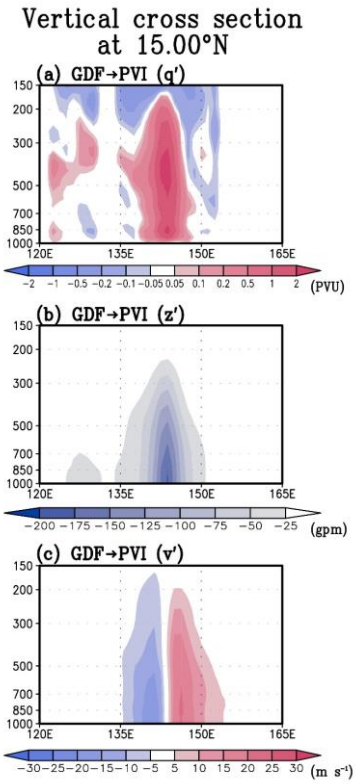

Fig. 3.11. As in the right-hand column of Fig. 3.9, but the input PVAs are calculated using the GDF's TC-removed fields.

3.4. Results

3.4.1. TC contributions to intraseasonal variability and seasonal-mean fields in the typhoon season in 2004

The technique proposed here is potentially useful for quantifying the contribution of TCs to climate variability. Two examples, namely seasonal-mean field and intraseasonal oscillation during June–October 2004, are demonstrated here. Figure 3.12 shows the seasonal-mean relative vorticity of the original and TC-removed fields during June–October 2004. In the following analysis, the above-mentioned negative vorticity of the TC component analyzed in the KF will be ignored because the negative vorticity seems to be artificially generated. Due to the prevailing recurving TC tracks in June–October 2004, the total removed PV associated with TCs exhibits a bow shape with the maximum located near TCs' statistical recurvature point where the TCs usually slow down (Figs. 3.12e–g). Removal of TC PV results in larger negative vorticity in the north and smaller positive vorticity in the

south. Moreover, consistent with the 6-h vorticity fields shown in Fig. 3.7, the TC component of seasonal-mean vorticity obtained by the PVI is approximately 40% larger than that derived from the KF (Figs. 3.12e,g). Because of the larger vorticity of the TC component derived from the PVI, the positive vorticity over the central Philippine Sea becomes smaller, and the negative vorticity in the northeastern of the recurving point becomes larger than by the KF (Figs. 3.12b,d). In contrast, the TC component of seasonal-mean vorticity obtained by the GDF is approximately 20% larger near the statistical recurvature point than that derived from the PVI (Figs. 3.12f,g). This results in the larger negative vorticity in the northeastern of the recurving point than those based on the PVI (Figs. 3.12c,d). The GDF's larger TC contribution to the seasonal-mean vorticity is likely caused by the removal of not only the TC component of the relative vorticity within the removal domain but also its background field in the scheme.

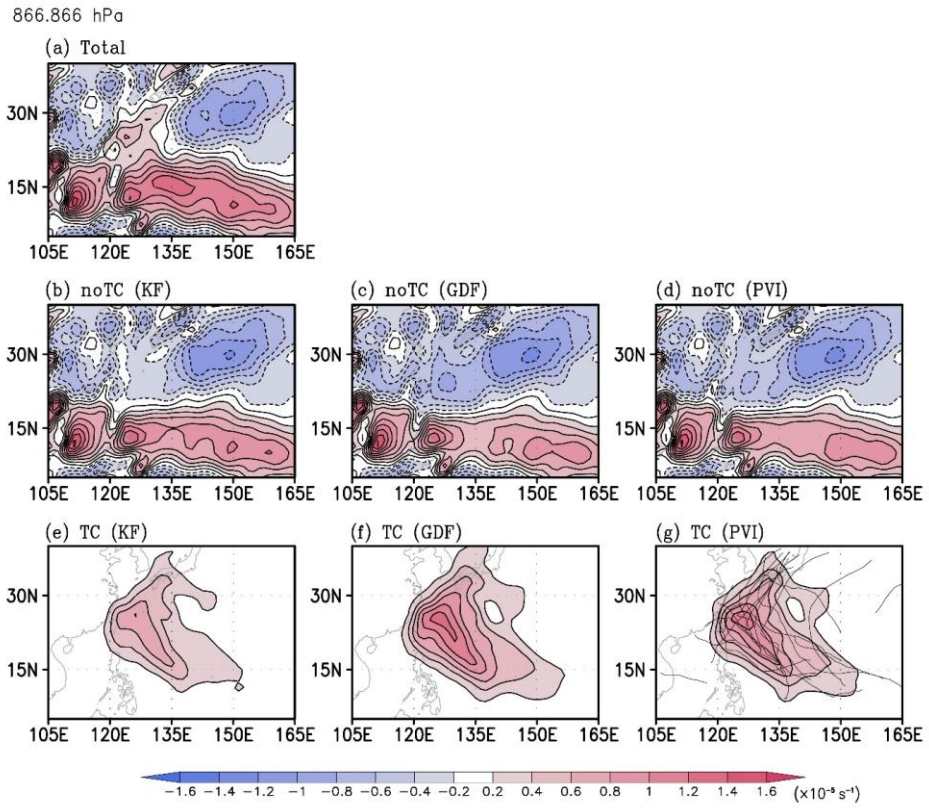

Fig. 3.12. As in Fig. 3.7, but for the time mean in June–October 2004. Contour interval is $0.2 \times 10^{-5}\ s^{-1}$. The TC tracks during June–October 2004 are also shown in (g).

Figures 3.13a–c show the seasonal-mean upper-level temperature of the original and TC-removed fields. After the removal of TCs, the seasonal-mean upper-level temperature becomes lower in both the KF and PVI results. The largest temperature decrease exists to the east of Taiwan (approximately 25°N, 128°E). Because the

larger warm core is calculated in the PVI than in the KF, a temperature decrease in the upper-level temperature after removal of TCs by the PVI is larger than that by the KF; the temperature decreases in the KF and PVI is 0.35 and 1.35 K, respectively, at the largest temperature decrease location. The seasonal-mean low-level geopotential height of the original and TC-removed fields are shown in Figs. 3.13d–f. While a weak seasonal-mean cyclone remains to the east of the Philippines becomes smaller after TC removal by the KF, the seasonal-mean cyclone disappears in the PVI result. The extent of low-level negative vorticity in the northeastern of the recurvature point obtained from the GDF and PVI (Figs. 3.12c,d) indicates that the subtropical anticyclone expands its spatial coverage westward and becomes more dominant over the subtropical WNP after the TC removal. As would be expected from the 6-h TC-removed geopotential height fields (Figs. 3.6e,h), the seasonal-mean TC-removed geopotential height field shows the westward expansion and intensification of an anticyclone over the region (Figs. 3.13d,f). The above results reveal that the existence of TCs with their strong positive vorticity enhances the strength of the monsoon trough and weakens the subtropical anticyclone in the lower troposphere, and at the same time warms the troposphere. In other words, the strength of seasonal-mean circulations over the tropical WNP is markedly enhanced because of the presence of TCs, which are induced in the favorable background conditions provided by the large-scale circulations. This result demonstrates the mutual dependence of TCs and background mean-circulations through active interaction.

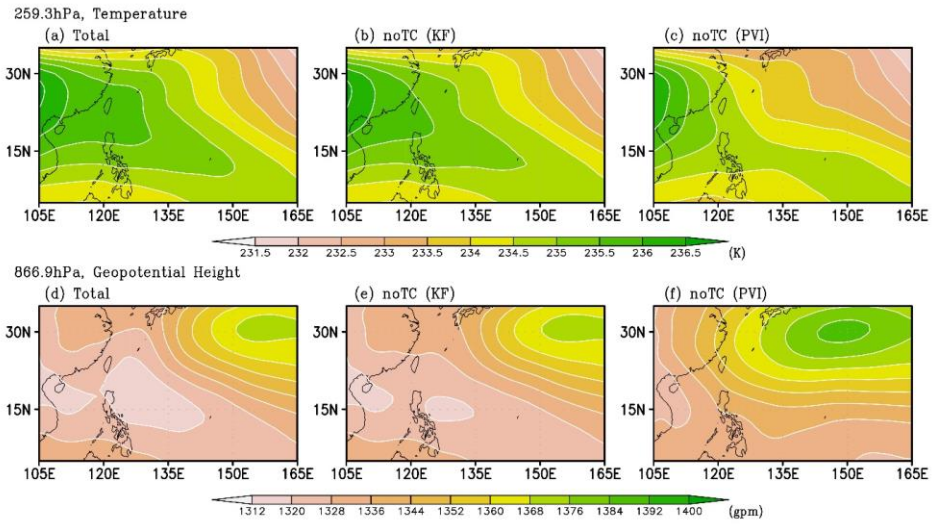

Fig. 3.13. Temperature (color and contour, in K) at 259.3 hPa for the time mean in June–October 2004: (a) JRA-55 reanalysis; TC-removed field obtained by (b) KF and (c) PVI. (d–f) As in (a–c), respectively, but for geopotential height at 866.9 hPa (in gpm).

Hsu et al. (2008b) revealed that the 32–76-day ISO was the dominant subseasonal fluctuation in June–October 2004, and its amplitude reached the 50-year record high value. The contributions of TCs to the 32–76-day ISV at the lower layer were estimated for both TC-removed fields, as shown in Fig. 8 by Hsu et al. (2008b), and the difference between these contributions was also investigated. The contributions of 32–76-day variance of the low-level vorticity indicate two major ISV regions along the TC tracks: one is located to the east of Taiwan and the northern Philippines, and the other to the south of Japan (Fig. 3.14e). The former corresponds to the northwestward TC tracks, while the latter corresponds to the northeastward TC tracks after recurvature. As compared with Fig. 8 by Hsu et al. (2008b), the variance associated with the East Asian monsoon trough over the SCS is much larger than the variance associated with the clustered TCs (Fig. 3.14a). This is because of the differences in the resolution (1.25° versus 2.5°) and temporal interval (6 hourly versus daily) of the data used in the analysis, as discussed in Section 5 of Hsu et al. (2008a). The TC contribution obtained by the GDF is consistent with the KF's but in a much larger magnitude (Fig. 3.14f). The stronger TC vorticity derived from the GDF presumably leads to the larger TC contribution to the subseasonal variance. The difference between the contributions calculated by the KF and PVI appears in the northwestward-track region: the TC contribution calculated by the PVI in the northwestward-tracks region is larger (up to 20%) than the contribution calculated by the KF (Fig. 3.14g). By contrast, the differences in the TC contribution are relatively small in the northeastward-track region. The variance reduced significantly in these two regions after removing the TCs (Figs. 3.14a–d). Similar to the result in Hsu et al. (2008b), the clustered TCs contribute 50% or more to ISV along the TC tracks in both TC removal procedures, and this contribution is larger when the PVI is applied.

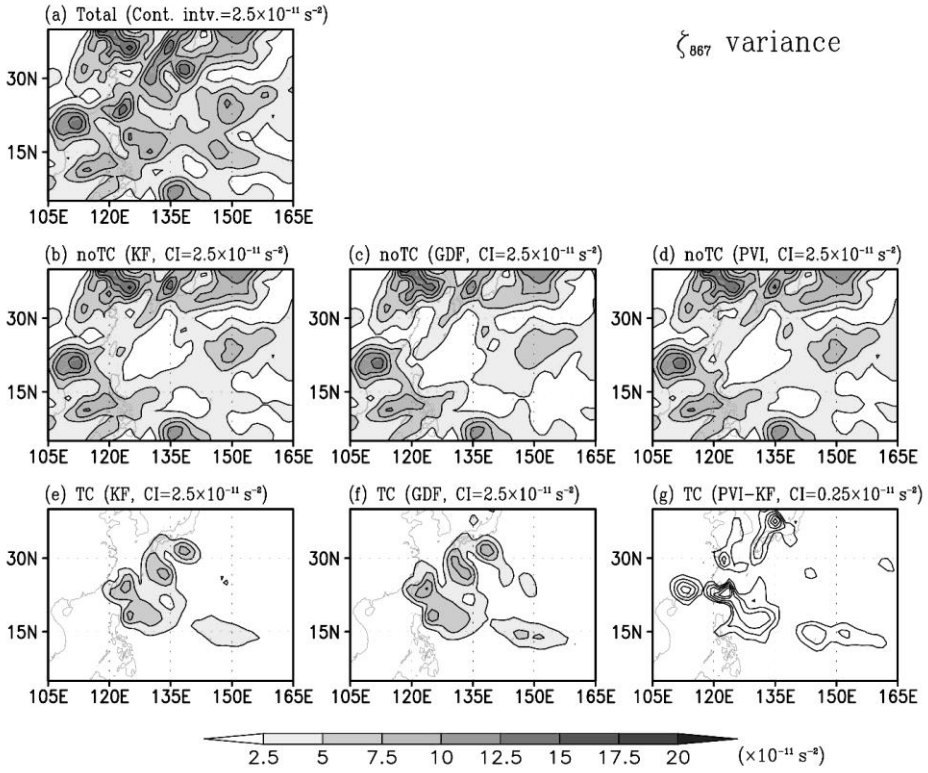

Fig. 3.14. Intraseasonal (32–76-day) variance of relative vorticity (shade and contour) at 866.9 hPa. (a) JRA-55 reanalysis. (b–d) TC removed field determined by the KF, GDF, and PVI, respectively. The difference between (a) and (b,c) are shown in (e,f), respectively (referred to as the TC component of intraseasonal variance). (g) The difference in the TC component of intraseasonal variance between the PVI and KF. Non-positive contour is omitted in the bottom panel. Contour interval is $2.5\ (0.25) \times 10^{-11}\ \mathrm{s}^{-2}$ in a–f (g).

To investigate the ISO propagation after the removal of TCs, the Hovmöller diagrams of low-level vorticity are shown in Fig. 3.15. The ISO propagates northward associated with the northward movement of TCs; therefore, the Hovmöller diagram of low-level vorticity averaged over 120°E–150°E is first shown in Fig. 3.15a. The large amplitudes are observed near 8°N and 17°N, and northward propagation from 5°N to 20°N is also evident. The intraseasonal perturbation repeatedly oscillated throughout June–October 2004. After the TC removal, the large amplitudes of the vorticity weaken significantly between 10°N and 25°N (Figs. 3.15b–d). Spectral analysis reveals that removing the TCs reduces the intraseasonal amplitude by 50% (not shown). The northward propagation becomes much weaker and less systematic after the TC removal. More interestingly, a slow southward propagation from 30°N to 10°N, which is not present before the TC removal, becomes evident. Thus, the TCs leave marked footprints in the propagation characteristics of the ISO, i.e., the amplitude and propagation tendency of large-scale intraseasonal perturbation. These changes in the ISO characteristics can be seen in all three TC removal

methods; however, the PVI method yields larger differences.

Next, because ISO is mainly affected by the northwestward TC tracks in the 10°N–20°N latitudinal band, to investigate longitudinal propagation, the Hovmöller diagram of low-level vorticity averaged over 10°N–20°N is shown in Fig. 3.15e. The eastward propagation of the low-level vorticity from 120°E to 160°E is observed from the middle of July 2004. Intraseasonal oscillations are also evident near 120°E, 130°E, and 145°E. After the TC removal, the amplitudes of the vorticity and oscillations weaken, especially between 120°E and 160°E, where TCs originally existed (Figs. 3.15f–h). As with the northward propagation, the eastward propagation becomes less evident after the TC removal. Although the choice of the TC removal method influences the vorticity amplitude, the effect is weaker than that in the northward component. Overall, the TC footprint in the ISO propagation exhibits the larger amplitude and more organized propagation.

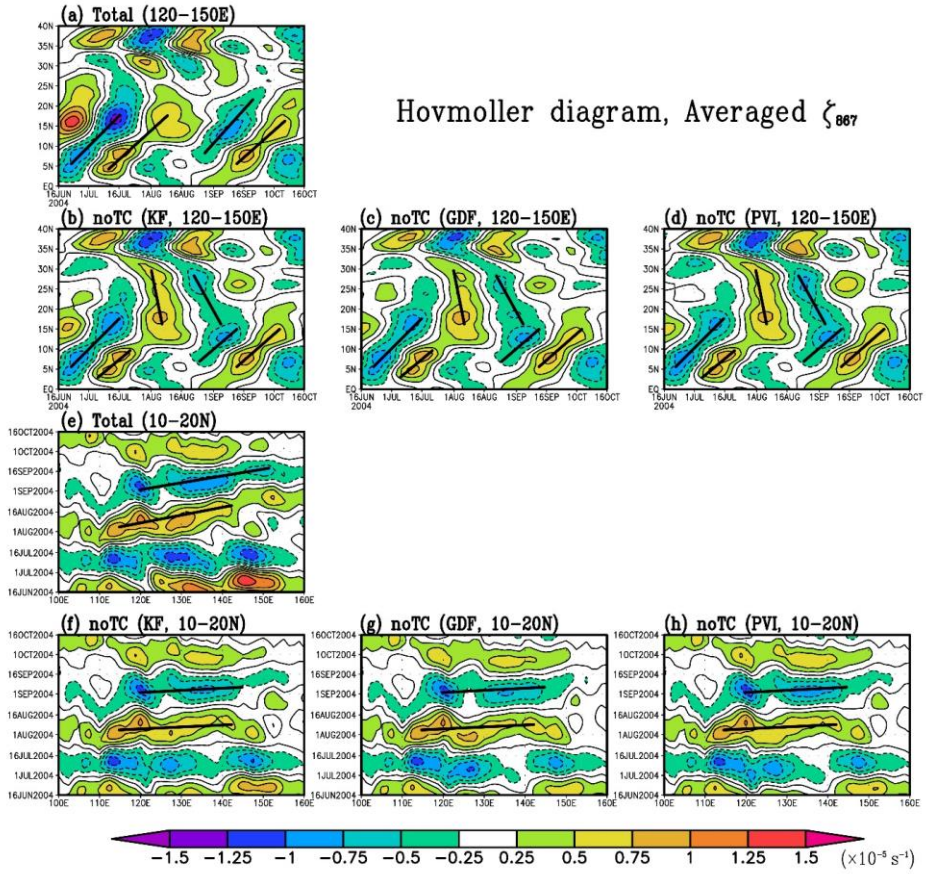

Fig. 3.15. Hovmöller diagrams of the 32–76-day filtered relative vorticity averaged over 120°E–150°E (color and contour) at 866.9 hPa. (a) JRA-55 reanalysis. (b–d) TC-removed field determined by the KF, GDF, and PVI, respectively. (e–h) As in (a–d), respectively, but averaged over 10°N–20°N. Contour interval is 0.25×10^{-5} s^{-1}. The lines in each panel indicate the ISO propagation.

3.4.2. Respective effects of TC-related positive and negative PV anomalies

The effect of negative PVA in TC is evaluated here. The contributions by tropospheric positive PVA and tropospheric and stratospheric negative PVAs for the wind, geopotential, and temperature fields during June–October 2004 are calculated by the PVI. Hereafter, the PVI calculation considering only positive PVA is referred to as the P-PVI and the original calculation considering both positive and negative PVAs as the PN-PVI.

Figure 3.16 shows the TC-removed fields on 23 August 2004 obtained by the P-PVI, and the corresponding vertical structures of the PN-PVI and P-PVI results are compared in Fig. 3.17. Although the expansion of subtropical anticyclone is observed as in the TC-removed fields obtained by the PN-PVI (Fig. 3.6), the magnitude of the anticyclone is stronger than the PN-PVI result (Figs. 3.16e,f,h,i). This is because upper-level

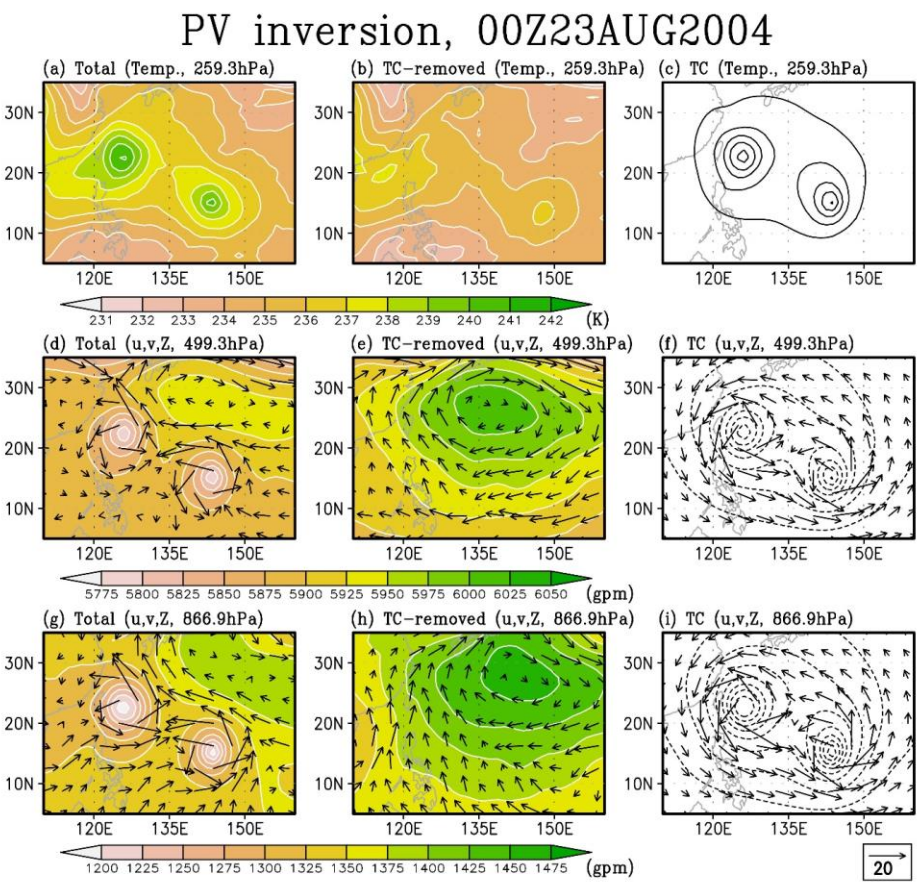

Fig. 3.16. As in Fig. 3.6, but for the results obtained by the P-PVI.

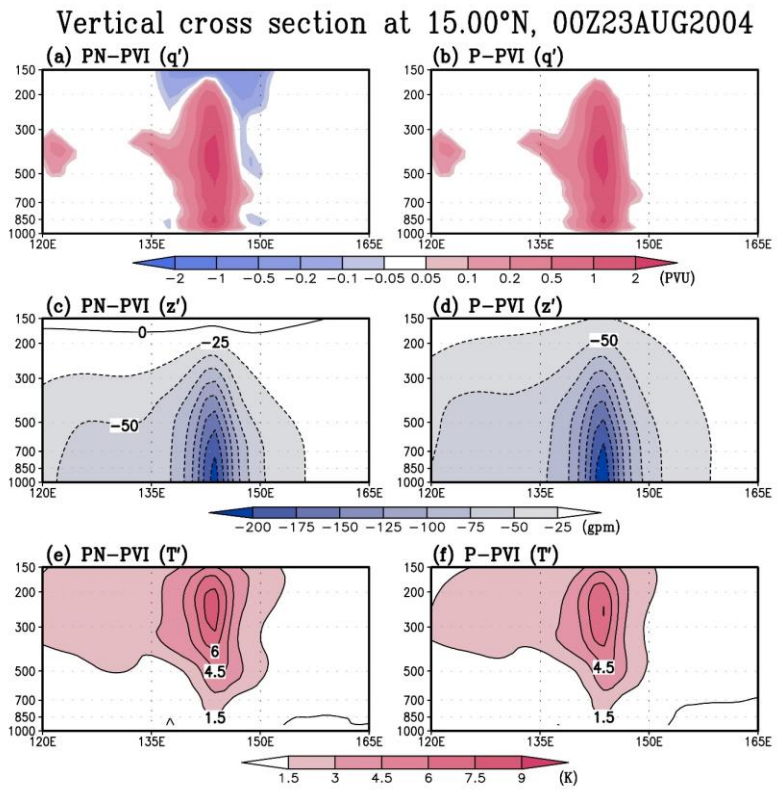

Fig. 3.17. The vertical cross-section at 15°N at 0000 UTC 23 August 2004 of TC-associated (top) PVA, (middle) geopotential height deviation, and (bottom) temperature anomaly. The left-hand (right-hand) column is derived from the result obtained by the PN-PVI (P-PVI).

Next, the upper-level TC-removed temperature field is examined. The TC-component of upper-level temperature is smaller in the P-PVI calculation than in the PN-PVI calculation (Figs. 3.6c, 3.16c, and 3.17e,f), resulting in the relatively higher temperature region in the TC-removed field near the TC center (Figs. 3.6b and 3.16b). To investigate the upper-level temperature in detail, the decomposed effect of PVAs is shown in Fig. 3.18. This indicates that the negative PVA in the troposphere induces not only an anticyclonic circulation but also a cold layer in the lower stratosphere and a warm layer in the upper troposphere (Figs. 3.18e,h). The temperature anomalies induced in the cold and warm layers are −1.5 K and 1.5 K, respectively, thus the negative PVA effect on upper-level temperature fields is not small. By contrast, the positive PVA induces cyclonic circulation throughout most of the troposphere with the maximum in the low level and a deep warm core in the troposphere. The effect of negative PVA in the lower stratosphere on the circulation in the middle-lower troposphere is relatively minimal compared with that of positive PVA (Figs. 3.18c,f,i). The net effect of both positive and negative PVAs associated with a TC appears to enhance the background large-scale circulations, namely a stronger low-level monsoon trough, a stronger upper-level anticyclone, and a warmer core throughout the troposphere. The effect of the thinner

upper-level negative PVA is essentially limited in the upper level, whereas the deep positive PVA has a much larger and deeper influence.

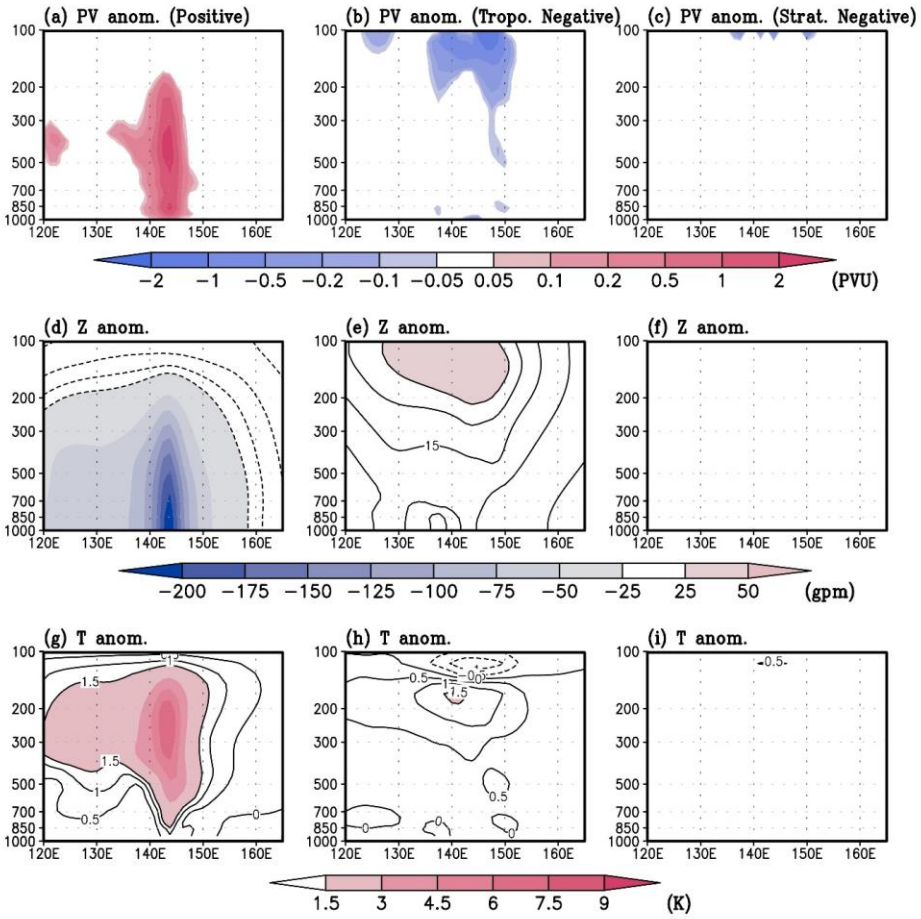

Fig. 3.18. The vertical cross-section at 15°N at 0000 UTC 23 August 2004 of TC-associated (a) tropospheric positive PVA, (d) geopotential height deviation (color and contour, contour interval is 5 gpm ranging from –20 to 20 gpm), and (g) temperature anomaly (color and contour: contour interval is 0.5 K ranging from –1 to 1 K). (b,e,g) As in (a,d,g), respectively, but for the tropospheric negative PVA. (c,f,i) As in (a,d,g), respectively, but for the stratospheric negative PVA.

Finally, the seasonal-mean upper-level temperature and low-level geopotential height in the TC-removed fields are shown in Fig. 3.19. Because of the weaker warm core structure obtained by the P-PVI (Figs. 3.17e,f), a smaller temperature reduction is observed compared with that caused by the PN-PVI (Figs. 3.19b,c). Moreover, compared with the result in the PN-PVI, the seasonal-mean low-level anticyclone becomes stronger in the P-PVI because there is no consideration of the negative PVA that suppresses the expansion of subtropical anticyclone (Figs. 3.19e,f). In contrast, the TC's low-level contribution to the 32–76-day ISV and the ISO propagation in the TC-removed field obtained by the P-PVI are almost the same as the results obtained by the PN-PVI because the

negative PVA effect on low-level wind field is much weaker (not shown).

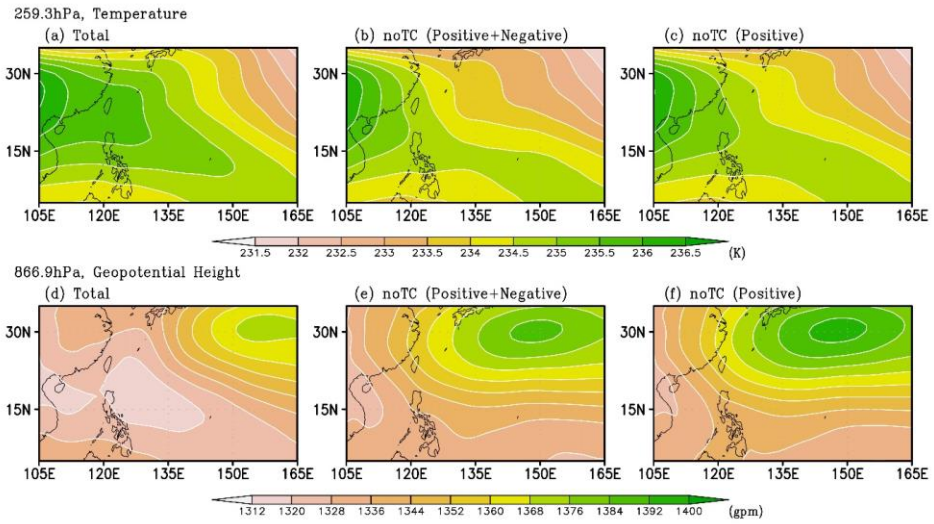

Fig. 3.19. Temperature (color and contour, in K) at 259.3 hPa for the time mean in June–October 2004: (a) JRA-55 reanalysis; TC-removed field obtained by (b) PN-PVI and (c) P-PVI. (d–f) As in (a–c), respectively, but for geopotential height at 866.9 hPa (in gpm).

In conclusion, removing positive PVA alone might be essentially enough for estimating the TC contribution to the low-level circulation. However, the negative PVA should be considered because the TC contribution induced by the negative PVA especially to the upper-level temperature field is not small.

3.5. Conclusion

By removing TC vortices in the global analysis and by evaluating the resultant differences, one may investigate the TC footprints on large-scale environmental fields. Although a method to remove the TC vortex proposed by Kurihara et al. (1995) has been widely used, it was unclear whether or not the TC-removed field obtained by the existing method is dynamically balanced. Here a methodology for constructing well-balanced TC-removed fields based on the PVI was proposed.

The proposed TC removal technique was unique in several respects. First, owing to the use of PVI, the obtained TC-removed fields at all levels were well-balanced in the framework of the PVI system. Second, although an averaging field was predefined when the PVA associated with TC was decomposed from the large-scale field, the effect of the TC-associated PVA was still included in the averaged field if it was calculated as a simple time

mean. The averaged field in the proposed technique was iteratively calculated using the TC-removed fields to reduce the TC residues in the averaged field. Third, the PVA associated with a TC was detected objectively at all layers, and the domain was not necessarily circular. Besides, a vertical vortex axis was defined, which prevented misinterpreting a PVA associated with other synoptic systems as the targeted TC perturbation. Thus, this algorithm did not extract PVAs associated with other synoptic systems that existed in the vicinity of the TC.

The Kurihara filtering method which was popular in TC simulations was compared with the proposed technique. The magnitude of the TC vortex calculated by the Kurihara filtering method was smaller. Furthermore, the Kurihara filtering method generated an unrealistic thick negative vorticity band encircling the TC center. In the TC-removed field, the Kurihara filtering method tended to retain a weak cyclonic circulation at the location where the removed TC originally existed. Such a weak cyclonic circulation no longer existed in the TC-removed field obtained by the technique proposed here. Moreover, TC vortices obtained by the proposed method have a more far-reaching influence than those obtained by the existing method. After the removal of TCs, the environmental field surrounding TCs remained largely unchanged in the existing method, while it changes markedly in the proposed method. Because of the marked change in the environmental field, one might doubt the validity of the proposed TC removal method. In general, TC is embedded in a larger circulation system, for example, the subtropical high and monsoon trough, and is surrounded by non-TC flows. The embedded TC suppresses these systems because of their strength. Besides, the PV has its dynamic impact on the far-field (the so-called electrostatics analogy; Bishop and Thorpe 1994; Thorpe and Bishop 1995). For this reason, it is expected that the derived mass and wind fields change in a region much larger than the TC domain after the removal of PVAs. Therefore, the appearance of marked changes in the environmental fields is not surprising considering the PV dynamics.

A new wind decomposition proposed by Galarneau and Davis (2013) was also compared. The TC contribution to the vorticity fields calculated by the GDF was the largest among the three methods because the GDF extracted not only the TC component of relative vorticity but also background vorticity. Moreover, in comparison with the irrotational wind component derived by Galarneau and Davis (2013) decomposition, the irrotational wind component obtained by the balanced omega equation system was smaller (not shown). As reported by Wang and Zhang (2003), this was an inherent problem when the velocity potential and vertical velocity were inverted by the balanced omega equation system. An adaptation of the Galarneau and Davis (2013) method may help enhance the underestimated irrotational wind. It would be better to use the method of Galarneau and

Davis (2013) to compute more accurate irrotational wind and vertical velocity in the TC-removed fields. For this reason, the method of Galarneau and Davis (2013) will be adopted to construct the long-term TC-removed dataset in Chapter 4 to compute the TC-related irrotational wind and vertical velocity components.

The KF, GDF, and the proposed technique were applied, following Hsu et al. (2008b), to evaluate the TC contribution to the intraseasonal variance and seasonal-mean fields over the tropical WNP during June–October 2004 and the results were compared. As reported by Hsu et al. (2008b), the summer was characterized by unusually strong TC and intraseasonal activity over the WNP, which reached a record high value in 50 years. The results obtained by the proposed method confirmed the significant contribution (up to 50%) of TCs to the intraseasonal variance along the TC tracks revealed by Hsu et al. (2008b). The strong northward propagating intraseasonal signals also weakened markedly after the TC removal. The TC contributions calculated by three TC removal schemes were consistent with the results of Hsu et al. (2008b), but the proposed PVI method revealed larger contributions of TCs than the KF.

Moreover, although the PV feature associated with TC is characterized by its tropospheric positive anomaly and negative anomaly in the upper troposphere and lower stratosphere, these individual effects were explored. The impact of TC on the large-scale monsoonal flow explored in this work focused mainly on the lower to middle troposphere where the well-defined positive PV dominated. The enhanced cyclonic flow presented in this work was a direct response to the removal of the positive PV in the lower-middle troposphere. However, negative PVA had a significant impact on the upper-level temperature. Thus, the negative PVA effect should be considered when the PVI is applied to TC studies. This finding will be also reflected in the construction of the long-term TC-removed dataset in Chapter 4.

Chapter 4. Tropical Cyclone Footprints in Long-Term Mean State and Multiscale Climate Variability over the Western North Pacific

4.1. Introduction

To examine TC footprints in climate variability in other variables in the troposphere, a sophisticated TC removal scheme was used in Chapter 3 to construct a TC-removed dataset for the WNP in which TC components were removed from all variables at all levels through the PV inversion in which the dynamic balance was maintained. TC structures were efficiently removed not only from the wind field, as in previous work, but also from other fields (e.g., geopotential height and temperature). The TC footprints in the climate variance in the low-level wind field during the WNP typhoon season in 2004 was slightly larger than that estimated by Hsu et al. (2008a,b). In Chapter 3, the intensification of the western flank of subtropical high, which is accompanied by a considerably weakened monsoon trough, and the upper-level cooling over the WNP were also identified after the removal of TC signals. Notably, the removal scheme was applied only to TCs in 2004; the TC footprints in long-term means and variabilities were not explored.

The present work revisits the TC footprint in the long-term climate means and variabilities between 1958 and 2019 by using the PV inversion technique employed in Chapter 3 to remove TC structures in winds, geopotential height, and temperature in the troposphere and lower stratosphere over the WNP. Moreover, the relationships between the existence of TC and the propagations of quasi-biweekly (10–20-day) and intraseasonal (20–80-day) oscillations over the WNP and between the interannual variations of TC genesis and the low-level vorticity field are explored. This work is organized as follows: Section 4.2 describes the data and methodology for the TC removal. TC footprints in seasonal and long-term means, interannual variability, and intraseasonal variability, and the relationship between the interannual variations of TC genesis and low-level relative vorticity field are reported in Section 4.3. Discussion and conclusion are presented in Section 4.4 and Section, 4.5, respectively.

4.2. Data and methods

In this work, the JRA-55 reanalysis and the RSMC-Tokyo best track data are used to detect TCs and their

center locations. All TC information over the WNP is recorded in the RSMC-Tokyo best track data from 1951 to the present. The JRA-55 reanalysis data are available in a 1.25° horizontal resolution in latitude and longitude and at 37 pressure levels for every 6 hours. Although the 1.25° horizontal resolution cannot resolve a realistic TC structure, the TC intensity and location are relatively better represented in the JRA-55 reanalysis than those in other reanalysis data, because TC surrounding winds are included in the data assimilation system (Murakami 2014).

In this work, the contributions of TCs to interannual and intraseasonal variabilities over the WNP between 1958 and 2019 are evaluated by comparing the variance between the original and TC-removed data. The interannual variance is calculated as the variance of the June–October seasonal mean in each year over this range. The intraseasonal components are extracted from the datasets through the application of a 20–80-day Butterworth bandpass filter.

TCs over the WNP that are recorded as Tropical Storm, Severe Tropical Storm, and Typhoon in the RSMC-Tokyo best track data are removed from the JRA-55 reanalysis. However, TC-related disturbances in the early and late stages of a TC (categorized as Tropical Depression or Extra-Tropical Cyclone) are not removed. The TC removal is performed based on the PV inversion technique originally proposed by Davis and Emanuel (1991). The PV inversion domain for the TC removal is from 0° to 60°N and from 90°E to 150°W. All target TCs for the removal are captured in the domain. To ensure stable calculation, the inhomogeneous vertical grid in pressure coordinates is reconstructed into the $\pi\ [= C_p(p/p_0)^{\kappa}]$ coordinate whose vertical grid interval is constant ($\Delta\pi = 0.02C_p$), where $\kappa = R_d/C_p$ is the ratio of the gas constant for dry air (R_d) to specific heat at a constant pressure (C_p), p is the pressure, and p_0 is the reference pressure (1000 hPa). The reconstructed data had 26 layers, satisfying $\pi = C_p$ at the bottom and $\pi = C_p/2$ at the top of the removal domain.

The removal procedure is performed as described in Section 3.2 except for the PVA decomposition for TCs and the estimation of TC components of irrotational wind and vertical velocity. To decompose a TC-related PVA, a TC domain must be determined. In Section 3.2, the TC domain at each level was determined by using a somewhat complicated and time-consuming process. In this work, the TC domain is simply defined as a cylinder of a specified radius from the TC center from 1000 to 88 hPa in the PV inversion domain. All positive and negative PVAs in the TC domain are referred to as the PVAs of the TC throughout this work. Using the PVAs, the TC components of geopotential height and virtual temperature are derived from the PPVI technique as described previously (Shapiro 1996; Wu and Emanuel 1995; Wang and Zhang 2003; Wu et al. 2003, 2004). Moreover, the

method of Galarneau and Davis (2013) is employed to determine the TC component of irrotational wind, not the balanced omega equation system, which removes a divergence anomaly within 1000 km from the TC center and derives the TC component of velocity potential from the divergence anomaly. As described in Section 3.5, this is because the TC component of irrotational wind obtained by the balanced omega equation system will be underestimated (Wang and Zhang 2003). Using the TC component of irrotational wind, the TC component of vertical velocity is derived from the continuity equation. Additionally, as the same as the divergence, the TC component of moisture is extracted from the total moisture field with a spatial filter which removes the moisture anomaly within 1000 km from the TC center. To obtain the TC-removed fields, the TC components are then subtracted from the original fields. Thus, the relationships among variables X in the original field (X_{total}), the TC-removed field (X_{noTC}), and the TC component (X_{TC}) can be expressed as $X_{\mathrm{total}} = X_{\mathrm{noTC}} + X_{\mathrm{TC}}$. For more details regarding the removal procedure, see Section 3.2.

As reported in Subsection 3.4.2, considering the TC-related negative PVAs in the upper level was vital when applying the PV inversion to TCs. In particular, accounting for the contribution of negative PVAs led to a better estimation of the warm core. As shown in Fig. 4.1, a radius of approximately 800 km from the TC center is sufficient to define the TC domain when considering only the positive PVA in the troposphere. By contrast, the negative PVA in the upper level is more widespread, and its distribution is highly asymmetric (Fig. 3.1). A larger domain is therefore needed. Notably, an excessively large TC domain would result in the removal of other convective systems near but not part of the TC. The results with radius settings at 600, 800, 1000 km are tested, and then the radius of the TC domain is set to 1000 km.[3]

[3] Note that the PV, divergence, and moisture anomalies in the domain are not completely removed. A removal rate function introduced in Kwon and Cheong (2010) was employed: the removal rate of the anomalies decrease as distance moving away from the domain center and it becomes zero at the maximum radius. Thus, it is considered that the effects of disturbances in the vicinity of TC are minimal on the results.

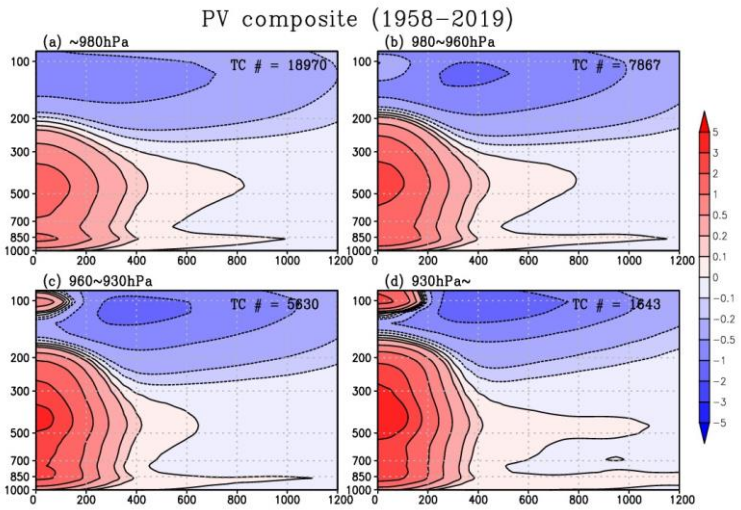

Fig. 4.1. Composites of a radial-height cross-section of a tangentially averaged PVA related to TCs (defined as a deviation from the averaged PV at 1500 km from the TC center), June–October 1958–2019 (in PV units: 10^{-6} m^2 kg^{-1} s^{-1} K). (a) TCs with minimum sea level pressure (MSLP) $<$ 980 hPa, (b) TCs for which 960 hPa $<$ MSLP $\leq$ 980 hPa, (c) TCs for which 930 hPa $<$ MSLP $\leq$ 960 hPa, and (d) TCs with MSLP $\leq$ 930 hPa. The horizontal and vertical axes represent the distance from the TC center and the pressure level (in km and hPa, respectively).

4.3. Results

4.3.1. TC footprints in climatological seasonal mean circulations

The TC and non-TC components are well separated by the present procedure. An example is shown in Fig. 4.2. At 1200 UTC 6 August 2019, three TCs have formed over the WNP: Tropical Storm Francisco at 35.1°N, 129.5°E, Typhoon Lekima at 19.5°N, 128.7°E, and Tropical Storm Krosa at 18.9°N, 142.4°E. The three TCs appear as isolated vortices in the low-level relative vorticity and geopotential height fields, and Typhoon Lekima and Tropical Storm Krosa are embedded in the monsoon trough (Figs. 4.2a,b). The corresponding warm cores are observable in the upper-level temperature field (Fig. 4.2c). Through the PPVI, the TC components are derived (Figs. 4.2g–i), and the TC-removed fields are obtained by subtracting the TC components from the total fields (Figs. 4.2d–f). The three vortices are cleanly removed from the original fields and other (non-targeted) disturbances are not removed. For example, a weak vortex over the SCS remains after the removal. The TC component of vorticity is localized, whereas the TC component of geopotential height is widespread. This is known as the far-field effect of PVAs (Bishop and Thorpe 1994; Thorpe and Bishop 1995). Owing to both the in situ and far-field

effects, the subtropical high becomes stronger and expands westward to cover most of the WNP after the TC removal. By contrast, the monsoon trough becomes considerably weaker and retreats westward to the SCS (Fig. 4.2e). The warm cores in the upper level are also thoroughly removed (Fig. 4.2f). The features observed in the TC-removed fields, such as the intensified subtropical high, weakened monsoon trough, and absence of warm cores are consistent with those noted in Fig. 3.6.

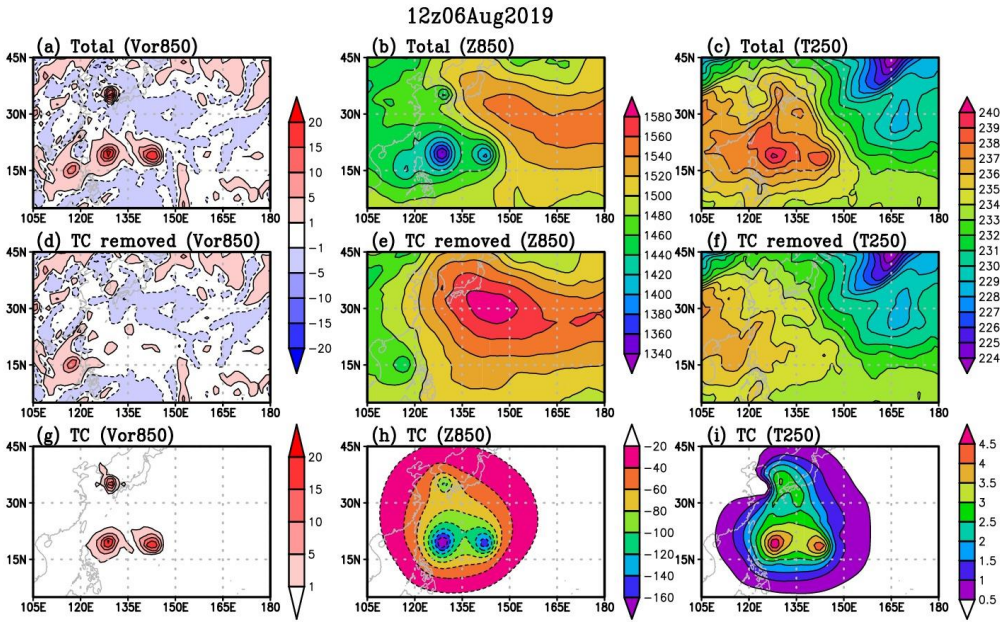

Fig. 4.2. (a) Relative vorticity at 850 hPa (in 10^{-5} s^{-1}), (b) geopotential height at 850 hPa (in gpm), and (c) temperature at 250 hPa (in K) at 1200 UTC 6 August 2019. (d–f) As in (a–c), respectively, but for the TC-removed fields. (g–i) As in (a–c), respectively, but for the TC components.

Figure 4.3 presents the climatological means of low-level vorticity, low-level geopotential height, and upper-level temperature during the typhoon season (June–October) from 1958 to 2019. After the TC removal, the positive vorticity related to the monsoon trough elongated at 15°N is weakened, and the negative vorticity related to the subtropical high south of Japan is strengthened (Figs. 4.3a,d). A weaker monsoon trough is therefore observable in the low-level geopotential height field. The elongated monsoon trough originally extending eastward over the SCS and the West Philippine Sea retreats westward (Figs. 4.3b,e). The enhanced negative vorticity area in Fig. 4.3d corresponded to the westward expansion and intensification of the subtropical high is seen in Figs. 4.3b,e. The reduction in the mean temperature in the upper troposphere is due to the removal of the TC warm core (Figs. 4.3c,f). The differences before and after the TC removal (Figs. 4.3g–i) demonstrate the size of TC footprints in both the amplitude and affected area. As manifested by a bullseye shape, the differences in vorticity span the SCS and

the northwestern Philippine Sea, whereas those in geopotential height and temperature cover almost the entire WNP. The affected area in geopotential height and temperature is larger because of the far-field effect of PV inversion. TCs often follow the background steering flow between the subtropical high and monsoon trough. Therefore, the areas of the largest TC footprints appear between the subtropical high and monsoon trough, exerting substantial contributions on both.

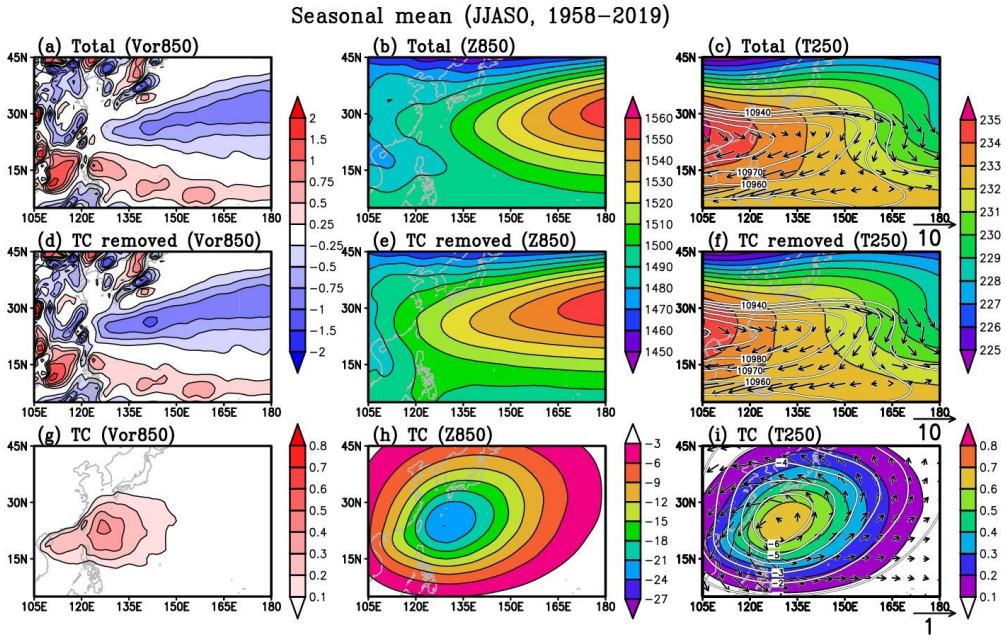

Fig. 4.3. As in Fig. 4.2, but for the climatological means, June–October 1958–2019. Geopotential height (contour) and wind (vector) are indicated in the column on the right. The geopotential height contour (wind vector) in (c,f) is omitted where the geopotential height is less than 10,940 gpm (where the wind speed is greater than 10 m s^{-1}).

The TC contribution extends throughout the troposphere and into the lower stratosphere. Figure 4.4 presents the vertical structure of the WNP monsoon system and the corresponding TC contribution along 130°E. The contribution to the mean geopotential height is characterized by a deep negative anomaly, the maximum of which is near the surface, which decays upward to the upper troposphere. The lower stratosphere is characterized by a positive anomaly. The corresponding contribution to temperature is distinguished by a positive anomaly, the maximum of which is in the upper troposphere, which decays downward to the surface. The lower stratosphere is distinguished by a negative anomaly. The negative geopotential height and positive temperature contributions in the deep troposphere are mainly related to the positive PVA in the troposphere, and the positive geopotential height and negative temperature contributions in the lower stratosphere are mainly related to the negative PVA in the

upper troposphere and lower stratosphere. The TC contribution to the atmospheric static stability can be investigated by the vertical profile of temperature. The vertical structure of climatological static stability and the corresponding TC contribution along 130°E are shown in Fig. 4.5. Since the height of climatological warm core maximum is at approximately 250 hPa (Fig. 4.4f), static stability in the TC-included mean field below (above) 250-hPa level is larger (smaller) than which in the TC-removed mean field (Fig. 4.5c). This TC footprint in static stability may suppress convections because larger static stability is unpreferable to excite convections.

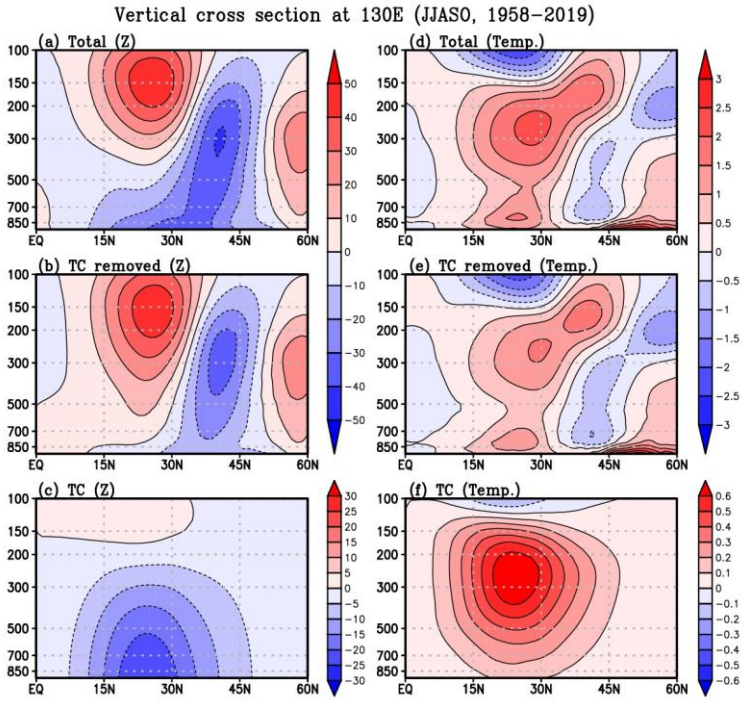

Fig. 4.4. Vertical cross-section of the climatological mean (June–October 1958–2019) of geopotential height (left, in gpm) and temperature (right, in K) at 130°E. (a,d) Total field, (b,e) TC-removed field, and (c,f) TC component. The deviations from the 90°E–150°W zonal means are shown to represent the spatial structure.

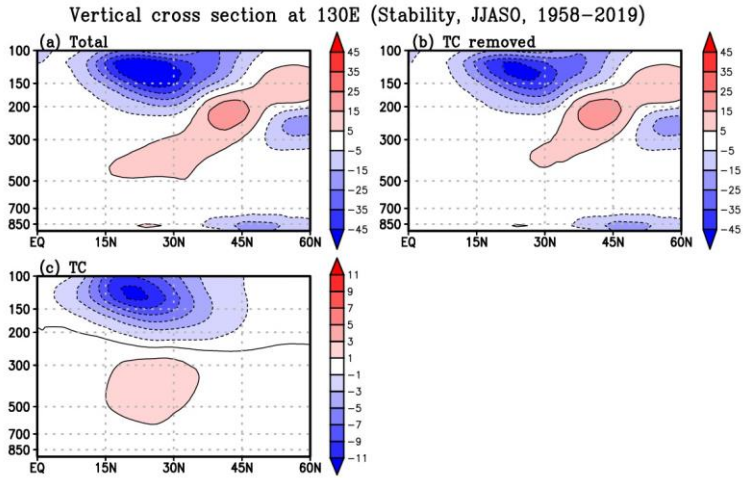

Fig. 4.5. Same as Figs. 4.4a–c, respectively, but for static stability defined as $-T\,\partial \ln\theta/\partial p$ (in 10^{-5} K Pa^{-1}).

The likelihood of TC formation is often estimated on the basis of the genesis potential index (GPI; Gray 1975, 1998; Emanuel and Nolan 2004; Camargo et al. 2007). The GPI proposed by Emanuel and Nolan (2004) is defined by

$$\mathrm{GPI} = |10^5\,\eta_{850}|^{1.5}\left(\frac{\mathrm{RH}_{700}}{50}\right)^3\left(\frac{V_{\mathrm{pot}}}{70}\right)^3\left(1+\frac{|V_{\mathrm{sh}}|}{10}\right)^{-2}, \tag{4.1}$$

where η_{850} is the climatological absolute vorticity at 850 hPa in s^{-1}; RH_{700} is the climatological relative humidity in percent; V_{pot} is the potential intensity in $\mathrm{m\,s}^{-1}$, which is calculated by climatological SST, vertical temperature profile, and sea level pressure (Emanuel 1986; Bister and Emanuel 2002); and V_{sh} is the climatological vertical wind shear between 850 and 200 hPa in $\mathrm{m\,s}^{-1}$. The powers on each factor in Eq. (4.1) are determined by comparing the monthly mean index and monthly cyclone number in each hemisphere in each month (Emanuel and Nolan 2004). As mentioned, these averages likely include distinct TC footprints. The background flow favorable to TC formation is represented when a portion of the TC footprint (e.g., low-level vorticity) is considered. On the other hand, the TC footprint included in the static stability represents unfavorable conditions. It is considered that indices showing the likelihood of TC genesis should not include the TC footprint itself. With these considerations, the TC footprint in the GPI is examined. The GPI and the respective factors calculated with the original data are shown in Fig. 4.6, and the TC contributions of the GPI and the factors are shown in Fig. 4.7. As shown in Fig. 4.3g, the TC contribution in the low-level vorticity is positive (Fig. 4.7b). The TC-related specific humidity is estimated by a spatial filter and the climatological TC-related specific humidity is positive everywhere

at 700 hPa. However, because of temperature reduction after the removal, positive and negative TC contributions are seen in the relative humidity at the level (Fig. 4.7c). Positive and negative TC contributions are also seen in the potential intensity (Fig. 4.7d). In the factor of vertical wind shear, positive TC contributions around Taiwan and negative TC contribution in the other region are seen (Fig. 4.7e; note that $1 + |V_{\mathrm{sh}}|/10 \geq 1$ and its power is negative). As a result, the TC contribution in the GPI is positive around Taiwan (up to 30%) and negative in the other region of the WNP (Fig. 4.7a), but overall, no significant changes have been observed. TC contributions in the moisture field and potential intensity would be underestimated, thus leading to underestimated GPI. This issue is discussed in Chapter 5.

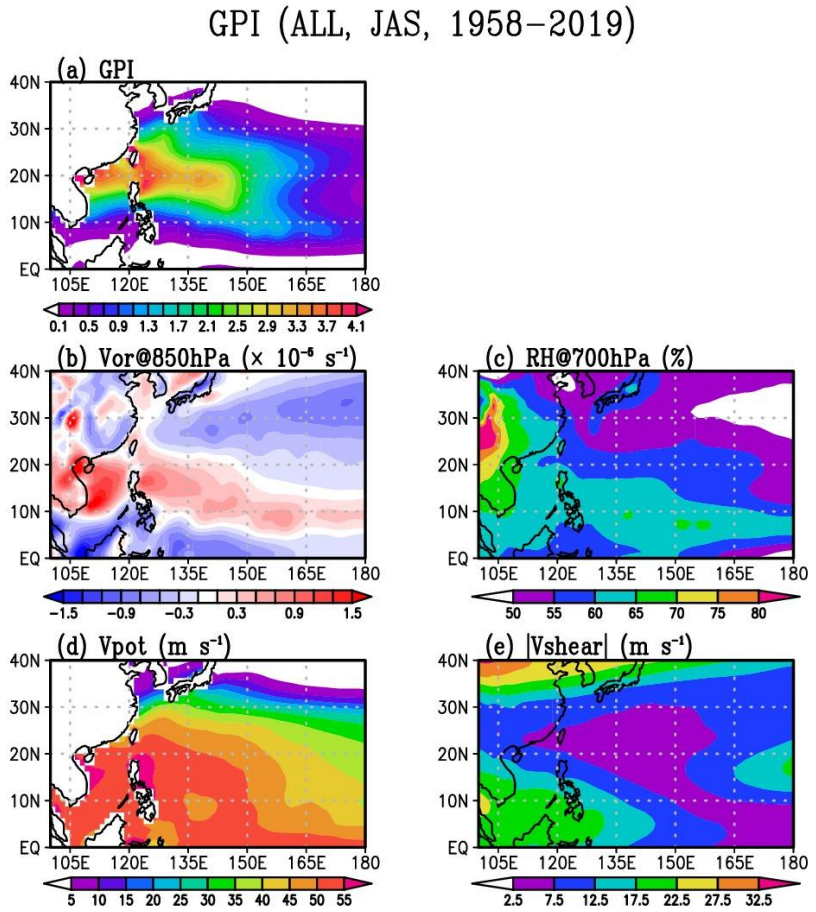

Fig. 4.6. Climatological seasonal mean (July–September 1958–2019) GPI and respective factors calculated using original data. (a) GPI, (b) relative vorticity at 850 hPa (s^{-1}), (c) relative humidity (%), (d) potential intensity (m s^{-1}), and (e) magnitude of vertical wind shear between 850 to 200 hPa (m s^{-1}).

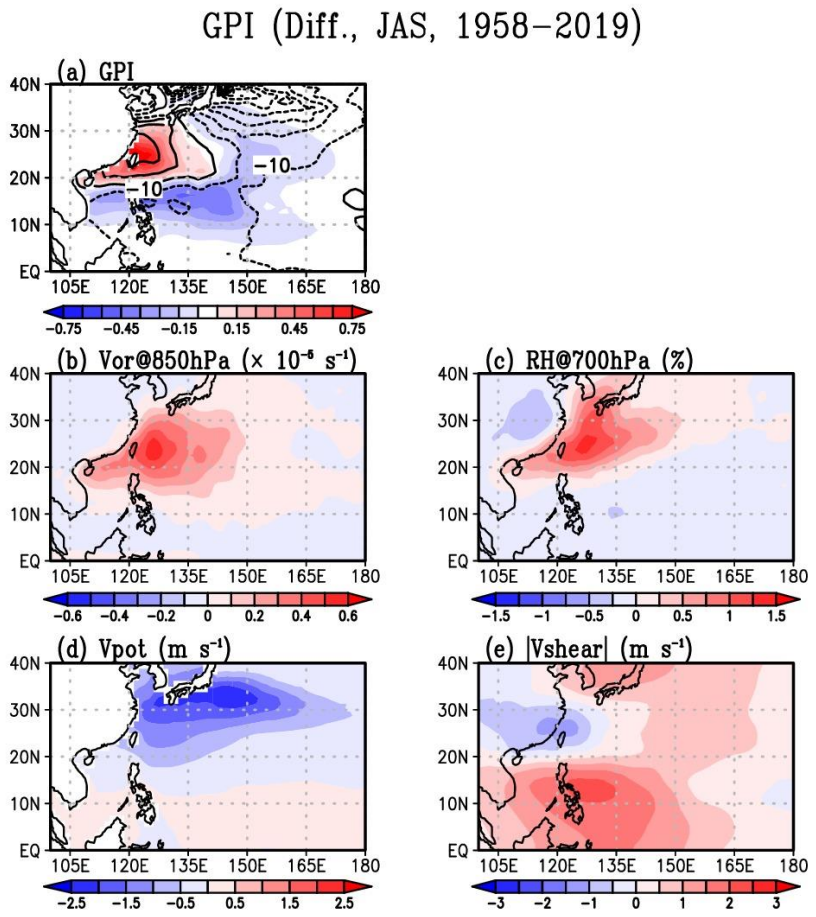

Fig. 4.7. Same as Fig. 4.6 but showing the difference between fields calculated using original and TC-removed data. Contour in (a) indicates TC contribution (%).

4.3.2. TC footprints in the interannual variability

According to the RSMC-Tokyo best track data, the number of TCs over the WNP varies each year between 1958 and 2019, ranging from 14 to 39 overall. To examine the impact of differences in the number of TCs on the seasonal mean, the June–October mean fields are compared in the 3 years in which TCs are the most active (1994, 1967, and 1966; total 91) and inactive (1998, 1969, and 2010; total 37). The distributions of seasonal mean monsoon trough and subtropical high differ considerably in the active and inactive years (Fig. 4.8). Specifically, in the active years, the subtropical high is weaker and confines to the east (e.g., the 1510-gpm contour is located east of 150°E) and the monsoon trough extends eastward to 140°E (Fig. 4.8a), indicating a strong monsoon trough and a weak subtropical high that favor TC genesis and development. In the inactive years, a strong western flank of subtropical high extends westward to eastern China. The monsoon trough is confined to the west of 110°E and is

not observable over the Philippine Sea (Fig. 4.8d), reflecting an unfavorable environment for TC genesis and development. This interpretation is based on the concept that an environment dominated by large-scale circulation determines TC genesis and development. This is correct in general. On the contrary, the results discussed thus far and in the study by Hsu et al. (2008a) suggest the following: the analysis of seasonal mean circulation (Figs. 4.8a,d) likely ignores the large TC footprints in the mean flow statistics because of the inability of time-averaging and low-pass filtering to cleanly remove the strong vortices and precipitation embedded in TCs.

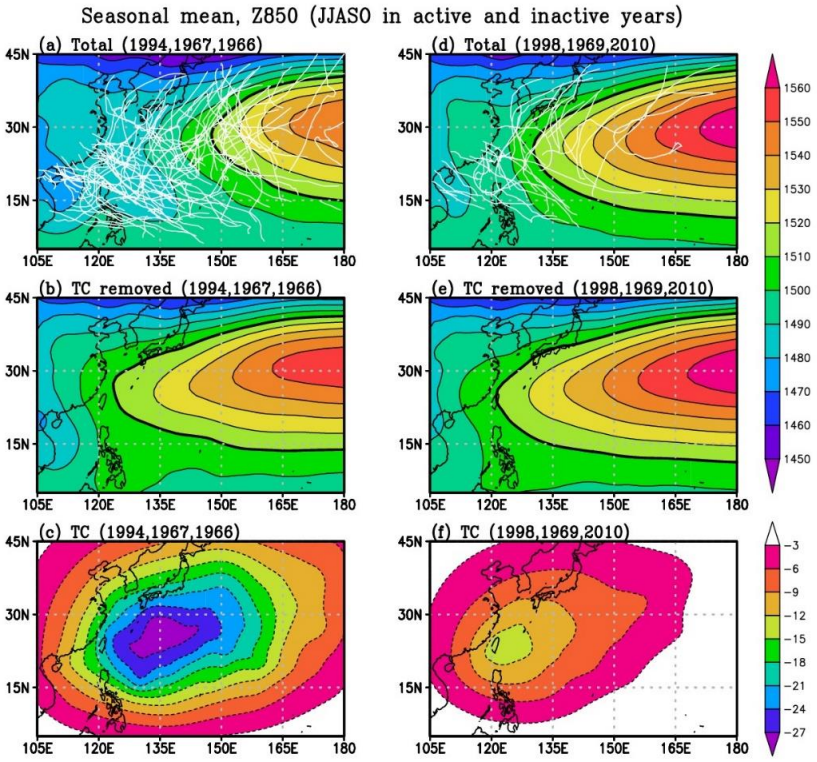

Fig. 4.8. Seasonal mean of the geopotential height at 850 hPa (in gpm) from June to October in the 3 years in which the most TCs occurred (1994, 1967, and 1966): (a) Total field, (b) TC-removed field, and (c) TC component. (d–f) As in (a–c), respectively, but for the 3 years in which the fewest TCs occurred (1998, 1969, and 2010). The thick solid line in the top and middle row panels marks the 1510-gpm contour. The white lines in (a) and (b) denote the tracks of TCs that occurred in the active and inactive years, respectively.

The strength of the TC footprint is dependent on TC activity and the degree of clustering: the stronger the activity and clustering, the larger the footprint. The contrast of the TC component of geopotential height is observable in Figs. 4.8c,f. The bullseye-like negative anomaly coinciding with the TC-prevailing region is stronger in the active years and covers a larger region; by contrast, it is weaker and spans a smaller region in the inactive years. The maximum anomaly in the active years exceeds 28 gpm, more than twice as large as that in the inactive

years (13 gpm). The large differences between the TC footprints reflect the fact of the substantially stronger (weaker) monsoon trough and weaker (stronger) subtropical high in the active (inactive) years (Figs. 4.8a,d). The seasonal mean monsoon trough and subtropical high remain almost unchanged after the removal of TCs in the inactive years; by contrast, in the active years, the monsoon trough over the Philippine Sea disappears completely and the subtropical high expands considerably westward. The geopotential height contrast between the active and inactive years becomes almost indistinguishable after the TC removal (Figs. 4.8b,e), indicating that the interannual variation between the active and inactive years is strongly affected by TC footprints. A similar contrast before and after the TC removal is noted in all other variables, including winds, vorticity, and temperature.

The interannual variance of the June–October seasonal-mean relative vorticity at 850 hPa from 1958 to 2019 is shown in Fig. 4.9. A region exhibiting large vorticity variance is observed over the ocean east of Taiwan and the Philippines (Fig. 4.9a) but disappears in the TC-removed field (Fig. 4.9b). The TC contribution to the interannual variance (Fig. 4.9c) is defined as the difference between variances in the total and TC-removed fields, or $\mathrm{Var}(X_{\mathrm{total}}) - \mathrm{Var}(X_{\mathrm{noTC}})$, where $\mathrm{Var}(X)$ represents the variance of variable X. As reported by Hsu et al. (2008a), the distribution of the TC contribution shown in Fig. 4.9c corresponds with TC tracks in which the maximum occurs near the largest TC passing point. Figure 4.9d presents the TC contribution ratio, defined as the ratio of the TC contribution to the total variance, or $1 - \mathrm{Var}(X_{\mathrm{noTC}})/\mathrm{Var}(X_{\mathrm{total}})$. The ratio generally exceeds 40% along the TC tracks that cover almost the entire subtropical WNP from 120°E to 160°E. Overall, apart from a slightly larger contribution ratio, the TC footprint in the interannual variance of the low-level vorticity is consistent with that in Hsu et al. (2008a).

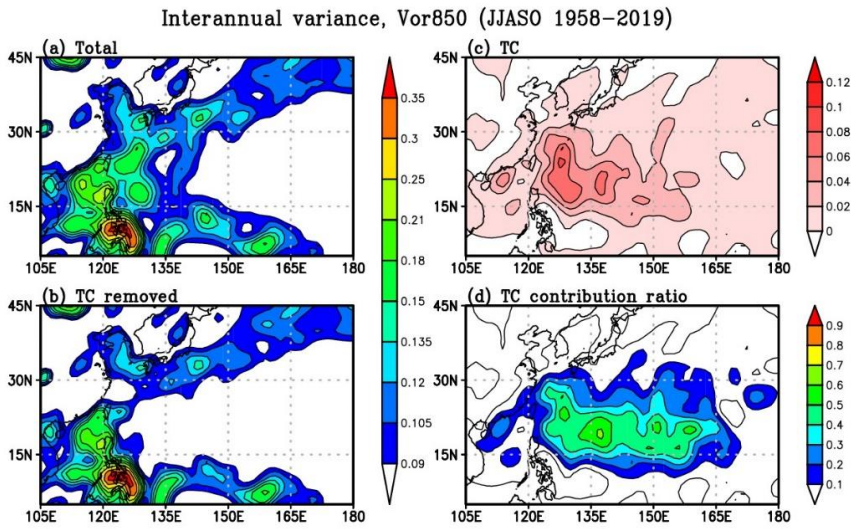

Fig. 4.9. Interannual variance of 850-hPa relative vorticity (in 10^{-10} s^{-2}), June–October 1958–2019: (a) Total field, (b) TC-removed field, (c) TC contribution, and (d) TC contribution ratio. The contour intervals in (c) and (d) are 0.02×10^{-10} s^{-2} and 0.1, respectively.

As shown in Fig. 4.10, the features of the TC contributions of interannual variances in low-level geopotential height and upper-level temperature differ from those of interannual variances in low-level relative vorticity. Positive TC contributions are noted in a large region over the subtropical WNP, with the center near 20°N, 155°E (Fig. 4.10b), and negative contributions are observed over Korea, Japan, and the East China Sea (Fig. 4.10e). The reason behind the negative contribution is discussed as follows. Under the assumption of the linear relationship for variable X ($X_{\text{total}} = X_{\text{noTC}} + X_{\text{TC}}$), the variance of X_{total} can be decomposed as follows:

$$\begin{aligned}\text{Var}(X_{\text{total}}) &= \overline{X_{\text{total}}^2} - \overline{X_{\text{total}}}^2 = \overline{(X_{\text{noTC}} + X_{\text{TC}})^2} - \overline{X_{\text{noTC}} + X_{\text{TC}}}^2, \\ &= \left(\overline{X_{\text{noTC}}^2} - \overline{X_{\text{noTC}}}^2\right) + \left(\overline{X_{\text{TC}}^2} - \overline{X_{\text{TC}}}^2\right) + 2(\overline{X_{\text{noTC}} X_{\text{TC}}} - \overline{X_{\text{noTC}}}\,\overline{X_{\text{TC}}}), \\ &= \text{Var}(X_{\text{noTC}}) + \text{Var}(X_{\text{TC}}) + 2\,\text{Cov}(X_{\text{noTC}}, X_{\text{TC}}),\end{aligned}$$

where $\overline{[\,]}$ denotes the time average for a specified period and $\text{Cov}(X_{\text{noTC}}, X_{\text{TC}})$ is the covariance of X_{noTC} and X_{TC}. Thus, the TC contribution can be expressed as $\text{Var}(X_{\text{total}}) - \text{Var}(X_{\text{noTC}}) = \text{Var}(X_{\text{TC}}) + 2\,\text{Cov}(X_{\text{noTC}}, X_{\text{TC}})$. Although $\text{Var}(X_{\text{TC}})$ is always non-negative, the sign of $\text{Cov}(X_{\text{noTC}}, X_{\text{TC}})$ is dependent on the relationship between the distributions of X_{noTC} and X_{TC}. In the low-level vorticity, the covariance term of the TC-removed field and the TC component in the TC-active region is negative but its magnitude is smaller than the variance of the TC component (Fig. 4.11), explaining the positive TC contribution spread across the region. However, in the low-level geopotential height and upper-level temperature, the magnitudes of negative covariance

in the TC-active region exceed those of the variances of the TC component in the area surrounding the East China Sea (Fig. 4.12). As a result, the bipolar structures of the TC contributions are observed. Therefore, the TC contribution strongly depends on the distribution and magnitude of $\mathrm{Cov}(X_{\mathrm{noTC}}, X_{\mathrm{TC}})$. A larger negative magnitude of $\mathrm{Cov}(X_{\mathrm{noTC}}, X_{\mathrm{TC}})$ tended to be seen when an extent of TC footprint was larger in an additional analysis (not shown). The contrast can be understood physically in terms of the prevailing circulation regimes: the western flank of subtropical high in the north and the monsoon trough in the south. As shown in Fig. 4.3, the weakened monsoon trough and strengthened subtropical high are found when TC footprints are neglected. These are related to the fact that TCs mainly translate along the western flank of the subtropical high, causing a decrease in geopotential along the western flank, and thus, an apparent retreat of the flank to the east. Therefore, the year-to-year fluctuation in TC activity amplifies the interannual fluctuation of the monsoon trough and diminishes the interannual fluctuation of the western flank of subtropical high over the WNP.

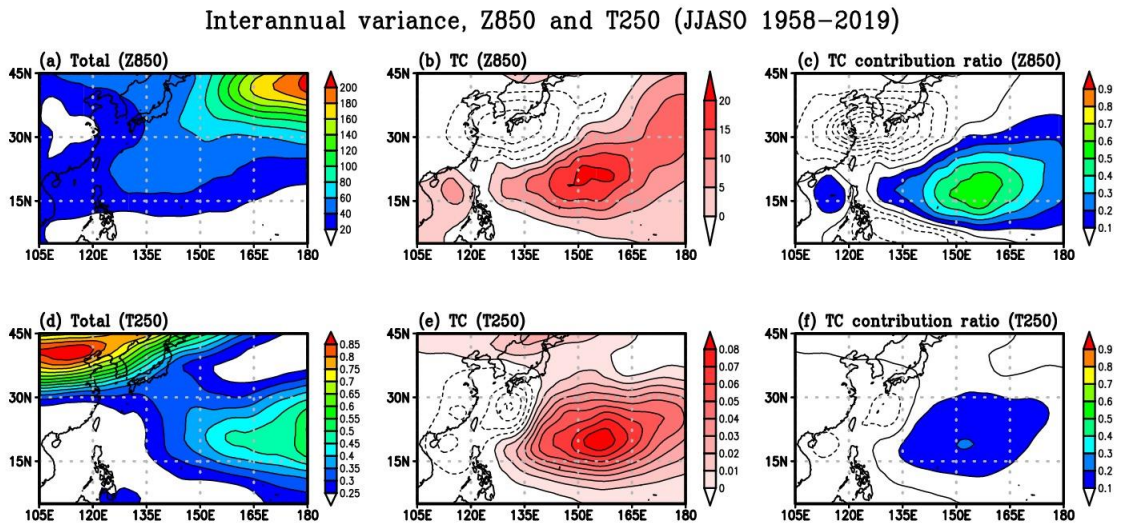

Fig. 4.10. (a–c) Interannual variance of 850-hPa geopotential height (in gpm^2), June–October 1958–2019. (a) Total field, (b) TC contribution, and (c) TC contribution ratio (dimensionless). (d–f) As in (a–c), respectively, but for temperature at 250 hPa (in K^2). The contour interval is 5 gpm^2 in (b), 0.01 K^2 in (e), and 0.1 in (c) and (f).

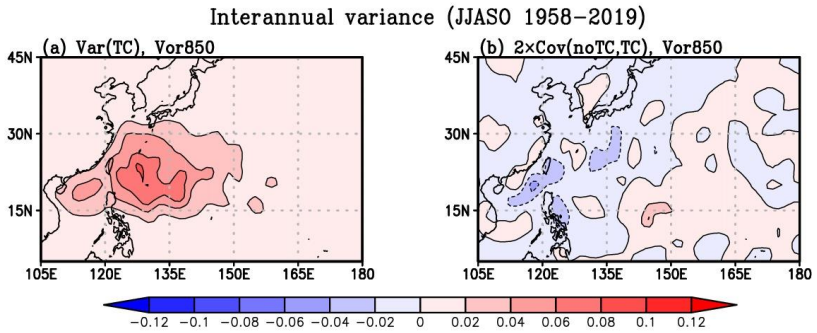

Fig. 4.11. Interannual variance and covariance of 850-hPa relative vorticity (in 10^{-10} s^{-2}), June–October 1958–2019. (a) Interannual variance of TC component and (b) Twice the interannual covariance of TC and non-TC components. The contour interval is 0.02×10^{-10} s^{-2}.

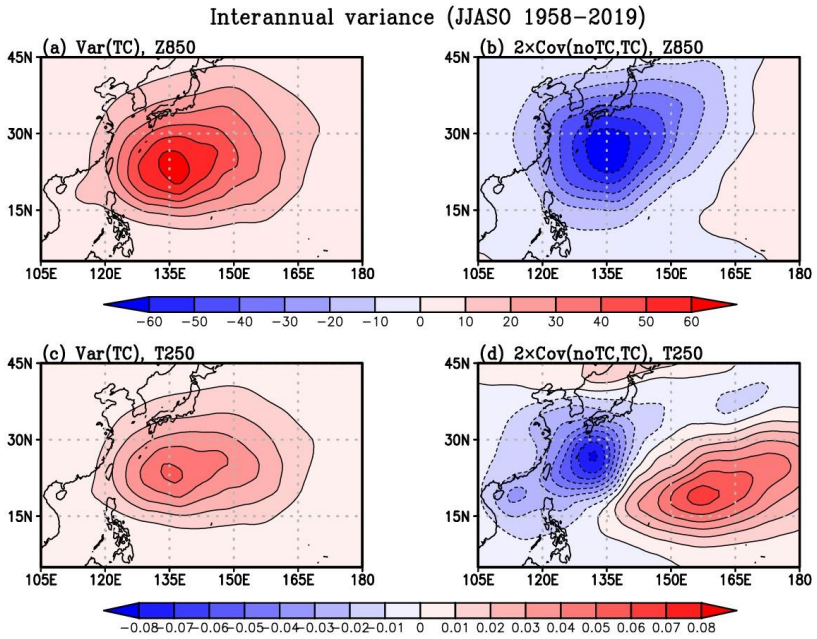

Fig. 4.12. (a,b) As in Fig. 4.11a,b, respectively, but for 850-hPa geopotential height (in gpm^2). The contour interval is 10 gpm^2. (c,d) As in (a,b), respectively, but for 250-hPa temperature (in K^2). The contour interval is 0.01 K^2.

The TC contribution ratio of the low-level geopotential height exceeds 50% at 20°N, 155°E, and the positive contribution area expands eastward from 130°E (Fig. 4.10c). The distribution of the TC contribution ratio in the upper-level temperature is similar to that in the low-level vorticity, but the maximum ratio is approximately 20% (Fig. 4.10f). By contrast, the negative TC contributions around the East China Sea in the low-level geopotential height and upper-level temperature exceed 70% and 10%, respectively. This indicates that if the TC footprints were not considered, the monsoon trough and the western flank of subtropical high would experience less

and more vigorous fluctuations, respectively. The negative contributions in the low-level geopotential height and the upper-level temperature appear to be larger than those in the low-level vorticity. This can be attributed to the far-field effect of PV inversion that expands the affected region.

The teleconnection pattern, called the Pacific–Japan (PJ) pattern, is caused by enhanced convection over the WNP east of the Philippines: the enhanced convection coincides with low-level anomalous cyclonic and anticyclonic circulations near the Philippines and over Japan, respectively (Nitta 1987). As shown in Figs. 4.3 and 4.9, TC activities are considered to influence the convections seasonally and interannually over the WNP east of the Philippines. Thus, the TC activity is expected to affect the PJ pattern. Here, the relationship between the TC activity and PJ pattern is examined.

By applying an empirical orthogonal function (EOF) analysis to June–October mean 850-hPa relative vorticity anomalies from 1977 to 2019 after removing its trend and applying horizontal smoothing, the first EOF mode (EOF1) and second EOF mode (EOF2) are extracted. The EOF1 and EOF2 are shown in Figs. 4.13a,b, respectively. Using the corresponding time series of principal components (PC1 and PC2), the spatial patterns of the 850-hPa TC-removed relative vorticity anomalies regressed onto the PC1 and PC2 are shown in Figs. 4.13c,d, respectively. Moreover, these differences, which are considered as TC footprints in the PJ pattern, are shown in Figs. 4.13e,f, respectively. The variance fraction explained by the EOF1 (EOF2) is 25.8% (18.4%). Although the PJ pattern is extracted as EOF1 in the previous studies, based on the spatial patterns, the EOF1 is considered to correspond to the Mariana-Bonin pattern (Takemura and Mukougawa 2021) and the EOF2 is considered to correspond to the PJ pattern in this analysis. The discrepancy is perhaps because the many previous studies used the monthly-mean data during June to August (Kosaka and Nakamura 2006; 2008; 2010), while this analysis uses the June–October mean data. In fact, the EOF analysis with the June–August mean data extracts the PJ pattern as EOF1 (24.6% of total variance) and the Mariana-Bonin pattern as EOF2 (20.6% of total variance) (not shown). In this study, the June–October mean data is used in the analysis of PJ pattern because the same 5-month mean data is used to estimate the TC contribution to the interannual variance. The PJ pattern analyzed in the TC-removed relative vorticity show a decrease in amplitude over the Philippine Sea compared to the PJ pattern observed in the original relative vorticity (Figs. 4.13b,d). Therefore, the bipolar structure of positive anomaly near the Philippine Sea and negative anomaly over Japan, which are observed in the original PJ pattern, appears to be shifted by 1° or 2° to the south in the TC-removed PJ pattern especially in the region between 115°E and 135°E.

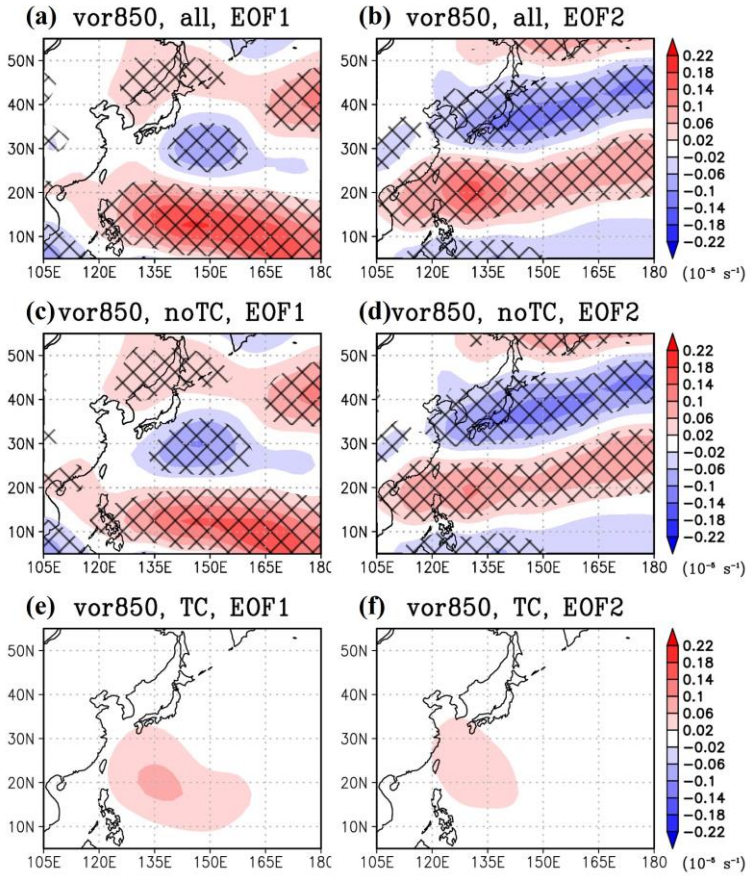

Fig. 4.13. (a) EOF1 spatial pattern of the June–October mean 850-hPa relative vorticity over the WNP (5°N–55°N, 105°E–180°) for the period 1977–2019 (in 10^{-5} s^{-1}). The variance explained by EOF1 is 25.8%. (b) Same as (a) but for EOF2. The variance explained by EOF2 is 18.4%. (c) The TC-removed 850-hPa relative vorticity regressed onto the standardized PC1 corresponding to (a). (d) Same as (c) but regressed onto the standardized PC2 corresponding to (b). (e,f) TC footprints in the EOF1 [differences between (a) and (c)] and EOF2 [differences between (b) and (d)], respectively. The cross-hatch areas in (a–d) indicate statistically significant at the 5% level by a two-sided Student's *t*-test (effective sample size: 43).

Next, Fig. 4.14 shows the spatial pattern of the low-level geopotential height anomalies regressed onto PC1 and PC2 obtained by the low-level relative vorticity anomalies. Corresponding to the bipolar structure of the PJ pattern seen in the relative vorticity anomalies, negative anomalies over the Philippine Sea and positive anomalies over Japan are also observed in the low-level geopotential height anomalies (Fig. 4.14b). After the TC removal, the negative anomaly is largely reduced, and the positive anomaly is largely increased and expand to the west. As a result, though the southward movement of the bipolar structure in the PJ pattern seen in the relative vorticity anomaly in the region between 115°E and 135°E is slight (Figs. 4.13b,d), it is clearly observed in the PJ pattern seen in the geopotential height anomaly (Figs. 4.14b,d). As can be understood from the comparison between

Fig. 4.13f and Fig. 4.14f, this is certainly because the range of TC contribution (or TC footprint) in the low-level geopotential height is larger than the range in the low-level relative vorticity.

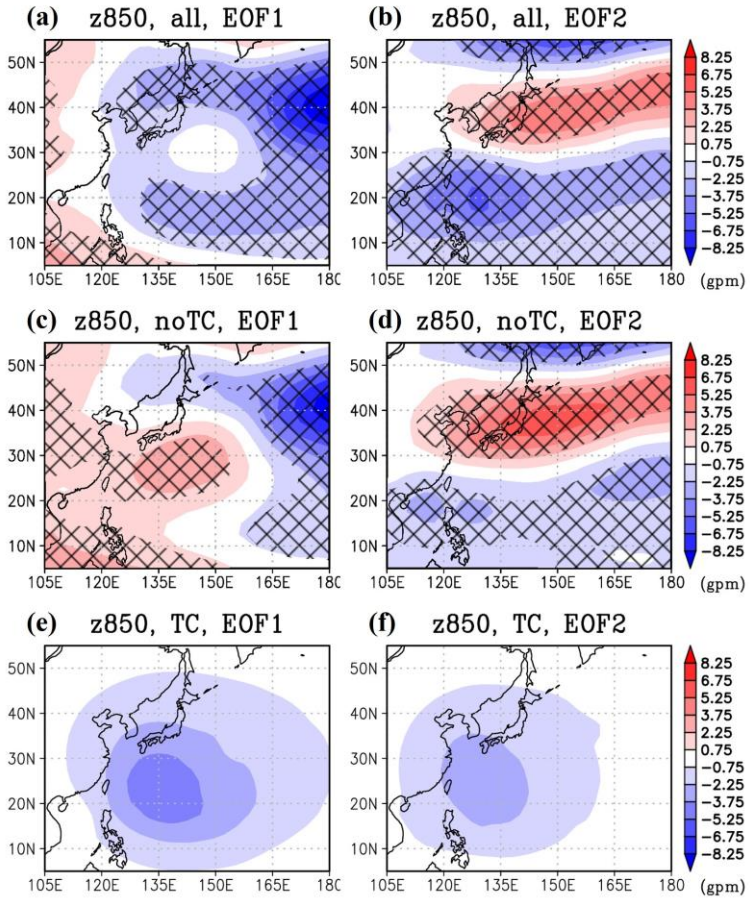

Fig. 4.14. (a) The 850-hPa geopotential height regressed onto the standardized PC1 corresponding to Fig. 4.13a (in gpm). (b) Same as (a) but regressed onto the standardized PC2 corresponding to Fig. 4.13b. (c,d) Same as (a,b), respectively, but for the TC-removed geopotential height. (e,f) TC footprints in the EOF1 [differences between (a) and (c)] and EOF2 [differences between (b) and (d)], respectively. The cross-hatch areas in (a–d) indicate statistically significant at the 5% level by a two-sided Student's *t*-test (effective sample size: 43).

The above discussions suggest that the TC activity and PJ pattern are related. To further investigate this relationship, the time series of standardized PC2 and the June–October mean of TC components of area-averaged low-level relative vorticity and geopotential height over the Philippine Sea (10°N–30°N, 120°E–150°E) are shown in Fig. 4.15. The correlation coefficient between the PC2 and area-averaged low-level relative vorticity is 0.39 (Fig. 4.15a), and that between the PC2 and area-averaged low-level geopotential height is −0.42 (Fig. 4.15b), indicating moderate correlations between the PC2 and TC components.

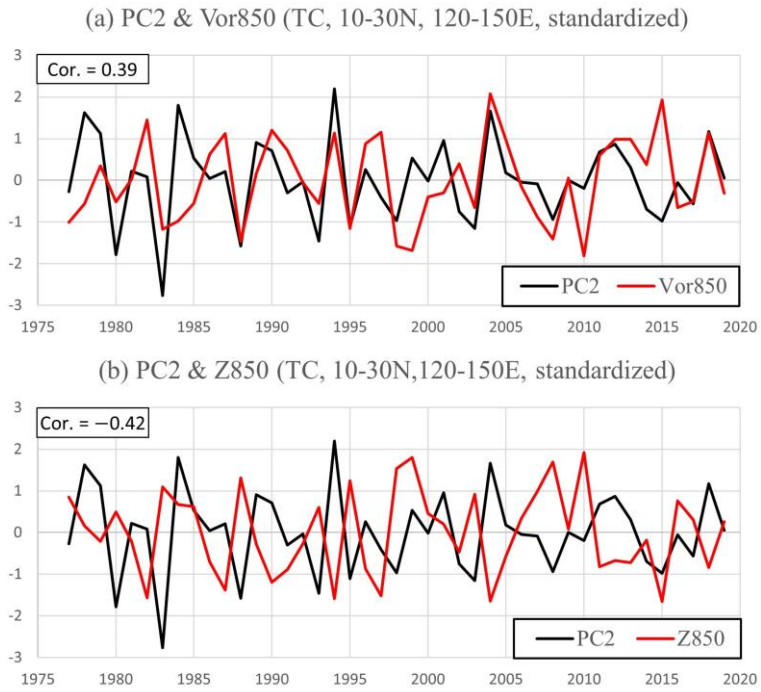

Fig. 4.15. (a) Time series of PC2 corresponding to Fig. 4.13b (black line) and TC component of area-averaged (10°N–30°N, 120°E–150°E) 850-hPa relative vorticity (red line). Both are standardized and the correlation coefficient is shown in the upper-left. (b) Same as (a) but for 850-hPa geopotential height.

4.3.3. TC footprints in the intraseasonal variability

Hsu et al. (2008a,b) reported that TC footprints in the intraseasonal variance of the low-level vorticity in the major regions of the clustered TC tracks exceeded 50%. Here, the contribution of TCs to the intraseasonal variance is evaluated to answer the following two questions. Could a similar contribution be identified in the dataset constructed using the new TC removal technique? Would such a large contribution also be observable in other variables at other levels?

Figure 4.16 shows the intraseasonal variance in vorticity at 850 hPa between 1958 and 2019. The intraseasonal component is extracted by applying a 20–80-day Butterworth bandpass filter to unfiltered data. In the original field with TCs, a large vorticity variance is observed over the northern SCS and the northwestern Philippine Sea between Taiwan and Japan (Fig. 4.16a). This variance vanishes after the TC removal (Fig. 4.16b). The largest reduction, which means the TC footprint, is noted over almost the entire region in which major variance is observed (Fig. 4.16c), with the TC contribution ranging from 30% to greater than 70% (Fig. 4.16d). This region

is near the clustered TC tracks and the recurvature area of the TCs, where they tend to reach the maximum intensity.

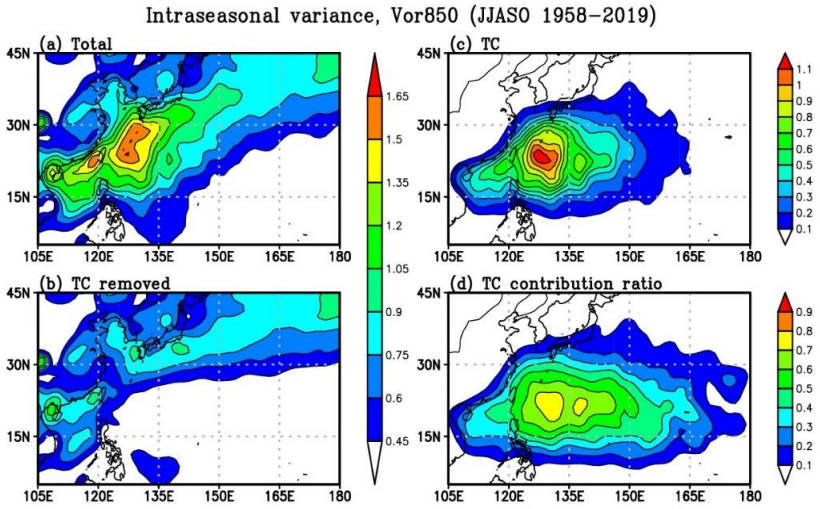

Fig. 4.16. Intraseasonal (20–80 day) variance of 850-hPa relative vorticity (in 10^{-10} s^{-2}) in June–October 1958–2019: (a) Total field, (b) TC-removed field, (c) TC contribution, and (d) TC contribution ratio (dimensionless). The contour intervals in (c) and (d) are 0.1×10^{-10} s^{-2} and 0.1, respectively.

The intraseasonal variances of low-level geopotential height and the upper-level temperature are shown in Figs. 4.17a,d, respectively. Similar to the results of the low-level vorticity, the largest TC contributions in both the variables are observed near the largest TC passing area (Figs. 4.17b,e). The TC contribution ratio in the low-level geopotential height and the upper-level temperature is more than 60% and 50%, respectively, with the major contribution region covering the northern SCS and the Philippine Sea (Figs. 4.17c,f). As in the interannual variance, the negative TC contribution in the low-level geopotential height is observed around 35°N, 115°E, and 10°N, 155°E. Unlike the TC contribution to the interannual variance over the Philippine Sea where the subtropical high and the monsoon trough prevail, the distribution of the positive TC contributions to the intraseasonal variance is widespread, centered near the largest TC passing area.[4]

[4] As in the interannual variances of the low-level vorticity and upper-level temperature in most part of the WNP, correlations between the no-TC and TC components for the intraseasonal variances over the whole WNP were low. Therefore, a weak relationship between the TC-free large-scale circulation and TCs is indicated.

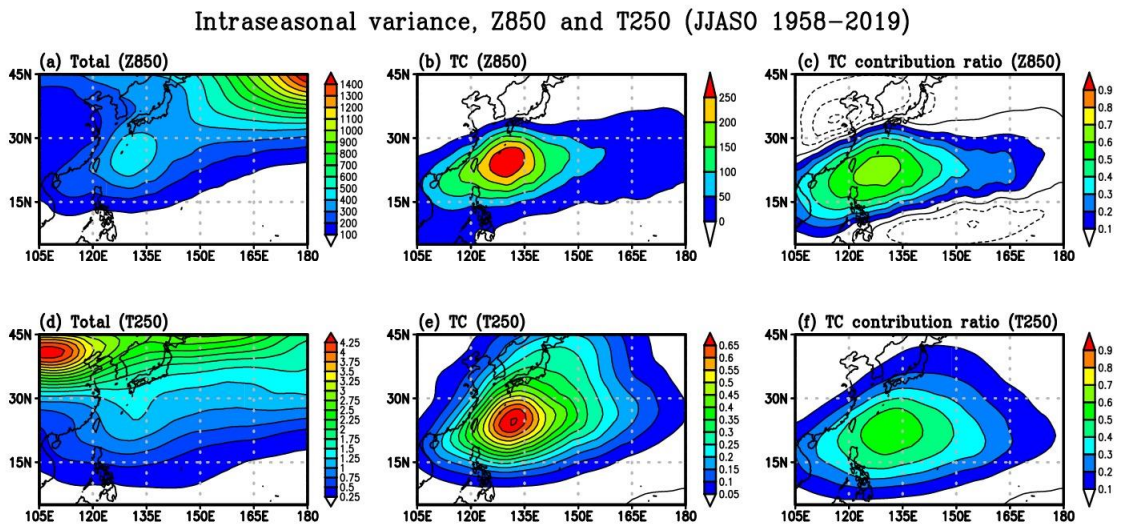

Fig. 4.17. (a–c) Intraseasonal (20–80 day) variance of 850-hPa geopotential height (in gpm^2), June–October 1958–2019: (a) Total field, (b) TC contribution, and (c) TC contribution ratio (dimensionless). The contour intervals in (b) and (c) are 50 gpm^2 and 0.1, respectively. (d–f) As in (a–c), respectively, but for temperature at 250 hPa (in K^2). The contour interval in (e) is 0.05 K^2.

本部分については、５年以内に雑誌等で刊行予定のため非公開。

As mentioned, in the TC-active area (15°N–30°N, 120°E–140°E), a substantial TC footprint can be seen in the intraseasonal variance. It can be inferred that the interannual variation of this variance is likely closely associated with the interannual variation in TC activity. Figure 4.24 is the interannual variation of the intraseasonal variance averaged over 15°N–30°N, 120°E–140°E. The intraseasonal variance in the total field fluctuates

considerably every year, with the maximum and minimum values of 2.02×10^{-10} and $0.59 \times 10^{-10}\ s^{-2}$ in 1968 and 2010, respectively (Fig. 4.24a). Moreover, as seen in the 9-year running mean, the intraseasonal variance between 1958 and 2019 fluctuates on the interdecadal scale and decreases with time. The Mann–Kendall nonparametric test (Kendall 1948) reveals that this decreasing trend is statistically significant at the 5% level. After the TC removal, the magnitude of the intraseasonal variance fluctuations decreases to a range between 0.32×10^{-10} and $0.73 \times 10^{-10}\ s^{-2}$ (a more than 3-fold reduction), and the interdecadal variation and decreasing trend disappear (Fig. 4.24b). The time series of the TC component exhibits almost the same fluctuation pattern with an equivalent amplitude in the total field (Fig. 4.24c). The correlation coefficient between the time series of the total field and the TC component is 0.95, whereas the correlation with the TC-removed time series is close to zero (0.03), indicating that the interannual and interdecadal variations in intraseasonal variance in the TC-active area coincide with the variations of TC activity. By contrast, the contribution of large-scale circulation systems to the variation is minimal. As the same as in the low-level relative vorticity, the correlation coefficients between the time series of the total field and TC component in the low-level geopotential height and upper-level temperature are also high (0.83 and 0.84, respectively; Figs. 4.25a,c and 4.26a,c). However, the correlations with the time series of the total and TC-removed fields are 0.53 (low-level geopotential height; Figs. 4.25a,b) and 0.78 (upper-level temperature; Figs. 4.26a,b), indicating that the fluctuations of the TC-removed fields averaged over 15°N–30°N, 120°E–140°E might not be negligible. The contrast may be explained as follows. First, vorticity is a variable that better reflects TC dynamics than inverted geopotential height and temperature fields, which exhibit a smoother and larger-scale pattern as shown in Figs. 4.2h,i. Secondly, the TC contribution to the fluctuations in vorticity occurs mainly along TC tracks and is much larger than the negative values within the averaged area (Figs. 4.27e,f; discussed later) because of the strong vortices associated with TCs. This contrast between positive and negative perturbations is less significant in the inverted geopotential height and temperature fields and therefore TC footprint is weaker in the area-averaged quantity.

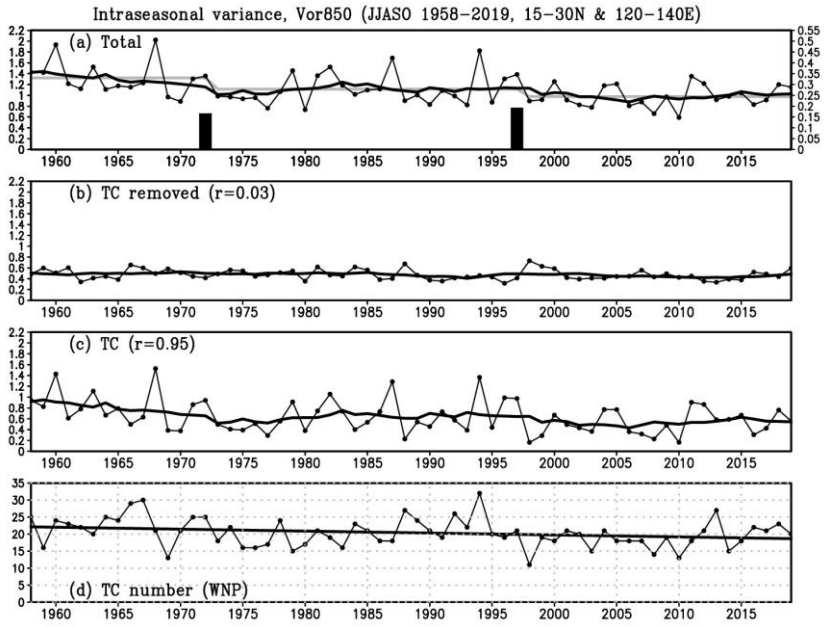

Fig. 4.24. Time series of the intraseasonal variance of 850-hPa relative vorticity averaged over the 15°N–30°N, 120°E–140°E area from June to October (thin black line, in 10^{-10} s^{-2}) and its 9-year running mean (thick black line): (a) Total field, (b) TC-removed field, and (c) TC contribution. The filled bar and thick gray line in (a) represent the regime shift index (*y*-axis at the right) and the time mean in each regime, respectively. (d) Time series of the number of TCs from June to October over the WNP (thin line) and the linear regression line derived through the least-squares method (think line). The linear decreasing trend (−0.57 per decade) is statistically significant at the 10% level by the Mann–Kendall nonparametric test.

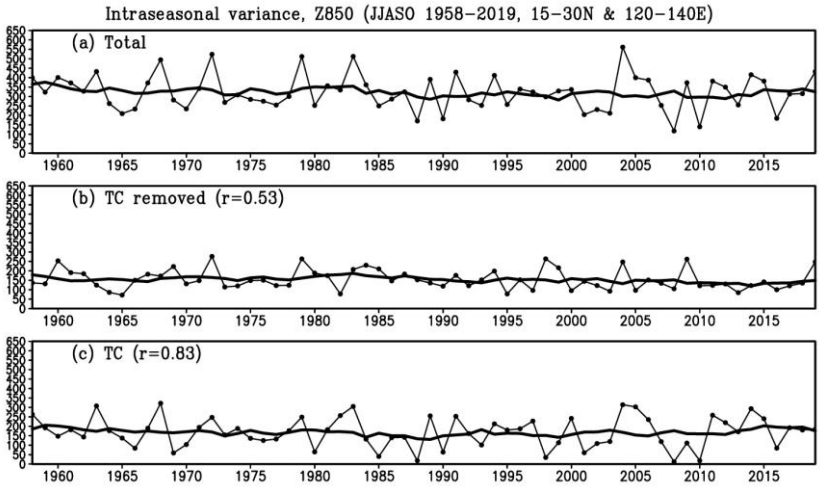

Fig. 4.25. As in Figs. 4.24a–c, respectively, but for 850-hPa geopotential height in gpm^2.

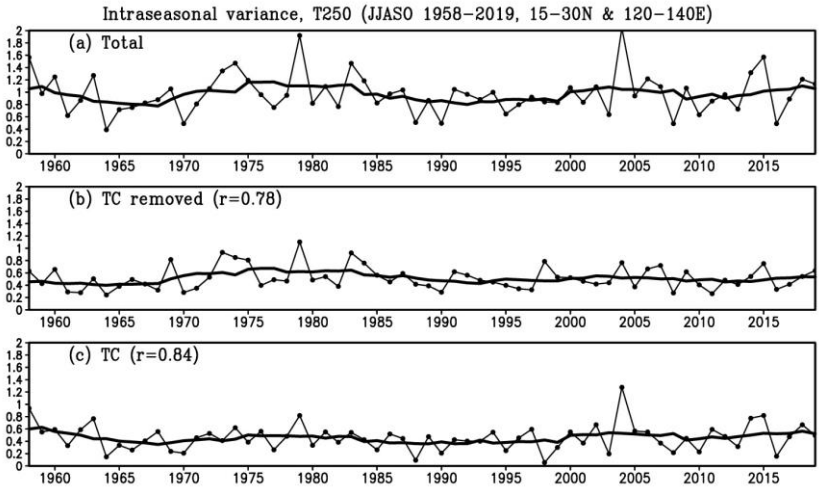

Fig. 4.26. As in Fig. 4.25, but for 250-hPa temperature in K^2.

The time series of intraseasonal variance also indicates regime shifts in the region. Shifts in 1972/1973 and 1997/1998 (marked in Fig. 4.24) are detected based on the approach used by Rodionov (2004). This finding is consistent with the regime shifts in TC activity reported in other studies, such as the event in the early 1970s (Matsuura et al. 2003; Liu and Chan 2013) and the late 1990s (Liu and Chan 2013; He et al. 2015; Hong et al. 2016; Zhao et al. 2018). To investigate the relationship between the changes in the intraseasonal variance of the total field and the TC contribution, the spatial distributions of the intraseasonal variance of low-level vorticity in different decades are constructed. From 1973 to 1997, the large variance region in the total field is widespread over the northwestern Philippine Sea and the northern SCS. From 1998 to 2019, the large variance is confined to a smaller area centered near 27°N, 127°E (Figs. 4.27a,c). The TC contribution domain is larger in 1973–1997 than in

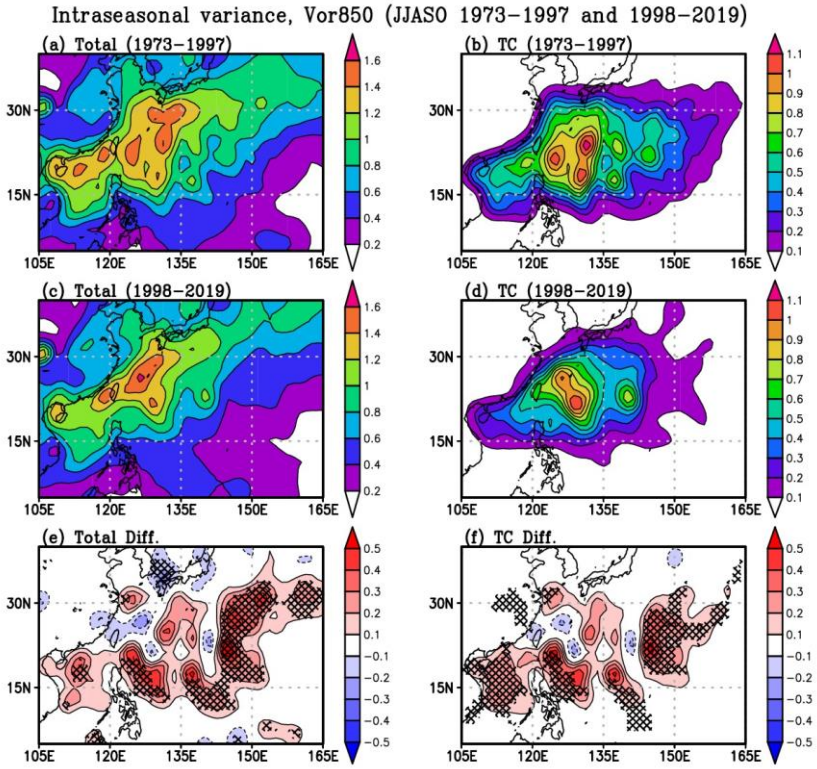

Fig. 4.27. Intraseasonal (20–80 day) variance of 850-hPa relative vorticity (10^{-10} s^{-2}). (a,b) Total field and TC component, June–October 1973–1997, respectively. (c,d) Total field and TC component, June–October 1998–2019, respectively. (e,f) Difference between the intraseasonal variance from 1998 to 2019 and from 1973 to 1997 in the total field and TC contribution, respectively. The cross-hatch areas in (e,f) indicate statistically significant at the 5% level by a two-sided Student's *t*-test.

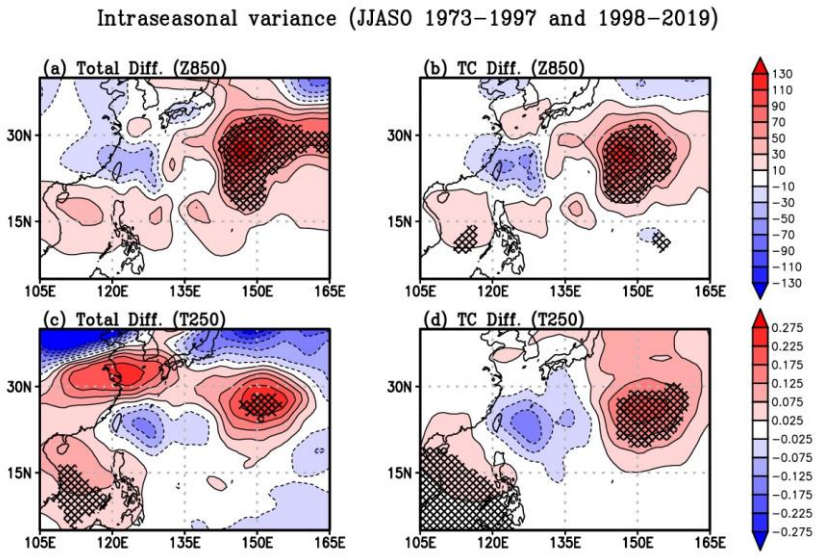

Fig. 4.28. (a,b) As in Figs. 4.27e,f, respectively, but for 850-hPa geopotential height (gpm^2). (c,d) As in (a,b), respectively, but for 250-hPa temperature (K^2).

The range at which to detect the TC perturbations in the TC removal was set as 1000 km. This radial length was somewhat arbitrary; therefore, the sensitivity of the results to the TC radius is tested. The vertical profiles of the TC contribution to the intraseasonal variance in the TC-active region (15°N–30°N, 120°E–140°E) for different radii are shown in Fig. 4.29. In the analysis over a 1000-km radius, a maximum TC contribution to the relative vorticity variance of more than 58% is observed at approximately 850 hPa and decreases with height. By contrast, the TC contribution to the temperature variance, which accounts for more than 50% of the total variance, increases with height, reaching its maximum at approximately 200 hPa. The heights of these maximum TC contributions correspond approximately to the heights of the maximum relative vorticity and warm cores in the basic TC structure, respectively. A comparison reveals that the smaller the detecting radius, the smaller the TC contribution. However, the sensitivity to the detection range is much smaller than the TC contribution itself. The TC contributions to the vorticity and temperature variances at the maximum contribution height are 56% and 46% when the radius is 800 km and 54% and 40% when it is 600 km, respectively. Although the contributions at all altitudes differ slightly with the detection radius, the profiles are consistent, and the degree of contribution is sufficiently large to confirm the substantial footprint of TCs in climate variability. Notably, the uncertainty of the TC contribution increases from 5% to 10% with the altitude, indicating that the detection domain must be carefully tested, particularly in the upper troposphere, where the relationship between negative PVA and TC is not as obvious as that in the lower troposphere.

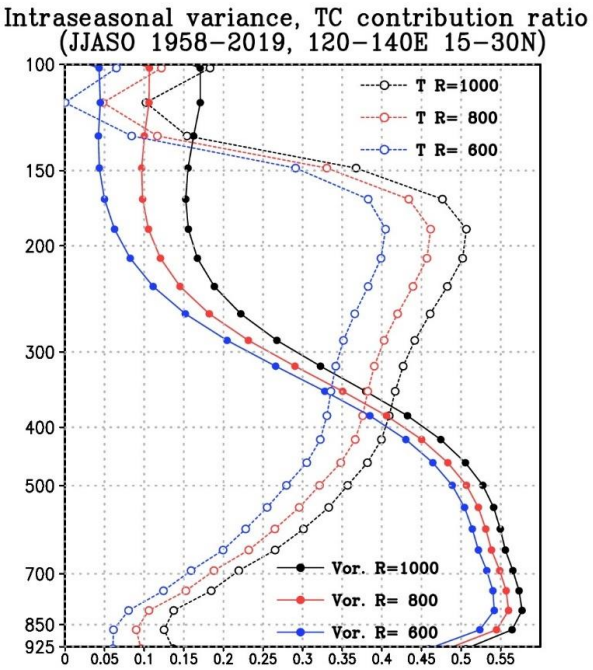

Fig. 4.29. Relationship between the TC contribution and height. The solid (dotted) line represents the TC contribution to relative vorticity (temperature). The blue, red, and black lines represent the estimated contribution with 600, 800, and 1000 km as the TC removal radius, respectively. The horizontal and vertical axes represent the contribution ratio and the pressure level in hPa, respectively.

While the asymmetry of PVA distribution associated with TC was considered in the PVA decomposition procedure in Chapter 3, the symmetric PVA was considered in this chapter (See Sections 3.2 and 4.2). As the same as the sensitivity of the TC contribution by the TC radius, the differences in the TC contribution to the seasonal mean and intraseasonal variance obtained when using different PVA decompositions are investigated. The TC contributions to the seasonal-mean fields during July–September 2004 are shown in Fig. 4.30, and the TC contributions to the intraseasonal (20–80-day) variances during July–September 2004 are shown in Fig. 4.31. The data of June and October 2004 are not used in the intraseasonal variances because the data contain a large edge effect by the Butterworth bandpass filter, and the data of June and October 2004 are also not used in the seasonal-mean fields for consistency with the intraseasonal variances.

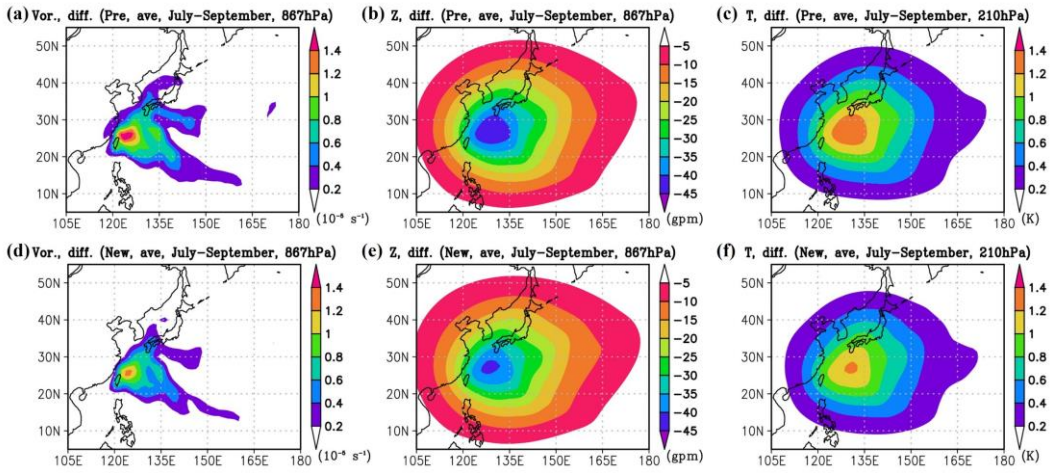

Fig. 4.30. TC contributions to the seasonal means in July–September 2004 obtained in Chapter 3 (upper panel) and Chapter 4 (lower panel). (a,d) Low-level vorticity in 10^{-5} s^{-1}, (b,e) low-level geopotential height in gpm, and (c,f) upper-level temperature in K.

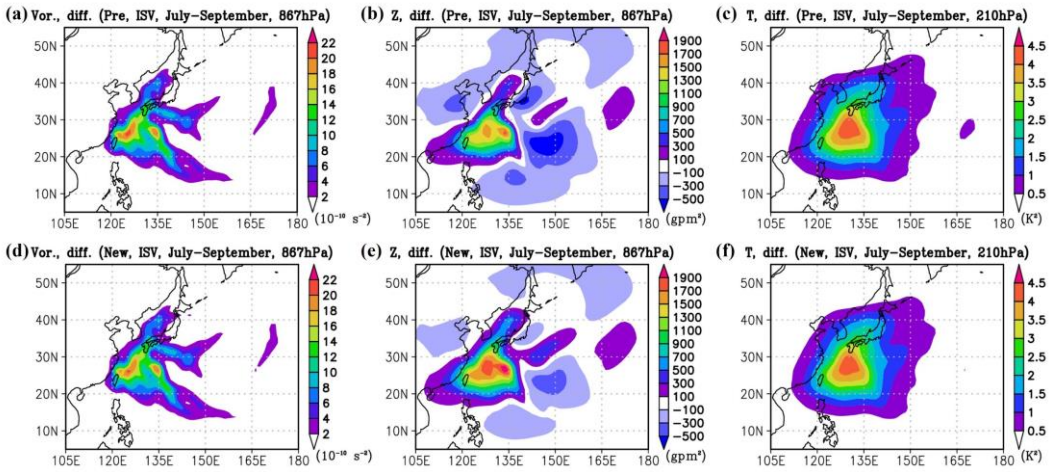

Fig. 4.31. TC contributions to the intraseasonal variances in July–September 2004 obtained in Chapter 3 (upper panel) and Chapter 4 (lower panel). (a,d) Low-level vorticity in 10^{-10} s^{-2}, (b,e) low-level geopotential height in gpm^2, and (c,f) upper-level temperature in K^2.

Compared with the PVA decomposition procedure modified in Chapter 4, a larger cyclonic PVA domain (up to 1200 km radius from the TC center) and a smaller anticyclonic PVA domain (800 km radius from the TC center) are determined in the PVA decomposition in Chapter 3. Therefore, the TC vortices calculated in Chapter 3 are more strongly represented than the TC vortices calculated in Chapter 4. However, the differences between the seasonal means in July–September 2004 are less than 10%, and the extents of the TC contributions do not change significantly (Fig. 4.30). Moreover, differences between the two PVA decompositions do not significantly affect the TC contributions to the intraseasonal variances in the low-level vorticity and upper-level temperature (Figs.

4.31a,c,d,f). On the other hand, although a difference of up to 10% can be seen in the low-level geopotential height, their spatial distributions are qualitatively the same (Figs. 4.31b,e).

4.3.4. Relationship between interannual variations in TC genesis and low-level vorticity fields

本部分については、５年以内に雑誌等で刊行予定のため非公開。

4.4. Discussion

In Subsection 4.3.1, the TC footprints in the climatological means during the 62-year typhoon season were investigated. The results showed a weakening low-level monsoon trough and an intensified low-level subtropical high when the TC footprints were not taken into account. The TC footprints were analyzed not only in the lower troposphere, but also in three dimensions from the surface to the lower stratosphere. This indicates that the TC footprints included in the observed long-term mean 3D circulation (e.g., the lower-tropospheric monsoon trough and subtropical high and the upper-level anticyclone and mid-Pacific trough) and in the corresponding warm core structure of the WNP summer monsoon system are crucial and notable. It has long been implicitly accepted that long-term averaging removes perturbations such as TCs, which fluctuate over a much shorter period than the averaging period. However, Hsu et al. (2008a) reported that the large perturbations of TCs could not be removed through averaging and left substantial footprints in the averaged field. Their findings were confirmed in this work, even though averaging over 62 years was performed. TC appears to be a crucial component in the WNP monsoon

system. Its existence influences the scales and locations of the subtropical high and monsoon trough conventionally regarded as the background state of high-frequency disturbances, such as TCs and tropical wave-like perturbations.

The TC contribution to the PJ pattern was analyzed in Subsection 4.3.2. The bipolar structure of the PJ pattern over the Philippine Sea and Japan was well observed in the EOF analysis. After the TC removal, the location and amplitude of the bipolar structure were changed. Moreover, the time series of convections associated with TC over the Philippine Sea and the principal component of the PJ pattern were moderately correlated. Therefore, it is possible that TC activity is related to the determination of the location and amplitude of the PJ pattern.

The propagations of the QBWO and boreal summer ISO (BSISO) were investigated in Subsection 4.3.3. After the TC removal, the westward propagation of QBWO occurred more rapidly ($4^\circ\ \mathrm{day}^{-1}$ versus $6^\circ\ \mathrm{day}^{-1}$). The analyzed QBWO characteristics of the northward propagation speed ($2^\circ\ \mathrm{day}^{-1}$) and westward propagation speed ($4^\circ\ \mathrm{day}^{-1}$) were consistent with results reported in previous studies (Yan et al. 2019; Li et al. 2020). Generally, the TC transition speed is slower than the westward propagation speed of QBWO. According to the RSMC-Tokyo best track data, the mean westward transition speed of TCs that move monotonically westward for more than 48 hours after their genesis for the period 1977–2019 is $3.3^\circ\ \mathrm{day}^{-1}$. The westward propagation of QBWO is perhaps dominated by the TC transition speed when TCs are present in the convective system. This is possibly why the westward propagation appears to be slower in the presence of TC signals. On the other hand, the phase speed of the northward propagation of BSISO were almost unchanged after the TC removal but a large reduction of its amplitude could be seen. This indicates that the TC signal is related to the northward propagation of BSISO. This suggests that TCs may facilitate the northward propagation of BSISO. On the other hand, in general, much more TC genesis is observed in the active phase of BSISO (Ko and Hsu 2009; Kikuchi 2021). Therefore, stronger signature of northward propagation may be expected in the active phase of BSISO, where many TCs are present. Although much more TC genesis is observed in the active phase of BSISO in general, it is worth discussing the possibility that much more TC genesis make an active phase of BSISO. If the northward propagation of BSISO is almost completely eliminated when the TC signals are removed, it would be possible to argue for the formation of an active phase of BSISO with a large number of TC genesis. However, the analysis results show a weakened northward propagation after the TC removal (Figs. 4.22a–c). Therefore, this cannot be strongly argued, although the possibility of an intensification of its northward propagation by many TCs cannot necessarily be ruled

out. For more detailed analysis, a composite analysis focusing on the phases of BSISO is considered necessary.

The sensitivity of the TC vortex to the PVA decomposition in the PPVI was examined. The strength of TC vortex derived by the PPVI differed depending on the PVA decomposition. The differences are considered as uncertainties. However, the differences in the results of climate field were not large, and the characteristics such as its distribution and the extent of the TC contribution were qualitatively the same. Galarneau and Davis (2013) decomposed the wind fields associated with a TC by removing relative vorticity and divergence anomalies circularly from the TC center. This suggests that the isotropic assumption of the PVA in the decomposition procedure in Chapter 4 could represent a certain degree of the TC characteristics. Therefore, although there are some uncertainties in the estimation of the TC contribution to the climate field, the TC removed dataset with the isotropic assumption of the PVA can be considered to estimate a certain degree of the TC contributions.

In Subsection 4.3.4, the relationship between the TC genesis location and the low-level relative vorticity field was investigated. The two peak TC genesis regions over the WNP in the TC active years corresponded to the enhancements of seasonal low-level relative vorticity over the peak regions; the enhancements could be explained as the divergence term enhancement in the vorticity equation. The divergence term enhancement over the western peak region was enhanced by only its TC-free component, while the enhancement over the eastern peak region was enhanced not only by its TC-free component but also by the TC component. This result suggests that a large number of TC genesis in the active years may have triggered subsequent TC genesis over the eastern peak region or the growth rate of TCs over the eastern region may be higher than TCs over the other region. The possibility of this TC-genesis positive feedback process, which might be related to the Rossby wave energy dispersion by a preexisting TC, is discussed in Chapter 5.

4.5. Conclusion

This work estimated the TC footprints in the climate mean state and multiscale variability over the WNP by comparing original reanalysis data (1958–2019) with data over the same period from which TC signals were removed. The removal was performed by subtracting the TC components, which were derived from the PPVI, from the reanalysis data. In this framework, the TC-removed data were dynamically balanced, which allows for the bulk assessment of the TC footprint in climate variability and exhibits significant potential utility for future climate

studies. This work revisited the issue of TC contribution raised in the studies by Hsu et al. (2008a,b), in which winds related to TCs at a single level only were removed and dynamic balance was not maintained. In contrast, this work retained this dynamic balance and removed multiple variables at all levels in the troposphere and lower stratosphere. This approach provided a more holistic view of TC footprints in climate mean state and variability.

Long-term mean fields over the WNP during the TC season between 1958 and 2019 were compared. Although the TCs were present for a much shorter period than the 62-year averaging period, TC footprints in the wind field, mass field, temperature field, and static stability could not be fully removed in the long-term mean fields. This suggests that even if TCs may appear in clusters because the modulating effect of large-scale flows is favorable to their genesis, the TC circulation of an extremely large amplitude can leave a distinct footprint in low-frequency, large-scale circulation, which is typically identified in the post-analysis through long-term averaging or low-pass filtering. As explained in Hsu et al. (2008a), this inseparability between the extremely-strong TC perturbations and the low-frequency large-scale flow was because the widely-adopted statistical procedure could not properly separate the signals of different time scales that actively interacted. The TC footprint in GPI defined by the long-term mean fields was also investigated. The result showed that the GPI is approximately 30% larger near Taiwan and smaller in another region of the WNP in the presence of TC footprints, but overall, no significant changes were observed. However, this result contains a large amount of uncertainty. The uncertainty of the influence of TCs on GPI is discussed in detail in Chapter 5.

This work demonstrated that although TCs tended to be more active when background flow was cyclonic, TCs left large cyclonic footprints in the background, and thus, the mean monsoon trough and the mean subtropical high appear to be stronger and weaker, respectively. Specifically, a larger footprint was observed in the years during which a large number of strong TCs occurred. This resulted in a much weaker subtropical high and a stronger monsoon trough than in the years during which a small number of strong TCs occurred. This contrast enhanced their interannual variance. According to the estimation described in this work, the TC contribution to the interannual variance exceeded 50% in the lower troposphere and decreased to 20% in the upper troposphere. In sum, when the TC footprint in the interannual variance was considered, the interannual variance of the monsoon trough appeared to be stronger and that of the western flank of subtropical high appeared to be weaker.

In relation to these interannual variabilities, the contribution of the TC signal to the PJ pattern was investigated. The bipolar structure of PJ pattern obtained from the seasonal-mean low-level relative vorticity

anomaly showed a distinct change in its position and amplitude when the TC signal was removed. Further analysis of the time series of TC activity and principal component of PJ pattern showed a moderate correlation. These results indicate that the interannual variabilities of TC activity and spatial structure of PJ pattern may be related.

The TC contribution to the intraseasonal variances of low-level vorticity, low-level geopotential height, and upper-level temperatures exceeded 50%, with a widespread positive TC contribution along prevailing TC tracks and the maximum located around the largest TC passing area. Notably, the intraseasonal variance also exhibited strong interannual fluctuations that were in turn embedded in an interdecadal fluctuation and a decreasing long-term trend and distinguished by regime shifts around 1972/1973 and in 1997/1998. After the TC removal, the interannual and interdecadal variations, regime shifts, and long-term trends of the intraseasonal variance became much weaker than before. This indicates the importance of TC footprints across multiple time scales—intraseasonal, seasonal, interannual, and interdecadal—and also in long-term trends.

Using low-level relative vorticity, the TC signals in the propagations of QBWO and BSISO over the WNP was investigated. In the TC-removed vorticity field, both amplitudes of northward propagations of QBWO and BSISO from 15°N to 35°N were largely reduced. Moreover, the westward propagation of QBWO in the TC-removed field was faster, indicating that the westward propagation became slower in the presence of TC footprints. This result suggests the possibility of TC footprints having significant contribution to the QBWO and BSISO propagations.

The relationship between the TC genesis location and the low-level relative vorticity field was investigated. Two peak regions of TC genesis were observed in the years when many TCs occurred. The enhancements of seasonal low-level relative vorticity over the two peak regions were also observed, indicating a close relationship between the TC genesis location and seasonal low-level relative vorticity distribution. The area-averaged magnitudes of seasonal low-level relative vorticity over the two peak regions were enhanced by the divergence term in the vorticity equation. However, over the western peak TC-genesis region, the vorticity was enhanced by only the non-TC component of the divergence term, while the enhancement over the eastern peak TC-genesis region was enhanced not only by its non-TC component but also by the TC component. This suggests that TC genesis may trigger subsequent TC genesis over the eastern peak region or the growth rate of TCs over the eastern region may be higher than TCs over the other region in the years when many TCs occurred.

Chapter 5. General conclusion

5.1. General discussion

As detailed in Chapter 2, numerical simulations revealed that TC Mora located over the BoB affected heavy rainfall over northern Taiwan by modulating frontal intensity. The enhanced front was caused by modulations of the upper-level trough and low-level synoptic-scale circulation. The modulated upper-level trough enhanced stronger downward northerly winds, which moved cooler airmass to northern Taiwan, whereas the modulated low-level synoptic-scale circulation enhanced southwesterly winds over the South China Sea, which transported warm/moist air to the Taiwan area. These enhancements promoted the enhancement of low-level convergence and confluence zone, resulting in the strong baroclinic zone, and thus, the heavy rainfall over Taiwan.

The modulation of low-level synoptic-scale circulation is observed when a TC exists. This modulation is a crucial mechanism leading to the PRE. In contrast, the upper-level trough modulation observed in the case study is not a common process in the PRE but is observed in the "downstream impact" during the extratropical transition, which has the potential to induce downstream high-impact weather (Archambault et al. 2013, 2015; Keller et al. 2019). Hirata and Kawamura (2013) reported that the BoB TCs in November had the potential to influence the East Asian weather system through the upper-level field modulation. In this case study, it was found that the BoB TC triggered a heavy rainfall event in East Asia through a similar mechanism reported by Hirata and Kawamura (2013). To the best of the author's knowledge, this case study is the first to report that a BoB TC helped trigger an extreme weather event in East Asia. This case study suggests that a proper representation and forecast of TC Mora and its remote impact in a model are necessary for well forecasting the heavy rainfall, in particular its timing and location. Furthermore, this case study implies that a frontal development might not be a purely local event and the consideration of the potential effect of a remote disturbance might be needed.

Moreover, TC Mora's intensity is weaker than the Category 1 TC in the Saffir–Simpson scale, meaning this TC was not strong. It was revealed that a weak TC over the BoB may be sufficient to influence the weather in East Asia. This suggests that the strength is likely not the major factor leading to the observed impact, however, the timing and favorable environment provided by the large-scale circulation may be more important. Interestingly, this is consistent with the fact that TCs entering the region ahead of the upper-level trough are favorable for the development of downstream cyclones and the size and intensity of TCs are secondary to the magnitude of the

downstream impact (Archambault et al. 2013). However, the reported downstream development occurred over the ocean, whereas the modulation of the upper-level circulation in the case occurred over land. Whether the remote effect of a TC over the BoB on the heavy rainfall in East Asia is a common process requires further investigation. If it is a common process, investigating the relationship between a TC located over the BoB and rainfall in East Asia using numerical models, specifically focusing on the relationship between the TC and environmental fields and topographic effect, is as valuable as the downstream impact studies.

In Chapter 3, a dataset from which TC vortices in 2004 summer season were removed was constructed to investigate the TC footprint in climate by comparing the analyses with the original and TC-removed datasets. Although there are some methods to decompose the wind field into TC and non-TC components, the PV inversion was employed to reconstruct not only the wind field, but also the mass and temperature fields in terms of dynamic balance. Compared with the TC-removed fields by the existing methods, which resulted in the unrealistic or over-removed vorticity fields, the TC-removed vorticity field by the PV inversion was reasonable. This was because the introduced PV decomposition into TC and non-TC components was proper. In addition, the effects of anticyclonic PVA in the upper troposphere and lower stratosphere, which were characteristic of the PV structure in TC, were investigated. Although many TC studies using the PV inversion did not consider the TC-induced anticyclonic PVA effects, the results demonstrate that the anticyclonic PVA had a significant effect on the upper-level temperature. Thus, the effect of anticyclonic PVA must be considered in TC studies.

The TC footprints in the intraseasonal variability and seasonal mean field over the tropical WNP were evaluated. The results obtained by the proposed method confirmed the significant TC footprints in the intraseasonal variability and seasonal-mean field as demonstrated in Hsu et al. (2008b). The strong northward intraseasonal variability signal was also significantly weaker after the TC footprint removal. The TC contributions obtained by the PV inversion were consistent with the results by Hsu et al. (2008b) but showed larger contributions. This is because their TC removal method underestimated the TC vortices, whereas the proposed PV inversion evaluates them appropriately.

In Chapter 4, although the TC-removed data only for 2004 were constructed in Chapter 3, TC-removed data from 1958 to 2019 were constructed to estimate the TC footprint in the climate mean state and multiscale variability over the WNP. Although this study revisits the TC footprint issue raised by Hsu et al. (2008a,b), the analysis provides a more holistic view of the TC footprints in the climate mean state and variability at all levels. It

was found that TCs left their significant footprint in multiple (intraseasonal, seasonal, interannual, and interdecadal) time-scale fields and also on long-term trends. Remarkably, this study revealed that TC signals left a large footprint in the propagations of QBWO and BSISO. Although the BSISO has long been considered a key element of TC genesis over the WNP (Yoshida et al. 2014; Kikuchi 2021), the results suggest the possibility that TC signals over the WNP may be an important component of BSISO propagation. The TC footprint to the PJ pattern was also large: After the TC removal, the location and amplitude of the PJ pattern were changed. As reported by Seiki et al. (2021), the BSISO and PJ pattern are closely linked. Therefore, it is not surprising that the large TC footprint is detected in the PJ pattern as well as in the BSISO.

Because of the substantial TC footprints in the long-term climate, TCs distinctly modified mean circulation patterns over the WNP from conditions with a strong subtropical high and a weak monsoon trough to those with a weaker subtropical high and a stronger monsoon trough. In addition, these variabilities were considerably greater than the variabilities in the TC-removed data. The results indicate that, in terms of the characteristics of the monsoon trough in the long-term mean state, TC signals should be regarded as a crucial element in the WNP monsoon system rather than just as extreme weather events modulated by large-scale environmental flows. The long-term dataset provides an opportunity to study the interaction between TC and TC-free large-scale circulation to advance the understanding of climate variability over the WNP.

The climatological TC-free low-level vorticity fields in the years in which many TCs occurred were analyzed. In a particular region (10°N–22.5°N, 142.5°E–160°E), the number of TC genesis increased, and the low-level vorticity was enhanced by the TC-free circulation and TC activities. This suggests that the TC activity may trigger subsequent TC genesis over the region or the growth rate of the TCs over the region may be higher than TCs in other regions in the years when many TC occurred, although the mechanism of enhancement of low-level vorticity is still unclear. Interestingly, this region roughly corresponds to the region of TC genesis induced by the Rossby wave energy dispersion by a preexisting TC. The mechanism of TC genesis induced by the preexisting TC is as follows: mature TCs disperse their energy, resulting in the Rossby wave trains in the southeast direction. A new TC sometimes occurs in the low-pressure region in the wave train (Li and Fu 2006; Yoshida and Ishikawa 2013). Fudeyasu et al. (2020) reported that most TCs that emerged via Rossby wave energy dispersion, which reached tropical cyclone strength after the development, over the WNP from 2009 to 2017 occurred east of 140°E, and the averaged genesis position of such TCs was 11.2°N, 153.7°E. The TC genesis region induced by the Rossby

wave energy dispersion corresponds to the region, in which the low-level vorticity is enhanced by TC activity, and thus, the Rossby wave energy dispersion by preexisting TC is the possible mechanism enhancing the low-level vorticity in the region. The possibility of the low-level vorticity enhancement due to preexisting TCs would increase if it can be confirmed that the increase of TC genesis induced by the preexisting TCs in years when many TCs occur is analyzed. Moreover, if spatial or temporal filtered TC-removed data is employed in such analysis using a budget equation, the TC contribution could not be adequately estimated because TC components cannot be completely decomposed from the total fields with such filtering schemes. A dynamically balanced TC-removed dataset is necessary to correctly estimate the TC contribution. From this standpoint, the TC-removed dataset constructed in this study is very useful.

It should be noted that while the TC-removed dataset is more useful than data constructed by other filtering schemes in terms of dynamic balance, the result is not completely dynamically balanced. The streamfunction, geopotential, and virtual temperature are balanced in the PV inversion system, whereas the velocity potential and vertical pressure velocity are balanced by the continuity equation. There is also a balanced relationship between the streamfunction and the velocity potential (e.g., vorticity equation or divergence equation), but this was not considered in this study. The low-level inflow and upper-level outflow are characteristics of TCs, and the upper-level outflow is considered to induce an upper-level inflow and subsidence elsewhere due to dynamic compensation. However, this compensation cannot be represented in the TC-removed dataset. An improved PV inversion system in which the velocity potential and vertical velocity are directly included would presumably produce new TC-removed data that better represent the inflow and compensated subsidence.

As mentioned in Section 1.3, the TC-removed data is constructed by removing dynamically balanced vortex structures from the 6-hourly reanalysis data in this study. On the other hand, the remote effect induced by TC vortex is not removed. We can understand the TC footprint in climate by analyzing the TC-removed data. However, the remote TC effect and cause-and-effect relationship between TC and climate cannot be understood directly. Numerical experiments are the way to understand them. For the experiments, the TC-removed data can be used for constructing an initial condition and a forcing data. For example, as shown in Chapter 2, the remote TC effect could be discussed from the difference in the evolution of the large-scale field in presence and absence of TC in the initial conditions given to the atmospheric model. The diabatic heating induced by TCs is very large and is expected to affect the large-scale field. The diabatic heating induced by TCs can be estimated by calculating the

diabatic heating from the original data and the TC-removed data, and by taking the difference. Using a linear baroclinic model and the calculated diabatic heating induced by TCs as a forcing, a steady-state linear response can be obtained. Another advantage of the TC-removed data is that it provides information of the instantaneous environmental field when TC exists. For example, the Statistical Hurricane Intensity Prediction Scheme (SHIPS; DeMaria and Kaplan 1994, 1999; DeMaria et al. 2005; Shimada et al. 2018), which is a statistical model used by many forecasting agencies to predict TC intensity, but it requires information on several environmental fields in addition to the instantaneous TC intensity. Moreover, the TC steering flow is defined as the wind direction of the instantaneous vertically-weighted averaged environmental flow. In such case, horizontal smoothing or spatial averaging are used to obtain the environmental field information, but it is unclear whether the contributions of TC vortex are sufficiently removed by these methods. The TC-removed data provides environmental field information with the contributions of TC vortex removed. Such data may improve the accuracy of intensity prediction using SHIPS, and steering flow. These issues will be investigated in the future.

The present findings have significant implications for GCM performance evaluations. Considering the considerable TC footprints in climate means and variabilities, GCMs that cannot properly simulate TCs (e.g., low-resolution GCMs) would exhibit a much weaker monsoon trough and a much stronger western flank of subtropical high as well as substantially less climate variability over the WNP. If such models show means and variabilities with amplitudes that are equivalent to those observed in the real world, other climate processes would likely behave unrealistically to compensate for the would-be underestimation. Most state-of-the-art GCMs used in climate projections, such as CMIP5 and CMIP6, are relatively low-resolution and are therefore not capable of properly simulating TC circulation and activity. Hypothetically, such models would tend to under-simulate the mean summer circulation and variability over the WNP both in the present and the future, leading to improper estimations of changes caused by global warming. Further studies evaluating the validity of this hypothesis are needed. In view of the substantial contributions of TCs, high-resolution models that realistically simulate TC activity would be better able to reliably project future climate changes in circulation and precipitation over the WNP; these models would also have a higher chance to narrow down the projection uncertainty. Moreover, Knutson et al. (2020) reported that, in the comparison of TC activity projections responding to global warming in climate models, some of the projections were robust in the models (e.g., increases of global TC intensity and precipitation), while some were in lower confidence levels (e.g., a decrease of global TC frequency and an increase of global very intense TC frequency). It was also reported that some GCMs are better than others at producing

realistic TCs (Camargo and Wing 2016). Analyzing the models that adequately simulate TCs may help reduce the uncertainty of the projections with large inter-model differences.

Another issue is the influence of satellite observation after the late 1970s. Data from 1980 to 2019 were analyzed, and the results were compared with those presented in this study. The estimated TC footprints in 1980–2019 were essentially the same as those in 1958–2019 except for a difference in approximately 10% in the interannual variance of low-level geopotential and upper-level temperature. The relatively minimal differences suggest the reliability of the results.

5.2. Implications for future works

Horizontal resolution may be an important consideration for this type of study. Although TCs in the JRA-55 reanalysis show better representation compared with TCs in other reanalysis data (see Section 4.2), the 1.25° horizontal resolution is not high enough to represent actual TC intensity and structure, specifically for strong TCs. The resolution dependence of TC footprint was explored in Hsu et al. (2008a) by comparing reanalysis data with different resolutions. They concluded that the higher resolution data revealed the TC footprint pattern in greater detail (in both distribution pattern and amplitude) but yielded essentially the same results as in the lower resolution data. It follows that the higher resolution data are expected to reveal an even higher contribution from TCs than the 50%–70% identified in the study. While this resolution issue deserves the following study, the large TC footprint identified in this study, although likely underestimated, is of a big concern for the climate variability study. To clearly show the TC footprint in different horizontal resolutions, TC-removed data with different resolutions need to be constructed. Moreover, the reanalysis used in this study was JRA-55 only. Different representations of TC in different reanalyses would lead to different TC footprints. To understand an uncertainty of the footprints, TC-removed data with multiple reanalyses also need to be constructed. Furthermore, as stated above, the effect of anticyclonic PVA associated with TC must be considered in TC studies in terms of better representation of warm core. Because the distribution of TC-related anticyclonic PVAs is highly asymmetric, the circular domain for the anticyclonic PVAs removal would not be proper. Therefore, it is expected that when the TC-removed data are constructed with different resolutions and different reanalyses in future studies, the TC-related anticyclonic PVAs are identified using more sophisticated partitioning techniques.

TCs likely leave marked footprints in climate variability also in other regions in which they are active,

such as the tropical North Atlantic, the northern Indian Ocean, and the tropical western South Pacific. The extent of the footprints is likely to depend on the mean state. For example, they are presumably smaller over the tropical North Atlantic because of the dominance of the subtropical high and the absence of a monsoon trough in that region. Future studies focusing on other basins are warranted to deepen our understanding of the relative contributions of TCs to the mean state and variability of the climate. Furthermore, TCs targeted for removal in this study were those with a maximum sustained wind speed of 34 kt or higher. Most tropical depressions dissipated, and less than half reached TC strength after development during June–October 2009–2017 (Fudeyasu et al. 2020). Although individual tropical depressions are weak vortices, their clustered contribution to large scale field is expected not to be negligible due to a large number of them, for example, heat uptake near the equator. The tropical depression contribution to the large-scale field is probably investigated by comparing two TC-removed datasets, in which the tropical depressions are retained and removed.

Although the GPI around Taiwan is approximately 30% larger in the presence of TC footprints, the TC footprints in the moisture field and potential intensity factors were likely underestimated. First, moisture was removed by a spatial filter. Second, although the potential intensity is sensitive to SST, it remained almost unchanged after the computation of potential intensity with TC-removed data because the TC contribution to SST could not be estimated with the current TC removal scheme. The estimations of dynamically-based changes of moisture field and SST when TCs are removed would result in larger contributions. Because the current TC removal scheme does not support the removals of moisture and SST anomalies, it is needed to estimate the TC contributions to the moisture field and SST that numerical models or a new removal scheme in which the air-sea fluxes are considered.

Studies have suggested that under global warming conditions, TCs decrease in number, but increase in strength (Sugi et al. 2002; Camargo 2013; Yamada et al. 2017), and TC translation speed slows down (Kossin 2018). In regions where TCs are active, the reduction in the number of TCs would result in smaller multiscale variability, whereas the increase in strong TCs and the deceleration of TC translation speed would result in larger variability. Moreover, TC genesis locations shift to the east due to the eastward monsoon trough extension (Yokoi et al. 2012; Wang and Wu 2018) and TC tracks migrate poleward (Knutson et al. 2019, 2020; Kossin et al. 2014, 2016) under future climate conditions. This implies that the distance between the TC genesis location and the TC recurvature location will increase. Coupled with the deceleration of TC transition speed, these changes would result

in enhanced TC footprint in the climate means and variabilities and shift the distributions of TC footprint to the northeast. Additional detailed diagnostics on the relative contribution from the various changes related to TCs are required to yield more reliable estimations of TC footprints under the conditions.

In recent years, numerous studies on the multiscale nature of circulation over the tropical WNP have been conducted, specifically concerning energetics (e.g., Hsu et al. 2011; Ko et al. 2012). Using data decomposed into various time scales, the studies estimated the energy conversion among fluctuations at different time scales. Although decomposition of the dynamic fields is one way to consider the TC contribution to energetics, temporal filtering cannot fully decompose the fields into TC and non-TC components as discussed above. Using TC-removed fields to reveal the TC contribution to energetics is the preferred approach. Based on the existing TC removal method, Ko et al. (2012) revealed that the kinetic energy conversion between submonthly and intraseasonal perturbations was 40%–50% larger when TC vortices are present in the analyzed dataset. Hsu et al. (2008b) and Ko et al. (2012) analyzed the TC contributions at the 850 hPa level due to the limitations of the existing TC removal method; therefore, they could not reveal the complete characteristics of energy conversion in three dimensions. Furthermore, considering the larger TC amplitude derived from the proposed TC removal method, Ko et al. (2012) might have underestimated the TC contribution. Both TC and TC-removed fields obtained by the proposed removal technique enable analysis at all layers while retaining dynamic balance. In addition to the vorticity budget demonstrated in this study, diagnostics based on such data are expected to obtain a more accurate estimation of energy conversion and dynamical processes involved in the multiscale interaction.

5.3. Concluding remarks

This study revealed a downstream impact of a BoB TC on East Asian extreme weather and TC footprints in climate fields over the WNP. Many previous studies have investigated the mechanism of downstream impact, but most have analyzed such events that occurred over ocean basins. In this study, the downstream impact caused by the modulation of the upper-level field, which was analyzed in previous studies, was also observed over the continent from the BoB to East Asia. Moreover, it was found to have induced extreme weather over the region. Thus, this study revealed that TCs over the BoB had the potential to excite severe weather over East Asia.

Several previous studies have pointed out that climate fields calculated by long-term time averaging or low-pass filtering include non-negligible TC footprints. In this study, various TC footprints in climate fields were

investigated using unique long-term data with TC vortices removed from the reanalysis data. The results showed that TCs had a large footprint in climate fields at various timescales and supported the findings obtained in previous studies. Remarkably, while BSISO characteristics have been considered as important environmental factors for TC genesis, this study pointed out the possibility of a large TC footprint in BSISO propagation over the WNP. The TC-removed data used in this study should be useful to understand the potential TC impact on climate fields and investigate the relationship between climate fields and TCs.

References

Arakane, S., and Coauthors, 2019: Remote effect of a tropical cyclone in the Bay of Bengal on a heavy-rainfall event in subtropical East Asia. npj Clim. Atmos. Sci., 2, 25, https://doi.org/10.1038/s41612-019-0082-8.

——, and H.-H. Hsu, 2020: A tropical cyclone removal technique based on potential vorticity inversion to better quantify tropical cyclone contribution to the background circulation. Climate Dyn., 54, 3201–3226, https://doi.org/10.1007/s00382-020-05165-x.

——, and ——, 2021: Tropical cyclone footprints in long-term mean state and multiscale climate variability in the western North Pacific as seen in the JRA-55 reanalysis. J. Climate, 34, 7443–7460, https://doi.org/10.1175/JCLI-D-20-0887.1.

Arakawa, A., and W. H. Schubert, 1974: Interaction of a cumulus cloud ensemble with the large-scale environment, Part I. J. Atmos. Sci., 31, 674–701, https://doi.org/10.1175/1520-0469(1974)031<0674:IOACCE>2.0.CO;2.

Archambault, H. M., L. F. Bosart, D. Keyser, and J. M. Cordeira, 2013: A climatological analysis of the extratropical flow response to recurving western North Pacific tropical cyclones. Mon. Wea. Rev., 141, 2325–2346, https://doi.org/10.1175/MWR-D-12-00257.1.

——, D. Keyser, L. F. Bosart, C. A. Davis, and J. M. Cordeira, 2015: A composite perspective of the extratropical flow response to recurving western North Pacific tropical cyclones. Mon. Wea. Rev., 143, 1122–1141, https://doi.org/10.1175/MWR-D-14-00270.1.

Bessho, K., and Coauthors, 2016: An introduction to Himawari8/9–Japan's new-generation geostationary meteorological satellites. J. Meteor. Soc. Japan, 94, 151–183, https://doi.org/10.2151/jmsj.2016-009.

Bishop, C. H., and A. J. Thorpe, 1994: Potential vorticity and the electrostatic analogy: Quasi-geostrophic theory. Quart. J. Roy. Meteor. Soc., 120, 713–731, https://doi.org/10.1002/qj.49712051710.

Bister, M., and K. A. Emanuel, 2002: Low frequency variability of tropical cyclone potential intensity. 1. Interannual to interdecadal variability. J. Geophys. Res., 107, 4801, https://doi.org/10.1029/2001JD000776.

Brennan, M. J., G. M. Lackmann, and K. M. Mahoney, 2008: Potential vorticity (PV) thinking in operations: The utility of nonconservation. Wea. Forecasting, 23, 168–182, https://doi.org/10.1175/2007WAF2006044.1.

Camargo, S. J., 2013: Global and regional aspects of tropical cyclone activity in the CMIP5 models. J. Climate, 26,

9880–9902, https://doi.org/10.1175/JCLI-D-12-00549.1.

——, K. A. Emanuel, and A. H. Sobel, 2007: Use of a genesis potential index to diagnose ENSO effects on tropical cyclone genesis. J. Climate, 20, 4819–4834, https://doi.org/10.1175/JCLI4282.1.

——, and A. A. Wing, 2016: Tropical cyclones in climate models. Wiley Interdiscip. Rev.: Climate Change, 7, 211–237, https://doi.org/10.1002/wcc.373.

Cha, D.-H., and Y. Wang, 2013: A dynamical initialization scheme for real-time forecasts of tropical cyclones using the WRF model. Mon. Wea. Rev., 141, 964–986, https://doi.org/10.1175/MWR-D-12-00077.1.

Chang, C.-W. J., S.-Y. S. Wang, and H.-H. Hsu, 2016: Changes in tropical cyclone activity offset the ocean surface warming in northwest Pacific: 1981–2014. Atmos. Sci. Lett., 17, 251–257, https://doi.org/10.1002/asl.651.

Chen, C.-S., and Y.-L. Chen, 2003: The rainfall characteristics of Taiwan. Mon. Wea. Rev., 131, 1323–1341, https://doi.org/10.1175/1520-0493(2003)131<1323:TRCOT>2.0.CO;2.

Chen, G. T.-J., 1992: Mesoscale features observed in the Taiwan Mei-Yu season. J. Meteor. Soc. Japan, 70, 497–516, https://doi.org/10.2151/jmsj1965.70.1B_497.

——, 2005: Characteristics of low-level jets over northern Taiwan in Mei-Yu season and their relationship to heavy rain events. Mon. Wea. Rev., 133, 20–43, https://doi.org/:10.1175/MWR-2813.1.

——, and C.-P. Chang, 1980: The structure and vorticity budget of an early summer monsoon trough (Mei-Yu) over southeastern China and Japan. Mon. Wea. Rev., 108, 942–953, https://doi.org/10.1175/1520-0493(1980)108<0942:TSAVBO>2.0.CO;2.

——, and C.-C. Yu, 1988: Study of low-level jet and extremely heavy rainfall over northern Taiwan in the Mei-Yu season. Mon. Wea. Rev., 116, 884–891, https://doi.org/10.1175/1520-0493(1988)116<0884:SOLLJA>2.0.CO;2.

——, C.-C. Wang, and L.-F. Lin, 2006: A diagnostic study of a retreating Mei-Yu front and the accompanying low-level jet formation and intensification. Mon. Wea. Rev., 134, 874–896, https://doi.org/10.1175/MWR3099.1.

Chen, J.-H., and S.-J. Lin, 2013: Seasonal predictions of tropical cyclones using a 25-km-resolution general circulation model. J. Climate, 26, 380–398, https://doi.org/10.1175/JCLI-D-12-00061.1.

Cheung, K. K. W., and J. C. L. Chan, 1999: Ensemble forecasting of tropical cyclone motion using a barotropic model. Part I: Perturbations of the environment. Mon. Wea. Rev., 127, 1229–1243, https://doi.org/10.1175/1520-0493(1999)127<1229:EFOTCM>2.0.CO;2.

Cote, M. R., 2007: Predecessor rain events in advance of tropical cyclones. M.S. thesis, Department of Atmospheric and Environmental Sciences, University at Albany, State University of New York, 200 pp. [Available online at http://cstar.cestm.albany.edu/CAP_Projects/Project10/index.htm.]

Davis, C. A., and K. A. Emanuel, 1991: Potential vorticity diagnostics of cyclogenesis. Mon. Wea. Rev., 119, 1929–1953, https://doi.org/10.1175/1520-0493(1991)119<1929:PVDOC>2.0.CO;2.

DeMaria, M., 1996: The effect of vertical shear on tropical cyclone intensity change. J. Atmos. Sci., 53, 2076–2088, https://doi.org/10.1175/1520-0469(1996)053<2076:TEOVSO>2.0.CO;2.

——, and J. Kaplan, 1994: A Statistical Hurricane Intensity Prediction Scheme (SHIPS) for the Atlantic basin. Wea. Forecasting, 9, 209–220, https://doi.org/10.1175/1520-0434(1994)009<0209:ASHIPS>2.0.CO;2.

——, and ——, 1999: An updated Statistical Hurricane Intensity Prediction Scheme (SHIPS) for the Atlantic and eastern North Pacific basins. Wea. Forecasting, 14, 326–337, https://doi.org/10.1175/1520-0434(1999)014<0326:AUSHIP>2.0.CO;2.

——, M. Mainelli, L. K. Shay, J. A. Knaff, and J. Kaplan, 2005: Further improvements to the Statistical Hurricane Intensity Prediction Scheme (SHIPS). Wea. Forecasting, 20, 531–543, https://doi.org/10.1175/WAF862.1.

Emanuel, K. A., 1986: An air-sea interaction theory for tropical cyclones. Part I: Steady-state maintenance. J. Atmos. Sci., 43, 585–604, https://doi.org/10.1175/1520-0469(1986)043<0585:AASITF>2.0.CO;2.

——, 2001: Contribution of tropical cyclones to meridional heat transport by the oceans. J. Geophys. Res., 106, 14771–14782, https://doi.org/10.1029/2000JD900641.

——, and D. S. Nolan, 2004: Tropical cyclone activity and global climate system. Preprints, 26th Conference on Hurricanes and Tropical Meteorology, Miami, FL, Amer. Meteor. Soc., 240–241.

Evans, C., and Coauthors, 2017: The extratropical transition of tropical cyclones. Part I: Cyclone evolution and direct impacts. Mon. Wea. Rev., 145, 4317–4344, https://doi.org/10.1175/MWR-D-17-0027.1.

Feng, T., X. Yang, X. Sun, D. Yang, and C. Chu, 2020: Reexamination of the climatology and variability of the

northwest Pacific monsoon trough using a daily index. J. Climate, 33, 5919–5938, https://doi.org/10.1175/JCLI-D-19-0459.1.

Franklin, J. L., S. E. Feuer, J. Kaplan, and S. D. Aberson, 1996: Tropical cyclone motion and surrounding flow relationships: Searching for beta gyres in omega dropwindsonde datasets. Mon. Wea. Rev., 124, 64–84, https://doi.org/10.1175/1520-0493(1996)124<0064:TCMASF>2.0.CO;2.

Fudeyasu, H., and Coauthors, 2020: Development conditions for tropical storms over the western North Pacific stratified by large-scale flow patterns. J. Meteor. Soc. Japan, 98, 61–72, https://doi.org/10.2151/jmsj.2020-004.

Galarneau, T. J., Jr., L. F. Bosart, and R. S. Schumacher, 2010: Predecessor rain events ahead of tropical cyclones. Mon. Wea. Rev., 138, 3272–3297, https://doi.org/10.1175/2010MWR3243.1.

——, and C. A. Davis, 2013: Diagnosing forecast errors in tropical cyclone motion. Mon. Wea. Rev., 141, 405–430, https://doi.org/10.1175/MWR-D-12-00071.1.

Gong, C.-Y., and Coauthors, 2015: The rank of extreme rainfall events over Taiwan (in Chinese). National Science and Technology Center for Disaster Reduction (available at https://watch.ncdr.nat.gov.tw/watch_ebook.aspx).

Grams, C. M., and Coauthors, 2013a: The impact of Typhoon Jangmi (2008) on the midlatitude flow. Part I: Upper-level ridgebuilding and modification of the jet. Quart. J. Roy. Meteor. Soc., 139, 2148–2164, https://doi.org/10.1002/qj.2091.

——, S. C. Jones, and C. A. Davis, 2013b: The impact of Typhoon Jangmi (2008) on the midlatitude flow. Part II: Downstream evolution. Quart. J. Roy. Meteor. Soc., 139, 2165–2180, https://doi.org/10.1002/qj.2119.

——, and S. R. Blumer, 2015: European high-impact weather caused by the downstream response to the extratropical transition of North Atlantic Hurricane Katia (2011). Geophys. Res. Lett., 42, 8738–8748, https://doi.org/10.1002/2015GL066253.

——, and H. M. Archambault, 2016: The key role of diabatic outflow in amplifying the midlatitude flow: A representative case study of weather systems surrounding western North Pacific extratropical transition. Mon., Wea., Rev., 144, 3847–3869, https://doi.org/10.1175/MWR-D-15-0419.1.

Gray, W. M., 1975: Tropical Cyclone Genesis. Dept. of Atmospheric Science Paper, 234, Colorado State University, Fort Collins, CO, 121 pp.

——, 1998: The formation of tropical cyclones. Meteor. Atmos. Phys., 67, 37–69, https://doi.org/10.1007/BF01277501.

Hakim, G. J., D. Keyser, and L. F. Bosart, 1996: The Ohio valley wave-merger cyclogenesis event of 25–26 January 1978. Part II: Diagnosis using quasigeostrophic potential vorticity inversion. Mon. Wea. Rev., 124, 2176–2205, https://doi.org/10.1175/1520-0493(1996)124<2176:TOVWMC>2.0.CO;2.

Han, J., and H.-L. Pan, 2011: Revision of convection and vertical diffusion schemes in the NCEP Global Forecast System. Wea. Forecasting, 26, 520–533, https://doi.org/10.1175/WAF-D-10-05038.1.

Harada, Y., and Coauthors, 2016: The JRA-55 reanalysis: Representation of atmospheric circulation and climate variability. J. Meteor. Soc. Japan, 94, 269–302, https://doi.org/10.2151/jmsj.2016-015.

Hart, R. E., 2011: An inverse relationship between aggregate northern hemisphere tropical cyclone activity and subsequent winter climate. Geophys. Res. Lett., 38, L01705, https://doi.org/10.1029/2010GL045612.

Haynes, P., and M. McIntyre, 1987: On the evolution of vorticity and potential vorticity in the presence of diabatic heating and frictional or other forces. J. Atmos. Sci., 44, 828–841, https://doi.org/10.1175/1520-0469(1987)044<0828:OTEOVA>2.0.CO;2.

Hazelton, A. T., L. Harris, and S.-J. Lin, 2018: Evaluation of tropical cyclone structure forecasts in a high-resolution version of the multiscale GFDL fvGFS model. Wea. Forecasting, 33, 419–442, https://doi.org/10.1175/WAF-D-17-0140.1.

He, H., J. Yang, and D. Gong, 2015: Decadal changes in tropical cyclone activity over the western North Pacific in the late 1990s. Climate Dyn., 45, 3317–3329, https://doi.org/10.1007/s00382-015-2541-1.

Hendricks, E. A., M. S. Peng, B. Fu, and T. Li, 2010: Quantifying environmental control on tropical cyclone intensity change. Mon. Wea. Rev., 138, 3243–3271, https://doi.org/10.1175/2010MWR3185.1.

Hirata, H., and R. Kawamura, 2013: Remote forcing and response of tropical cyclones over the Bay of Bengal to the Asian jet variability in late fall. SOLA, 9, 27–31, https://doi.org/10.2151/sola.2013-007.

Hirota, N., Y. N. Takayabu, M. Kato, and S. Arakane, 2016: Roles of an atmospheric river and a cutoff low in the

extreme precipitation event in Hiroshima on 19 August 2014. Mon. Wea. Rev., 144, 1145–1160, https://doi.org/10.1175/MWR-D-15-0299.1.

Holopainen, E., and J. Kaurola, 1991: Decomposing the atmospheric flow using potential vorticity framework. J. Atmos. Sci., 48, 2614–2625, https://doi.org/10.1175/1520-0469(1991)048<2614:DTAFUP>2.0.CO;2.

Hong, C., Y. Wu, and T. Li, 2016: Influence of climate regime shift on the interdecadal change in tropical cyclone activity over the Pacific basin during the middle to late 1990s. Climate Dyn., 47, 2587–2600, https://doi.org/10.1007/s00382-016-2986-x.

Hoskins, B. J., M. E. McIntyre, and A. W. Robertson, 1985: On the use and significance of isentropic potential vorticity maps. Quart. J. Roy. Meteor. Soc., 111, 877–946, https://doi.org/10.1002/qj.49711147002.

Hsu, H.-H., C.-H. Hung, A.-K. Lo, C.-C. Wu, and C.-W. Hung, 2008a: Influence of tropical cyclones on the estimation of climate variability in the tropical western North Pacific. J. Climate, 21, 2960–2975, https://doi.org/10.1175/2007JCLI1847.1.

——, A.-K. Lo, C.-H. Hung, W.-S. Kau, C.-C. Wu, and Y.-L. Chen, 2008b: Coupling of the intraseasonal oscillation with the tropical cyclone in the western North Pacific during the 2004 typhoon season. Recent progress in atmospheric sciences: Applications to the Asia-Pacific region, Liou KN and Chou M-D Eds., World Scientific, 49–65, https://doi.org/10.1142/9789812818911_0003.

Hsu, P.-C., T. Li, and C.-H. Tsou, 2011: Interactions between boreal summer intraseasonal oscillations and synoptic-scale disturbances over the western North Pacific. Part I: Energetics diagnosis. J. Climate, 24, 927–941, https://doi.org/10.1175/2010JCLI3833.1.

Hu, A., and G. A. Meehl, 2009: Effect of the Atlantic hurricanes on the oceanic meridional overturning circulation and heat transport. Geophys. Res. Lett., 36, L03702, https://doi.org/10.1029/2008GL036680.

Iacono, M. J., and Coauthors, 2008: Radiative forcing by long-lived greenhouse gases: Calculations with the AER radiative transfer models. J. Geophys. Res., 113, D13103, https://doi.org/10.1029/2008JD009944.

Jones, S. C., and Coauthors, 2003: The extratropical transition of tropical cyclones: forecast challenges, current understanding, and future directions. Wea. Forecasting, 18, 1052–1092, https://doi.org/10.1175/1520-0434(2003)018<1052:TETOTC>2.0.CO;2.

Keller, J. H., and Coauthors, 2019: The extratropical transition of tropical cyclones. Part II: Interaction with the midlatitude flow, downstream impacts, and implications for predictability. Mon. Wea. Rev., 147, 1077–1106, https://doi.org/10.1175/MWR-D-17-0329.1.

Kendall, M. G., 1948: Rank correlation methods. Charles Griffin, London.

Kikuchi, K., 2021: The boreal summer intraseasonal oscillation (BSISO): A review. J. Meteor. Soc. Japan, 99, https://doi.org/10.2151/jmsj.2021-045.

Knutson, T. R., and Coauthors, 2019: Tropical cyclones and climate change assessment: Part I. Detection and attribution. Bull. Amer. Meteor. Soc., 100, 1987–2007, https://doi.org/10.1175/BAMS-D-18-0189.1.

——, and ——, 2020: Tropical cyclones and climate change assessment: Part II. Projected response to anthropogenic warming. Bull. Amer. Meteor. Soc., 101, E303–E322, https://doi.org/10.1175/BAMS-D-18-0194.1.

——, ——, and C. Chou, 2012: Propagation and maintenance mechanism of the TC/submonthly wave pattern and TC feedback in the western North Pacific. J. Climate, 25, 8591–8610, https://doi.org/10.1175/JCLI-D-11-00643.1.

Ko, K.-C., and H.-H. Hsu, 2009: ISO modulation on the submonthly wave pattern and recurving tropical cyclones in the tropical western North Pacific, J. Climate, 22, 582–599, https://doi.org/10.1175/2008JCLI2282.1.

Kobayashi, S., and Coauthors, 2015: The JRA-55 reanalysis: General specifications and basic characteristics. J. Meteor. Soc. Japan, 93, 5–48, https://doi.org/10.2151/jmsj.2015-001.

Kosaka, Y., and H. Nakamura, 2006: Structure and dynamics of the summertime Pacific–Japan teleconnection pattern. Quart. J. Roy. Meteor. Soc., 132, 2009–2030, https://doi.org/10.1256/qj.05.204.

——, and ——, 2008: A comparative study on the dynamics of the Pacific–Japan (PJ) teleconnection pattern based on reanalysis datasets. SOLA, 4, 9–12, https://doi.org/10.2151/sola.2008-003.

——, and ——, 2010: Mechanisms of meridional teleconnection observed between a summer monsoon system and a subtropical anticyclone. Part I: The Pacific–Japan pattern, J. Climate, 23, 5085–5108, https://doi.org/10.1175/2010JCLI3413.1.

Kossin, J. P., 2018: A global slowdown of tropical-cyclone translation speed. Nature, 558, 104–107,

https://doi.org/10.1038/s41586-018-0158-3.

——, K. A. Emanuel, and G. A. Vecchi, 2014: The poleward migration of the location of tropical cyclone maximum intensity. Nature, 509, 349–352, https://doi.org/10.1038/nature13278.

——, ——, and S. J. Camargo, 2016: Past and projected changes in western North Pacific tropical cyclone exposure. J. Climate, 29, 5725–5739, https://doi.org/10.1175/JCLI-D-16-0076.1.

Kubota, T., and Coauthors, 2020: Global Satellite Mapping of Precipitation (GSMaP) products in the GPM era. Satellite precipitation measurement, Springer, https://doi.org/10.1007/978-3-030-24568-9_20.

Kurihara, Y., M. A. Bender, R. E. Tuleya, and R. J. Ross, 1995: Improvements in the GFDL hurricane prediction system. Mon. Wea. Rev., 123, 2791–2801, https://doi.org/10.1175/1520-0493(1995)123<2791:IITGHP>2.0.CO;2.

Kwon, H. J., S.-H. Won, M.-H. Ahn, A.-S. Suh, and H.-S. Chung, 2002: GFDL-type typhoon initialization in MM5. Mon. Wea. Rev., 130, 2966–2974, https://doi.org/10.1175/1520-0493(2002)130<2966:GTTIIM>2.0.CO;2.

Kwon, I.-H., and H.-B. Cheong, 2010: Tropical cyclone initialization with a spherical high-order filter and an idealized three-dimensional bogus vortex. Mon. Wea. Rev., 138, 1344–1367, https://doi.org/10.1175/2009MWR2943.1.

Li, K., Q. He, Y. Yang, and W. Yu, 2020. Equatorial moisture dynamics of the quasi-biweekly oscillation in the tropical northwestern Pacific during boreal summer. Geophys. Res. Lett., 47, e2020GL090929, https://doi.org/10.1029/2020GL090929.

Li, T., and B. Fu, 2006: Tropical cyclogenesis associated with Rossby wave energy dispersion of a preexisting typhoon. Part I: satellite data analyses. J. Atmos. Sci., 63, 1377–1389, https://doi.org/10.1175/JAS3692.1.

Lin, S.-J., 1997: A finite-volume integration method for computing pressure gradient force in general vertical coordinates. Quart. J. Roy. Meteor. Soc., 123, 1749–1762, https://doi.org/10.1002/qj.49712354214.

——, 2004: A “vertically Lagrangian” finite-volume dynamical core for global models. Mon. Wea. Rev., 132, 2293–2307, https://doi.org/10.1175/1520-0493(2004)132<2293:AVLFDC>2.0.CO;2.

——, and R. B. Rood, 1997: An explicit flux-form semi-Lagrangian shallow-water model on the sphere. Quart. J.

Roy. Meteor. Soc., 123, 2477–2498, https://doi.org/10.1002/qj.49712354416.

Lin, Y.-L., R. D. Farley, and H. D. Orville, 1983: Bulk parameterization of the snow field in a cloud model. J. Climate Appl. Meteor., 22, 1065–1092, https://doi.org/10.1175/1520-0450(1983)022<1065:BPOTSF>2.0.CO;2.

Liu, K. S., and J. C. L. Chan, 2013: Inactive period of western North Pacific tropical cyclone activity in 1998–2011. J. Climate, 26, 2614–2630, https://doi.org/10.1175/JCLI-D-12-00053.1.

Matsuura, T., M. Yumoto, and S. Iizuka, 2003: A mechanism of interdecadal variability of tropical cyclone activity over the western North Pacific. Climate Dyn., 21, 105–117, https://doi.org/10.1007/s00382-003-0327-3.

Menkes, C. E., and Coauthors, 2012: Comparison of tropical cyclogenesis indices on seasonal to interannual timescales. Climate Dyn., 38, 301–321, https://doi.org/10.1007/s00382-011-1126-x.

Murakami, H., 2014: Tropical cyclones in reanalysis data sets. Geophys. Res. Lett., 41, 2133–2141, https://doi.org/10.1002/2014GL059519.

——, T. Li, and M. Peng, 2013: Changes to environmental parameters that control tropical cyclone genesis under global warming. Geophys. Res. Lett., 40, 2265–2270, https://doi.org/10.1002/grl.50393.

Nitta, T., 1987: Convective activities in the tropical western Pacific and their impact on the Northern Hemisphere summer circulation. J. Meteor. Soc. Japan, 65, 373–390, https://doi.org/10.2151/jmsj1965.65.3_373.

Ogura, Y., and D. Portis, 1982: Structure of the cold front observed in SESAME-AVE III and its comparison with the Hoskins–Bretherton frontogenesis model. J. Atmos. Sci., 39, 2773–2792, https://doi.org/10.1175/1520-0469(1982)039<2773:SOTCFO>2.0.CO;2.

Quinting, J. F., and S. C. Jones, 2016: On the impact of tropical cyclones on Rossby wave packets: A climatological perspective. Mon., Wea., Rev., 144, 2021–2048, https://doi.org/10.1175/MWR-D-14-00298.1.

Riboldi, J., M. Röthlisberger, and C. M. Grams, 2018: Rossby wave initiation by recurving tropical cyclones in the western North Pacific. Mon., Wea., Rev., 146, 1283–1301, https://doi.org/10.1175/MWR-D-17-0219.1.

Riemer, M., S. C. Jones, and C. A. Davis, 2008: The impact of extratropical transition on the downstream flow: An idealized modelling study with a straight jet. Quart. J. Roy. Meteor. Soc., 134, 69–91,

https://doi.org/10.1002/qj.189.

——, and ——, 2010: The downstream impact of tropical cyclones on a developing baroclinic wave in idealized scenarios of extratropical transition. Quart. J. Roy. Meteor. Soc., 136, 617–637, https://doi.org/10.1002/qj.605.

Ritchie, E. A., and G. J. Holland, 1999: Large-scale patterns associated with tropical cyclogenesis in the western Pacific. Mon. Wea. Rev., 127, 2027–2043, https://doi.org/10.1175/1520-0493(1999)127<2027:LSPAWT>2.0.CO;2.

——, and W. M. Frank, 2007: Interactions between simulated tropical cyclones and an environment with a variable Coriolis parameter. Mon. Wea. Rev., 135, 1889–1905, https://doi.org/10.1175/MWR3359.1.

Robinson, W. A., 1988: Analysis of LIMS data by potential vorticity inversion. J. Atmos. Sci., 45, 2319–2342, https://doi.org/10.1175/1520-0469(1988)045<2319:AOLDBP>2.0.CO;2.

Rodionov, S. N., 2004: A sequential algorithm for testing climate regime shifts. Geophys. Res. Lett., 31, L09204, https://doi.org/10.1029/2004GL019448.

Rogers, R. F., S. S. Chen, J. Tenerelli, and H. E. Willoughby, 2003: A numerical study of the impact of vertical shear on the distribution of rainfall in Hurricane Bonnie (1998). Mon. Wea. Rev., 131, 1577–1599, https://doi.org/10.1175/2546.1.

Ross, R. J., and Y. Kurihara, 1995: A numerical study on influences of Hurricane Gloria (1985) on the environment. Mon. Wea. Rev., 123, 332–346, https://doi.org/10.1175/1520-0493(1995)123<0332:ANSOIO>2.0.CO;2.

Schumacher, R. S., T. J., Galarneau, Jr., and L. F. Bosart, 2011: Distant effects of a recurving tropical cyclone on rainfall in a midlatitude convective system: A high-impact predecessor rain event. Mon., Wea., Rev., 139, 650–667, https://doi.org/10.1175/MWR-D-11-00307.1.

Seiki, A., Y. Kosaka, and S. Yokoi, 2021: Relationship between the boreal summer intraseasonal oscillation and the Pacific–Japan pattern and its interannual modulations. SOLA, 17, 177–183, https://doi.org/10.2151/sola.2021-031.

Seiler, C., 2019: A climatological assessment of intense extratropical cyclones from the potential vorticity

perspective. J. Climate, 32, 2369–2380, https://doi.org/10.1175/JCLI-D-18-0461.1.

Sekioka, M., 1956: A hypothesis on complex of tropical and extratropical cyclones for typhoon in the middle latitudes. J. Meteor. Soc. Japan, 34, 276–287, https://doi.org/10.2151/jmsj1923.34.5_276.

Shapiro, L. J., 1996: The motion of Hurricane Gloria: A potential vorticity diagnosis. Mon. Wea. Rev., 124, 2497–2508, https://doi.org/10.1175/1520-0493(1996)124<2497:TMOHGA>2.0.CO;2.

Shimada, U., and Coauthors, 2018: Further improvements to the statistical hurricane intensity prediction scheme using tropical cyclone rainfall and structural features. Wea. Forecasting, 33, 1587–1603, https://doi.org/10.1175/WAF-D-18-0021.1.

Sobel, A. H., and S. J. Camargo, 2005: Influence of western North Pacific tropical cyclones on their large-scale environment. J. Atmos. Sci., 62, 3396–3407, https://doi.org/10.1175/JAS3539.1.

Sugi, M., A. Noda, and N. Sato, 2002: Influence of the global warming on tropical cyclone climatology: An experiment with the JMA global model. J. Meteor. Soc. Japan, 80, 249–272, https://doi.org/10.2151/jmsj.80.249.

Takaya, K., and H. Nakamura, 2001: A formulation of a phase-independent wave-activity flux for stationary and migratory quasigeostrophic eddies on a zonally varying basic flow. J. Atmos. Sci., 58, 608–627, https://doi.org/10.1175/1520-0469(2001)058<0608:AFOAPI>2.0.CO;2.

Takemura, K., and H. Mukougawa, 2021: A new perspective of Pacific–Japan pattern: Estimated percentage of the cases triggered by Rossby wave breaking. J. Meteor. Soc. Japan, https://doi.org/10.2151/jmsj.2022-006.

Thorpe, A. J., 1985: Diagnosis of balanced vortex structure using potential vorticity. J. Atmos. Sci., 42, 397–406, https://doi.org/10.1175/1520-0469(1985)042<0397:DOBVSU>2.0.CO;2.

——, and C. H. Bishop, 1995: Potential vorticity and the electrostatics analogy: Ertel–Rossby formulation. Quart. J. Roy. Meteor. Soc., 121, 1477–1495, https://doi.org/10.1002/qj.49712152612.

Tu, C.-C., Y.-L. Chen, P.-L. Lin, and Y. Du, 2019: Characteristics of the marine boundary layer jet over the South China Sea during the early summer rainy season of Taiwan. Mon. Wea. Rev., 147, 457–475, https://doi.org/10.1175/MWR-D-18-0230.1.

Wang, C., and L. Wu, 2018: Future changes of the monsoon trough: Sensitivity to sea surface temperature gradient

and implications for tropical cyclone activity. Earth's Future, 6, 919–936, https://doi.org/10.1029/2018EF000858.

Wang, C.-C., G. T.-J. Chen, and K.-H. Ho, 2016: A diagnostic case study of Mei-Yu frontal retreat and associated low development near Taiwan. Mon. Wea. Rev., 144, 2327–2349, https://doi.org/10.1175/MWR-D-15-0391.1.

Wang, H., Y. Wang, and H. Xu, 2013: Improving simulation of a tropical cyclone using dynamical initialization and large-scale spectral nudging: A case study of Typhoon Megi (2010). Acta Meteor. Sinica, 27, 455–475, https://doi.org/10.1007/s13351-013-0418-y.

Wang, X., and D.-L. Zhang, 2003: Potential vorticity diagnosis of a simulated hurricane. Part I: Formulation and quasi-balanced flow. J. Atmos. Sci., 60, 1593–1607, https://doi.org/10.1175/2999.1.

Wang, Y., Y. Rao, Z.-M. Tan, and D. Schnemann, 2015: A statistical analysis of the effects of vertical wind shear on tropical cyclone intensity change over the western North Pacific. Mon. Wea. Rev., 143, 3434–3453, https://doi.org/10.1175/MWR-D-15-0049.1.

Wernli, H., and M. Sprenger, 2007: Identification and ERA-15 climatology of potential vorticity streamers and cutoffs near the extratropical tropopause. J. Atmos. Sci., 64, 1569–1586, https://doi.org/10.1175/JAS3912.1.

Winterbottom, H. R., and E. P. Chassignet, 2011: A vortex isolation and removal algorithm for numerical weather prediction model tropical cyclone applications. J. Adv. Model. Earth Syst., 3:8pp, https://doi.org/10.1029/2011MS000088.

Wirth, V., M. Riemer, E. K. M. Chang, and O. Martius, 2018: Rossby wave packets on the midlatitude waveguide—A review. Mon. Wea. Rev., 146, 1965–2001, https://doi.org/10.1175/MWR-D-16-0483.1.

Wu, C.-C., and K. A. Emanuel, 1995: Potential vorticity diagnostics of hurricane movement. Part I: A case study of Hurricane Bob (1991). Mon. Wea. Rev., 123, 69–92, https://doi.org/10.1175/1520-0493(1995)123<0069:PVDOHM>2.0.CO;2.

——, T.-H. Yen, Y.-H. Kuo, and W. Wang, 2002: Rainfall simulation associated with Typhoon Herb (1996) near Taiwan. Part I: The topographic effect. Wea. Forecasting, 17, 1001–1015, https://doi.org/10.1175/1520-0434(2003)017,1001:RSAWTH.2.0.CO;2.

——, T.-S. Huang, W.-P. Huang, and K.-H. Chou, 2003: A new look at the binary interaction: Potential vorticity diagnosis of the unusual southward movement of Tropical Storm Bopha (2000) and its interaction with Supertyphoon Saomai (2000). Mon. Wea. Rev., 131, 1289–1300, https://doi.org/10.1175/1520-0493(2003)131<1289:ANLATB>2.0.CO;2.

——, ——, and K.-H. Chou, 2004: Potential vorticity diagnosis of the key factors affecting the motion of Typhoon Sinlaku (2002). Mon. Wea. Rev., 132, 2084–2093, https://doi.org/10.1175/1520-0493(2004)132<2084:PVDOTK>2.0.CO;2.

Yamada, Y., and Coauthors, 2017: Response of tropical cyclone activity and structure to global warming in a high-resolution global nonhydrostatic model. J. Climate, 30, 9703–9724, https://doi.org/10.1175/JCLI-D-17-0068.1.

Yan, X., and Coauthors, 2019: Quasi-biweekly oscillation of the Asian monsoon rainfall in late summer and autumn: different types of structure and propagation. Climate Dyn., 53, 6611–6628, https://doi.org/10.1007/s00382-019-04946-3.

Yeh, H.-C., G. T.-J. Chen, and W. T. Liu, 2002: Kinematic characteristics of a Mei-Yu front detected by the QuikSCAT oceanic winds. Mon. Wea. Rev., 130, 700–711, https://doi.org/10.1175/1520-0493(2002)130<0700:KCOAMY>2.0.CO;2.

Yokoi, S., and Y. N. Takayabu, 2009: Multi-model projection of global warming impact on tropical cyclone genesis frequency over the western North Pacific. J. Meteor. Soc. Japan, 87, 525–538, https://doi.org/10.2151/jmsj.87.525.

——, C. Takahashi, K. Yasunaga, and R. Shirooka, 2012: Multi-model projection of tropical cyclone genesis frequency over the western North Pacific: CMIP5 results. SOLA, 8, 137–140, https://doi.org/10.2151/sola.2012-034.

Yoshida, R., and H. Ishikawa, 2013: Environmental factors contributing to tropical cyclone genesis over the western North Pacific. Mon. Wea. Rev., 141, 451–467, https://doi.org/10.1175/MWR-D-11-00309.1.

——, Y. Kajikawa, and H. Ishikawa, 2014: Impact of boreal summer intraseasonal oscillation on environment of tropical cyclone genesis over the western North Pacific. SOLA, 10, 15–18, https://doi.org/10.2151/sola.2014-004.

Zhao, H., X. Duan, G. B. Raga, and P. J. Klotzbach, 2018: Changes in characteristics of rapidly intensifying western North Pacific tropical cyclones related to climate regime shifts. J. Climate, 31, 8163–8179, https://doi.org/10.1175/JCLI-D-18-0029.1.